TU
WIEN

TECHNISCHE
UNIVERSITÄT
WIEN

DIPLOMARBEIT

Prototype Modules for the CMS High Granularity Calorimeter

zur Erlangung des akademischen Grades

Diplom-Ingenieur/in

im Rahmen des Studiums

Masterstudium Technische Physik

eingereicht von

Patrick SIEBERER, BSc
Matrikelnummer 1328786
Lichtenegg 12,
3261 Steinakirchen am Forst

ausgeführt am Institut für Hochenergiephysik
der Österreichischen Akademie der Wissenschaften

unter der Anleitung von
Privatdoz. Dipl.-Ing. Dr.techn. Christoph SCHWANDA
und
Univ.Lektor Dipl.-Ing. Dr.techn. Thomas BERGAUER

Wien, am 4.9.2019   Unterschrift des Verfassers   Unterschrift des Betreuers

Kurzfassung

Das High Luminosity Upgrade des LHC am CERN fordert neue Sub-Detektoren für das CMS Experiment vor allem in Vorwärtsrichtung. Einer von diesen ist das High Granularity Calorimeter (HGCal), ein Sampling Kalorimeter, welches hexagonale Silizium-Pad Sensoren als aktive Elemente nutzt. Die aktuelle elektromagnetische und hadronische Kalorimeter-Endkappe des CMS Detektors, welche nicht für die hohen Teilchenflussraten des HL-LHC entworfen wurde, wird mit einem leistungsfähigeren System ersetzt wird. Großflächige Silizumsensoren von 8 Zoll Wafern, welche noch nie zuvor in dieser Anwendung verwendet wurden, werden szintillierende Kristalle ersetzen. Die hexagonalen Module überdecken eine Oberfläche von 600 Quadratmetern und müssen einer Teilchenrate von bis zu $10^{16}\,n_{eq}/cm^2$ standhalten.

Diese Arbeit ist in zwei Teile geteilt. Zuerst wurden Prototyp-Module unter realen Bedingungen während eines Strahltests am CERN untersucht. Prospektive Strahltests benötigen intensive Vorbereitungen, welche Funktionstests, Standardisierung und Simulation im Vorhinein benötigen um Design-Probleme zu identifizieren. Meine Beteiligung an diesem Projekt umfasst den Empfangstest von kleineren Demonstrator-Modulen nach deren Zusammenbau im Ausland und Montage eines sampling Kalorimeter aus diesen, welches in einem Strahltest in CERNs Nord-Areal des SPS Beschleunigers benutzt und getestet werden soll. Danach wurden die Daten analysiert, mit Fokus auf die Performance von einzelnen Modulen in Bezug auf Rauschen und Stabilität der Basiswerte.

Größere 8 Zoll Sensoren und Hexaboards wurden für weitere Verwendung im Detektor produziert. Ich habe am Testen dieser Sensoren und den allerersten Auslesen-Boards teilgenommen.

Danach wurden Studien an Silizium Detektoren durchgeführt. Für diese wurde ein modifiziertes Auslese-Board an Sensoren im Reinraum angeschlossen und ein neues Messsystem aufgesetzt. Kommissionierung dieses Systems und Entwicklungen für zukünftige Nutzung als Ladungserfassungseffizienz-Test sind teil dieser Arbeit. Diese Art von Tests benötigen ein Datenaufnahmesystem. Die Weiterentwicklung dieses Systems, vor allem Integration zusätzlicher Hardware für Labortests und Integration schneller online-Tests während der Datennahme, sind ebenfalls Teil dieser Arbeit.

Zu guter Letzt kombiniert die Analyse von Sensoren, welche das neue System benutzt, Interessen von Modul- und Sensorseite. Diese Studien benötigen ebenfalls eine kombinierte Software, welche Beiträge von (zuvor) völlig verschiedenen Laborsystemen benötigt. Nette Resultate dieser Studie zur Performance von Sensor-Rauschen, welche noch nie zuvor für diesen Sensortyp durchgeführt wurden, werden präsentiert.

Abstract

The High Luminosity upgrade of the LHC at CERN demands new sub-detectors for the CMS experiment especially in forward direction. One of them is the High Granularity Calorimeter (HGCal), a Sampling calorimeter which uses hexagonal silicon pad sensors as active detector material. The current electromagnetic and hadronic calorimeter endcap of the CMS detector, which was not designed for the high particle rates of the HL-LHC, will be replaced by a more powerful system. Large-area silicon sensors built from 8-inch wafers, which have never been used in this application before, will replace scintillator crystals. The hexagonal modules will cover a surface over about 600 square meters and have to resist a particle fluence of up to $10^{16}\,n_{eq}/cm^2$.

This thesis is divided into to main parts. Firstly, prototype modules have been studied under real conditions at a beam test at CERN. Prospective test beams require extensive preparations that include functionality tests, standardization and simulation in advance to identify design problems. My involvement in this project covered the reception test of smaller demonstrator modules after assembly abroad and assembly of a sampling calorimeter out of them to be used and tested during a beam test at CERNs North Area of the SPS accelerator. Afterwards, data analysis has been performed, focusing on performance of single modules with respect to noise and pedestal stability.

Larger 8-inch sensors and hexaboards have been produced for further use in the detector. I took part in testing these sensors and the very first 8-inch readout boards.

Secondly, studies on silicon sensors are conducted. Therefore, a modified readout board has been connected to the sensor in a cleanroom and a complete new measurement system has been set up. Commissioning of this setup and development for future use as a charge collection efficiency test are part of this thesis. All these kind of tests need a data acquisition system. Further development of this system, especially integrating different hardware for laboratory tests as well as integrating fast online tests already during data-taking, have been part of this thesis as well.

Last but not least, analysis of sensors, using the new setup combines interests from modules and sensor perspective. These studies also require a combined software, taking input from two (initially) completely different laboratory setups. Some very nice result from this study on noise performance of sensors, which has never been done before with this type of sensor are presented.

Contents

1. Introduction

1.1. Large Hadron Collider, Luminosity and Upgrade

1.1.1. From LHC to HL-LHC

The worlds most powerful particle accelerator, the Large Hadron Collider (LHC) at CERN collides particles at almost the speed of light, where each of them has an energy of 7 TeV. The LHC collides bunches of protons, containing $\sim 1.2 \cdot 10^{11}$ particles each. Those particles are detected and characterized at four main experiments, ATLAS (A Toroidal LHC ApparatuS), ALICE (A Large Ion Collider Experiment), LHCb (Large Hadron Collider beauty) and CMS (Compact Muon Solenoid). After the discovery of the Higgs-boson in 2012, the LHC is being upgraded step by step following a schedule shown in figure 1.1. After a period of roughly three years data taking, a so-called long shutdown (LS) is scheduled for roughly two years to upgrade the LHC and experiments. Currently, in 2019, the LHC is in LS-2 which is focussing on upgrading injectors and preparatory work for the High-Luminosity-LHC (HL-LHC), starting in the year 2025. Figure 1.1 also

Figure 1.1.: Roadmap of the LHC showing the steps towards HL-LHC. LS1, LS2 and LS3 are so-called long shutdowns which are, together with the year-end-technical-stops (YETS), the only possibility to upgrade the machine. An extended YETS (EYETS) was needed after 2016 in order to upgrade cooling, vacuum and other cryogenic facilities. The two biggest detectors, ATLAS and CMS, are upgraded in two phases during LS2 and LS3. Picture taken from [1]

shows the increase of energy and luminosity for the LHC. While energy will stay the same after 2020, luminosity will increase due to the HL-LHC upgrade. This is possible by squeezing bunches of protons together, which results in around 200 colliding protons compared to roughly 25 nowadays, before the HL-LHC. This process is called an increase of the *pile-up*. Luminosity is closely related to cross-section of collisions. The unit *barn* is used for describing cross-sections in high energy physics, where 1 barn = 10^{-28} m^2. If one multiplies the cross-section with the (instantaneous) luminosity of the beam, which is measured in number of particles per time per area, one gets the rate of collisions. Thus, (time-)integrated luminosity is given in inverse barns b^{-1} or, in order to express it in typical orders of magnitude for LHC, inverse femtobarn fb^{-1}.

1.1.2. Prospects for Physics

An increase in luminosity leads to more interactions and thus more data for the detectors. All of the detectors will have to cope with new challenges, as described in section 1.2.3, however, it also opens up new possibilities to study rare processes that might produce particles we could not detect yet. It is known that the standard model is incomplete, since it can not explain all phenomena from cosmic observations, such as dark matter, weakly interacting massive particles (WIMPs) or the matter-antimatter asymmetry. Also the measured mass of the Higgs boson does not fully agree with the predictions of the standard model.

Some extensions of the standard model predict particles at energy levels that are in the range of LHC and could be theoretically measured, but have not been found yet because the production probability for those particles is very low. All of these phenomena and theories are addressed by HL-LHC, which aims to study them in detail.

1.2. Compact Muon Solenoid CMS

1.2.1. Introduction and Composition

CMS is one of four big experiments of the LHC. A brief overview of this detector is given here, more details on specific parts are given throughout the thesis whenever needed.

CMS is one out of two general purpose detectors, originally designed to find the Higgs-boson as last missing particle of the standard module. After the discovery of the Higgs in 2012, CMS aims to precisely measure interactions of different particle with Higgs, as well as discovering new physics beyond the standard model, as described in section 1.1.2. CMS is also called the *Cylindrical Onion* due to its cylindrical structure and the many layers. It consists of a barrel part and two endcaps to assure a 4π coverage. The different sub-detectors of CMS include an inner and outer Tracker in the barrel, as well as an electromagnetic calorimeter (ECAL), a hadronic calorimeter (HCAL) calorimeter and the muon system which are present in barrel and both endcaps. A schematic of all the subsystems can be seen in figure 1.2.

The name of CMS is chosen to emphasize its design. Comparing the volume of about $3.7 \cdot 10^6$ m^3 and its mass of 14000 tons to other detectors, CMS is a very compact detector.

CMS DETECTOR
Total weight : 14,000 tonnes
Overall diameter : 15.0 m
Overall length : 28.7 m
Magnetic field : 3.8 T

STEEL RETURN YOKE
12,500 tonnes

SILICON TRACKERS
Pixel (100x150 µm) ~1m² ~66M channels
Microstrips (80x180 µm) ~200m² ~9.6M channels

SUPERCONDUCTING SOLENOID
Niobium titanium coil carrying ~18,000A

MUON CHAMBERS
Barrel: 250 Drift Tube, 480 Resistive Plate Chambers
Endcaps: 540 Cathode Strip, 576 Resistive Plate Chambers

PRESHOWER
Silicon strips ~16m² ~137,000 channels

FORWARD CALORIMETER
Steel + Quartz fibres ~2,000 Channels

CRYSTAL ELECTROMAGNETIC CALORIMETER (ECAL)
~76,000 scintillating PbWO$_4$ crystals

HADRON CALORIMETER (HCAL)
Brass + Plastic scintillator ~7,000 channels

Figure 1.2.: Different sub-detectors of CMS. The cylindrical layers with horizontal z-axis consist of the 'side' area of the cylinder, called *barrel* and the 'bottom' and 'top' areas, called *endcap*. Picture taken from [2].

Its ability to precisely record muons, as well as the fact that the muon system is the biggest part of CMS, the 'M' is chosen represent this in the name. Due to the compact design, a strong magnet is needed to keep particles as long as possible in the detector system by bending their track. Thus, the solenoid-magnet of CMS is a very strong magnet, holding the world record of the biggest superconductor ever build. Obviously, this has to be represented in the name as well.

1.2.2. Sub-Systems

Tracker

The innermost section of all particle detectors in high energy physics is the so-called tracker. Its main purpose is to record tracks of particles in all three space dimensions. Besides, trackers also reconstruct so-called vertices, which are starting points of secondary interactions.

CMS has an *inner* and *outer tracker*, which are both made of silicon. The CMS-tracker is, with an area of around 200 m² surface, the largest silicon tracker ever built. Since tracks are really dense in the inner part close to the collision point, a high granularity is needed for sensors of the inner tracker. CMS uses silicon-pixel detectors, which have currently 124 million pixels altogether. Highly advanced and complex electronics is needed to acquire data from these sensors with a speed of 40 MHz, which makes this part of the

detector really expensive.

In order to save some costs, the outer tracker consists of silicon strip sensors, which do not have such a high granularity. Such a high granularity is not needed because tracks are not as dense in outer regions as they are in inner parts. The CMS strip detector consists of about ten million strips.

Apart from the challenge of distinguishing many tracks from each other in the inner part, radiation damage is a major concern for trackers. Although silicon is a quite radiation hard material and thus a good choice for tracking, it will suffer from radiation damage due to knows effects that create defects in the lattice. CMS deals with this effect by replacing the tracker every couple of years completely with an upgraded detector.

Calorimeter

The tracker is surrounded by the calorimeter system, which is situated inside the magnet as well. Calorimeters are also present in the endcaps of CMS and not only in the barrel part as for the tracker. The calorimeter system is divided into two subsystems. The ECAL is the inner detector and consists of over 70000 homogenous lead tungstate crystals. More details on this part are given in section 2.3. Its purpose is to measure energy of electromagnetic particles such as photons and electrons. The scintillating crystals produce light when energy is deposited in them, which is detected by photo-diodes at the end of each crystal.

The HCAL surrounds the ECAL and measures energy of hadronic particles, such as pions. It is a sampling calorimeter consisting of alternating layers of absorbers and detectors. Particles loose energy in brass absorbers which are stopping hadrons more efficiently than the ECAL. Their energy is only sampled in the detectors between the brass layers. Silicon photomultipliers on tile are used for measuring energy. However, those brass layers are not enough to stop high energetic particles. Thus, the HCAL is divided into to parts, where just one of them is inside the magnet. Putting the last layers of HCAL outside the magnet provides more space for additional layers and allows to use the magnet itself as an absorbers as well.

Details on energy loss in matter are given in section 2.1, while more considerations about electromagnetic and hadronic calorimeters can be found in section 2.5.

Muon System

The muon system is the outermost part of CMS. It measures tracks of muons and neutrinos. Neutrinos are interacting very weakly, thus they are only measured indirect by missing energy deposit in the calorimeters. The Muon system consists of layers of iron, which serve as absorber and return-yoke for the magnet. These layers the main reason why CMS is such a heavy detector. Drift tubes and cathode strip chambers are used in four detecting layers. The track is reconstructed by fitting a curve through this four sampling points. Since the muon system is quite far away from the interaction point, it does not suffer so much from radiation and is only upgraded nowadays, after ten years of operation, to prepare for future use and not because of non working channels. In fact, the muon system is the most reliable sub-detector of CMS.

Trigger

Counting all readout channels together, CMS has over 130000 channels, most of them in the tracker. Taking into account that those channels acquire data 40 million times per second, it becomes obvious that this amount of data can never be stored or even guided to electronics. In fact, 40 million collsions per second equal to a time frame of only 25 ns, which means that previous particles have not even left the detector when the next ones arrive. Thus, a so-called *trigger* is needed which distinguishes between two events and makes a fast decision if an event is interesting and will be stored or not. CMS uses two trigger systems after each other. The Level-1 trigger reduces amount of data already to around 100 kHz and uses data from the calorimeters and muon system. This part of the trigger has to make a decision within a 25 ns time frame, which is realized with Field Programmable Gate Arrays (FPGA). For the second trigger, the so-called High Level Trigger (HLT), information from all subsystems is used to make a decision if an event is interesting or not. It reconstructs the whole event before making this decision. The HLT reduces amount of data to about 100 events per second.

Comparing the CMS data rate to a high speed camera, which has nowadays around ten million pixels (=readout channels) and records around 2000 times per second, one can imagine how much electronics is used to run the detector and why a good working trigger is essential to run CMS.

1.2.3. Challenges of HL-LHC for CMS

Radiation Damage

The expected radiation environment is studied with the FLUKA[3] program, a package that provides Monte-Carlo simulation for particle transport and interaction with matter. The result for an integrated luminosity of 3000 fb^{-1}, which is the expected rate at the end of HL-LHC is presented in figure 1.3. Considering that radiation dose of one year operation during HL-LHC will equal the integrated dose of the whole operation before HL-LHC from 2009 until 2025, the magnitude of the problem becomes obvious. Most of the detectors and subsystems of the LHC will suffer from this increased radiation and become ineffective. Thus, the high luminosity upgrade replaces some of the sub-detectors with completely new ones that can cope with the high radiation environment.

Pile-Up

Apart from the need to resist a much higher radiation, the increasing pile-up is a huge challenge for the detector as well. The number of tracks and showers will increase by a factor of 5-10, which makes it a lot more difficult to distinguish them from each other which results in the need for a higher granularity for all detectors. This is also needed to choose which interactions are interesting, since it is not possible to record and store information of all tracks and showers. This decision is made by the so-called *trigger*. For HL-LHC, more information from additional sub-detectors should be used for triggering, which increases computing power by a factor of roughly 30. New software techniques,
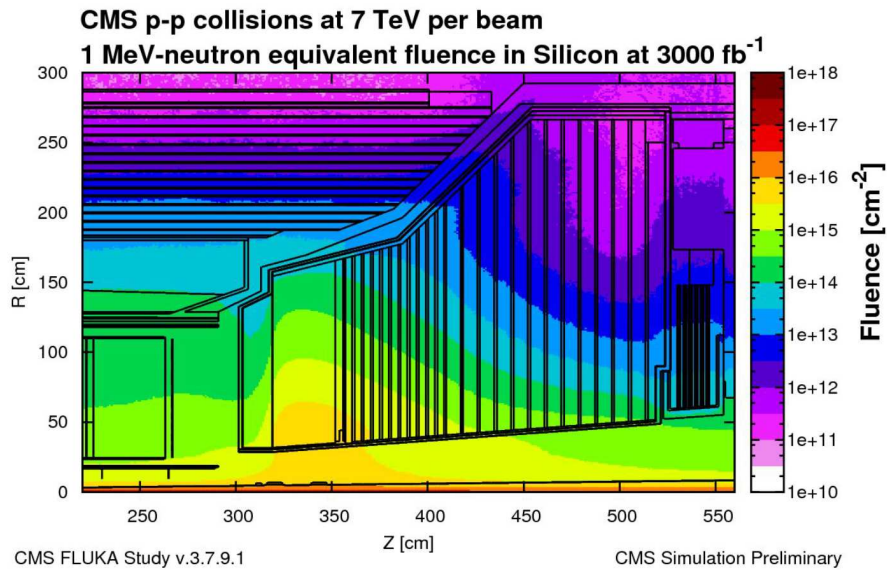
Figure 1.3.: Simulation of radiation environment for an inner part of the CMS detector after HL-LHC. The coordinates are given in cylindrical coordinates, with origin at the collision point of protons. The beam line is on the very bottom. Picture taken from [4, p. 13].

such as machine learning, are needed since it is not feasible to increase the number of computing cores by this factor. As a reference, reconstruction of a event with pile-up of 86 taken in 2016 at the CMS detector can be seen in figure 1.4 to visualize the challenge of increased pile-up.
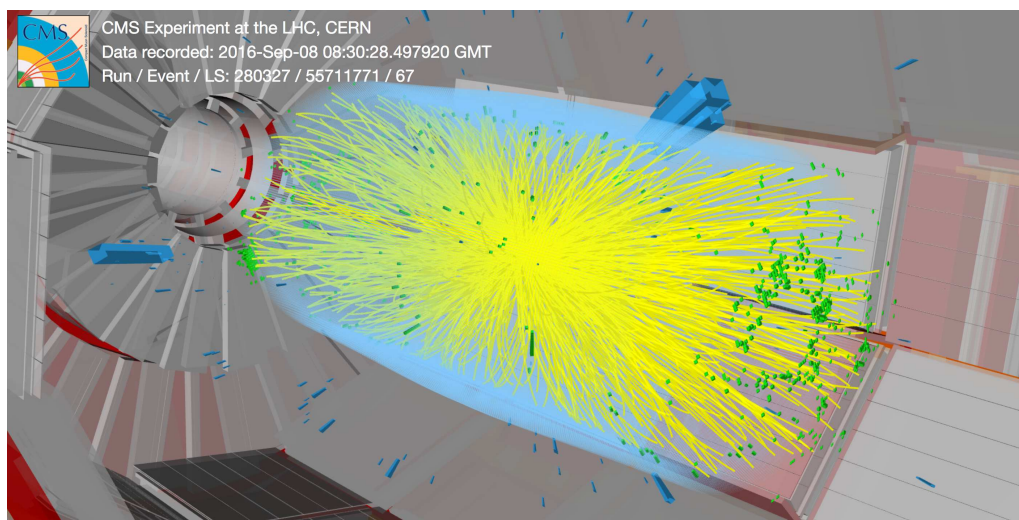
Figure 1.4.: Visualization of a high pile-up event in CMS recorded in 2016. Yellow parts are recorded tracks by the tracker while green parts represent energy deposit in the electromagnetic calorimeter and blue cuboids its structure. Picture taken from [5].

2. Calorimetry

Calorimeters are built to stop particles completely in order to measure their energy. The summed up energy deposit in the detector equals to the energy of the incoming particle. This chapter describes this process very detailed, starting from a more general approach followed by different interaction types of particles with matter. Those are used to describe typical processes inside calorimeters afterwards.

2.1. Particle Interaction with Matter

2.1.1. Bethe Bloch Formula

The Bethe Bloch formula

$$-\frac{\mathrm{d}E}{\mathrm{d}x} = 4\pi N_A r_e^2 m_e c^2 q^2 \frac{Z}{A}\frac{1}{\beta^2}\left[\frac{1}{2}\ln\left(\frac{2m_e c^2 \beta^2 \gamma^2 E_{kin,max}}{E_{ex}^2}\right) - \beta^2 - \frac{\delta(\gamma)}{2}\right] \qquad (2.1)$$

is an empiric function that describes average energy loss of a charged particle in matter. Details can be found for instance in [6, pp. 21–23]. The used variables are:

$$\frac{\mathrm{d}E}{\mathrm{d}x} = \text{Energy loss per length unit}$$

$$N_A = \text{Avogadro's constant}$$

$$r_e = \text{Electron radius}$$

$$m_e = \text{Electron mass}$$

$$q = \text{charge of incoming particle}$$

$$Z = \text{Atomic number}$$

$$A = \text{Atomic mass}$$

$$\beta = \frac{v}{c}$$

$$\gamma = \text{Relativistic } \gamma \text{ factor: } \frac{1}{\sqrt{1-\beta^2}}$$

$$E_{kin,max} = \text{The maximum kinetic energy a free electron can have}$$
$$\text{after a collision (= maximum of transmitted energy)}$$

$$E_{ex} = \text{mean exitation energy}$$

$$\delta = \text{density correction factor}$$

A graphical representation of the formula is given in plot 2.1. The shown spectrum is for a muon in copper, although the curve looks nearly the same for any other charged particle and material except a shifted x-scale.

The given Bethe-Bloch formula only considers scattering on electrons. For a given
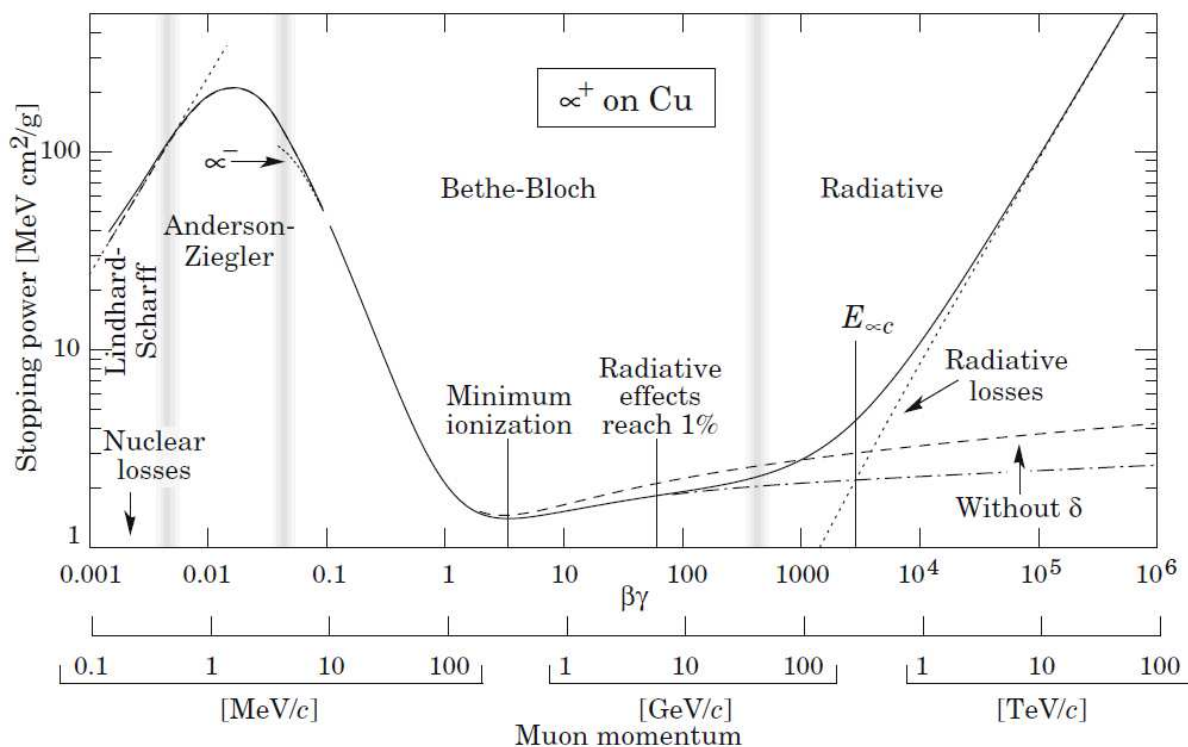
Figure 2.1.: The Bethe Bloch - formula is only valid between 0.1 MeV/c and 800 GeV/c. The relevant part for detectors in high energy physics is the flat valley, containing the Minimum Ionization Point (MIP). Plot taken from [6, p. 22].

target, energy dependence in the Bethe-Bloch formula is only in the β- and γ- factors. Therefore, the $\frac{1}{\beta^2}$-term is dominant for low energies and the $\ln(\gamma^2)$-term is dominant for high energies. The $\frac{1}{\beta^2}$-term comes from the fact that interaction-time Δt is proportional to $\frac{1}{\gamma v}$ and therefore higher for lower energies which result in a higher momentum transfer. This explains the steep rise from the Minimum Ionization Point (MIP) towards lower energies in the energy-loss spectrum.

The $\ln(\gamma^2)$-term is responsible for the slight increase in energy loss above the MIP. This comes from two effects. On the one hand, $E_{kin,max}$ is growing linear with higher energies as a pure kinematic effect. On the other hand, the impact parameter is growing linearly for increasing γ due to relativistic effects. The above mentioned δ-density correction is also a highly-relativistic effects which leads to screening of the electric field from other atoms and thus flattens the $\frac{dE}{dx}$-curve for high energies.

8

At very low energies in the order of the energy of a valence electron, a lot more effects such as quantum mechanical interference and energy loss at the nucleus become important which is not considered in Bethe-Bloch. Neither are radiative losses, such as pair-production and fission, which occur at very high energies.

Consequences of Bethe-Bloch

The two most important features observed in the Bethe-Bloch curve are the MIP on the one hand and the flat valley in the middle of the energy scale on the other hand.
The MIP is the point where the least energy is deposited in the detector. Therefore, a detector needs to resolve at least this amount of energy in order to record the full energy of the incoming particle. Since this is such an important value, it is common to report energies in terms of MIPs for comparing results of different detectors. Generally, a muon can be considered as a MIP-like particle because muons are one of the least interacting charged particles.
Counting the fact that the scale in figure 2.1 is double logarithmic, the valley in the middle of the muon is very flat over a wide range of energy. Based on this fact, the MIP-value is generally treated as an energy, which is constant over a wide interval which makes this value suitable as a reference point for physics analysis of this detector and comparison of results with other detectors. A 'MIP-like' particle deposits the least amount of energy possible and is also called MIP (Minimum Ionising Particle), which might be a bit confusing.
In fact, the detector built during this project is calibrated with respect to MIPs instead of absolute energy, which shows the importance of this value.

Statistical Fluctuations

Bethe-Bloch only considers the average loss of energy per length in the material. In reality, this process is a sum of many small contributions, which underlay statistical fluctuations.
Firstly, the amount of interaction fluctuates which can be described by a Poisson-distribution. With additional information from Bethe-Bloch for the average energy loss ΔE, one can calculate the energy resolution $\frac{\sigma(\Delta E)}{\Delta E}$ due to fluctuation in the amount of interactions. $\frac{\sigma(\Delta E)}{\Delta E}$ is proportional to $\frac{1}{\sqrt{N}}$ according to [7, p. 45], thus energy resolution is depending on $\frac{1}{\sqrt{E}}$.
There are also other statistical fluctuations in the amount of transmitted energy per interaction and Heisenberg's uncertainty principle, however, those are less dominant effects.

2.1.2. Bremsstrahlung and Radiation Length X_0

Bethe-Bloch only describes energy loss by interaction with electrons. However, charged particles can also loose energy due to Bremsstrahlung. Bremsstrahlung is the relativistic analogy to classical Rutherford radiation and considers many relativistic corrections such as screening and Coulomb correction. The so-called radiation length X_0 is defined as $\frac{\mathrm{d}E}{\mathrm{d}x} = -\frac{E}{X_0}$ according to [7, p. 64] and describes the characteristic length for energy loss

due to bremsstrahlung. The radiation length gives the average length after which a traversing particle loses $1/e$ of its energy. A good estimation of X_0 for a target consisting only one single type of particles is equation 2.2 according to [8, p. 21].

$$X_0[g/cm^2] = \frac{716.4 \cdot A[g/mol]}{Z(Z+1)\ln\frac{287}{\sqrt{Z}}} \tag{2.2}$$

The variables used in equation 2.2 are:

$$\rho = \text{density of the target}$$
$$A = \text{Atomic mass of the target}$$
$$Z = \text{Atomic number of the target}$$

X_0 is a property of the (microscopic) material and not of the (macroscopic) object. The main dependency is in the A/Z value, which is not depending on the macroscopic object. Thus, this differential property needs to be divided by a factor proportional to the 'number of nuclei' in the way of traversing particles, which is given by the density of the material, to get the physical length of the track in material. The radiation length of lead, which is a very common absorber, is 0.56 g/cm² as an example.

2.1.3. Interaction of Photons with Matter

whereas the main contribution for electron interactions with nuclei comes from bremsstrahlung, the dominating process for photons interacting electromagnetically with a nucleus at high energies is pair production. Feynman-diagrams for both interactions are shown in figure 2.2. The energy of the photon needs to be twice the energy of a resting electron in order to
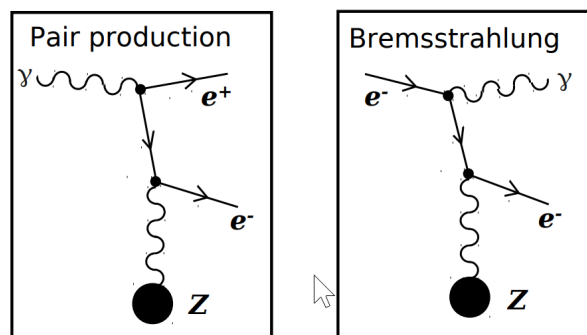
Figure 2.2.: Feynman-diagrams for pair production (incoming photon γ) and bremsstrahlung (incoming electron $e-$). Both diagrams are very similar, the second diagram can be produced just by switching two branches of the first one. Diagrams taken from [9]

produce a electron-positron pair. Moreover, the Coulomb field of the nucleus is needed for an additional photon, as seen in the Feynman diagrams. The photon-absorption length is about $\frac{9}{7}X_0$ considering only pair production, according to [7, p. 86]. Thus, electrons loose energy earlier in the material due to bremsstrahlung than photon due to pair production. For lower energies, Compton scattering (elastic scattering) and photo effect (emission of an electron) are dominating.

10

2.1.4. Interaction of Hadrons with Matter

Strong force plays a major role for hadrons interacting with matter. An exact treatment is very difficult, due to many possible interactions. However, according to the radiation length, a so-called nuclear interaction length λ_I can be defined with same properties. A good approximation for λ_I is given in equation 2.3 according to [8, p. 42].

$$\lambda_I[cm] = \frac{A}{\sigma N_A \rho} \tag{2.3}$$

The variables used in equation 2.3 are:

$$A = \text{Atomic mass of the target}$$
$$\sigma = \text{Cross-section of the hadron interacting with a proton}$$
$$N_A = \text{Avogadro's constant}$$
$$\rho = \text{density of the target}$$

The λ_I is usually given in cm, thus it needs to be multipied with the density of the material to compare it to X_0. λ_I is determined from inelastic nuclear interactions such as excitation of the nucleus or decay into fragments and other secondary particles. Most of these secondary particles are typically pions who are again triggering other interactions. The energy dependence of λ_I is only in the cross-section. For energies > 1 GeV, cross-section is nearly independent from energy and type of the incoming particle. Thus, the nuclear interaction length is constant for a given absorber material. The nuclear interaction length for lead is 194 g/cm^2 which is much higher than its radiation length X_0.

2.2. Showers and Jets

Usually a calorimeter does not record single particles, but collections of particles, so-called showers and jets because single particles are interacting within the detector rather early and start to shower quickly. A short definition of these interaction types is given here.

- *Single Particle*: A single particle passing through the detector.

- *Shower*: A primary particle hitting a target produces a wide range of secondary particles which again interact with other targets and produce even more particles. This is called a particle shower. The maximum lateral spread, so-called shower maximum, as well as the shower starting point are two important parameters for calorimetry.

- *Jet*: In a very highly energetic hadronic decay of bosons, whenever energy is high enough to produce quark - antiquark pairs, a pair of pions can be produced which

are traversing the detector at a small angle with respect to each other. These two pions still have very high energies and the strong interaction increases with distance between them. A quark - antiquark pair is produced which reduces energy of the two pions. This evolution continues, until the energy of the pions are not high enough any more and they start to shower. This way through the detector before these particles start showering, the shower has a thin cone shape and is called jet.

2.2.1. Electromagnetic Showers

Electrons, positrons and photon decay according to section 2.1.2 and 2.1.3 into more photons and pairs due to bremsstrahlung and pair production. These showers are called electromagnetic showers. A widely used approximation for this type of shower is the so-called Rossi-approximation. A visualisation can be found in figure 2.3.

In this simple approximation, an electron decays into two particle with exactly half of
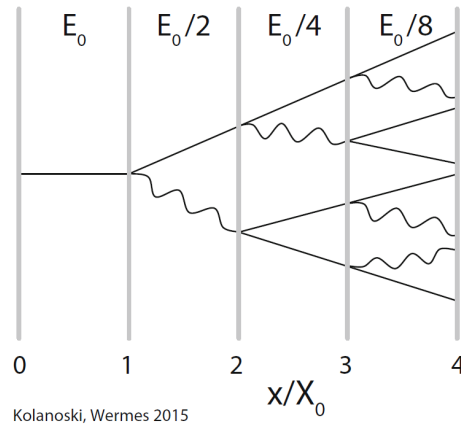
Figure 2.3.: Rossi-approximation for electromagnetic showers with a step-size of one X_0. Electrons are represented with a full line, while photon are represented with a wiggled line. Picture taken from [7, p. 582]

the energy of the incoming electron each after exactly one X_0. This process continues for each particle after every X_0-step and stops at a critical energy E_c. The whole energy deposit E_0 has to be the energy of the incoming particle. Thus, the number of steps N_{tot} equals $\frac{E_0}{E_c}$.

After an amount t of steps (with one X_0 each), $N = 2^t$ particles have been produced with an energy of $E = \frac{E_0}{2^t}$ each. At the maximum amount of steps t_{max}, energy has to equal E_c. Inserting this into the previous formula ($E_c = \frac{E_0}{2^{t_{max}}}$) gives an approximation for maximum length of the shower and maximum amount of particle:

$$t_{max} = \frac{\ln(E_0/E_c)}{\ln(2)} \tag{2.4}$$

$$N_{max} = \frac{E_0}{E_c} \tag{2.5}$$

12

The maximum amount of particles in the shower is linear dependent on energy and can be used as a measure of energy according to equation 2.5. Furthermore, the length of the shower grows only logarithmic with energy, according to 2.4, which makes calorimetry at high energies possible.

Apart from t_{max} as characteristic parameter for the longitudinal shower profile, it is also possible to measure transverse energy distribution of a shower, which is given by the so-called Molière-radius as characteristic parameter. This is the transverse radius of a shower, where 90% of the energy is deposited.

2.2.2. Hadronic Showers

Showers caused by in an incident hadron are much more complicated to described than electromagnetic showers. Different types of hadrons interacting with matter include simple ionization as well as spallation inside a heavy nucleus and creation of secondary hadronic or electromagnetic showers in a nucleus and outside. All of these types are shown in figure 2.4

Smashing a high energetic hadron into a heavy nucleus can rip off single particles or big-
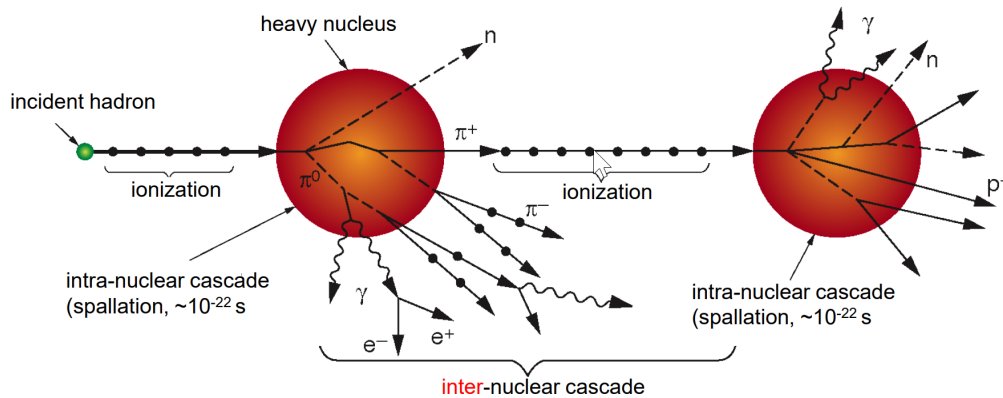
Figure 2.4.: . Picture taken from [10, p. 29]

ger fragments, such as other hadrons or smaller nuclei from it or even split it completely. These fragments can again rip off new hadrons inside the big nuclei, which is a so-called intra-nuclear cascade. The decay of hadrons and smaller emitted nuclei outside of the big nuclei is called inter-nuclear cascade. Such particles can decay in a electromagnetic shower, thus a hadronic shower always has an electromagnetic components as well.

A parameter to describe the length of a hadronic shower is λ_I, as introduced in section 2.1.4, however, a mathematical description and simulation is much more difficult compared to X_0 since it includes a lot more processes.

2.3. Methods of Construction

Calorimeters consist of two fundamentally different parts. Showers are evolving in the *active* part of the detector, while an electronically measurable signal is created in the

passive part.

Sampling detectors consist of alternating layers of massive, passive absorbers and active layers that sample the signal after certain distances. All electronics is attached to the active medium only. A schematic of such a detector is given in figure 2.5.
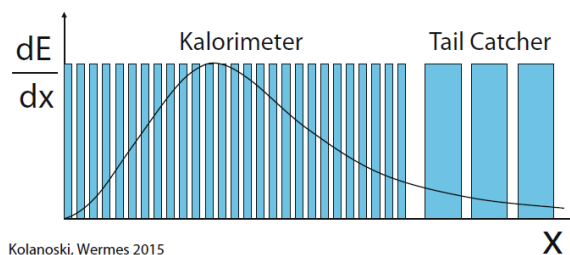
Figure 2.5.: A sampling detector consists of many absorbers (in blue) with active sensors and electronics in-between them. The tail-catcher is a special absorber, that catches the low energetic part at shower-end to record the full energy. Usually, smaller sampling rates (=bigger absorbers) are used for it, since the measured energy does not contribute a lot to the full energy of a shower. Figure taken from [7, p. 601].

Contrary, *homogeneous* detectors, such as crystal scintillators, consist of only one medium where showers are evolving and measured at the same place. An example of such a detector is the inner calorimeter of CMS, which uses lead-tungstate crystals as absorber and active medium. A picture of such crystals is shown in figure 2.6. The crystals
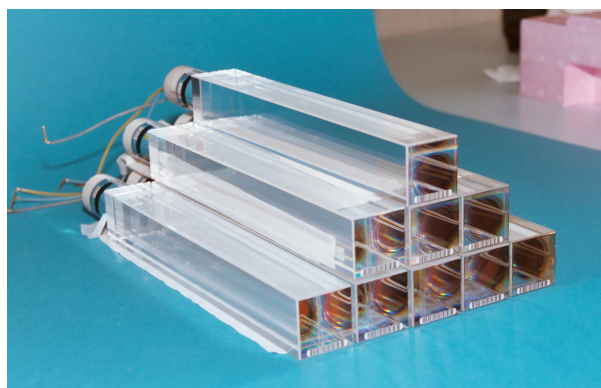
Figure 2.6.: Scintillating crystals for a homogenous sub-detector of CMS. Although crystals are completely transparent, they consist primarily of metal, thus they have the mass of an equivalent metal piece. Picture taken from [11].

are made of a scintillating material which produces light when electrons or photons are passing through. The readout is done via photodetectors at the end of the crystal. Signal amplitude is proportional to the number of produced photons and thus to the energy deposited in it.

2.4. Energy Resolution

Calorimeters are measuring energy, thus the most important quality criteria and parameter of every calorimeter is energy resolution $\frac{\sigma(\Delta E)}{\Delta E}$. Its proportionality to energy of the incoming particle by a factor of $\frac{1}{\sqrt{E}}$ due to statistical fluctuations is already discussed in section 2.1.1. However, there are more contributions to energy resolution which can be summed up according to equation 2.6, which uses the $\oplus$-symbol for quadratic sum.

$$\frac{\sigma_E}{E} = \sqrt{\frac{a^2}{E} + \frac{b^2}{E^2} + c^2} = \frac{a}{\sqrt{E}} \oplus \frac{b}{E} \oplus c \tag{2.6}$$

The first contribution (a-parameter) contains the already discussed statistical fluctuations and is called *stochastic term*. Contributions of the b-parameter comes from electronic noise of the acquisition system, leading to the $\frac{1}{E}$ (indirect) proportionality, while the c-parameter covers all terms that scale linear with energy, such as mechanical irregularities and calibration mistakes. Thus, the c-parameter is called *constant term*. The latter term is dominating for high energies, while the middle term is most relevant at low energies. As a reference, the values of a,b and c for an 100 GeV electron in the homogenous CMS crystals is given in equation 2.7, according to [7, p. 621].

$$\begin{aligned} \frac{a}{\sqrt{E}} &= 0.3\% \\ b &= 120 \text{ MeV} \\ c &= 0.3\% \end{aligned} \tag{2.7}$$

2.5. Electromagnetic and Hadronic Calorimeters

A typical calorimeter consists of two separated parts to measure two different kind of particles. The electromagnetic calorimeter (ECAL) is designed to measure particles which mainly interact electromagnetically, such as photons and electrons. The hadronic calorimeter (HCAL) is designed to measure hadrons, such as pions and protons. Electromagnetic and hadronic showers are fundamentally different, as shown in sections 2.2.1 and 2.2.2, leading to different behaviour in energy resolution for certain construction types of calorimeters.

So-called *sampling-fluctuation* is a problem only in sampling calorimeters. This fluctuation describes differences in measured energy, due to showers evolving randomly and parts of them can also evolve in active layers, where they cannot be measured directly. This effects the a-parameter in equation 2.6 and can lead to two different measured energies for two showers which have the same energy.

This problem does not exist in homogeneous detectors, thus one might think that homogenous detectors are always the better choice. However, it is not possible to grow infinitely long crystals, so a fully homogeneous detector is not always reasonable.

Electromagnetic showers are very short compared to hadronic showers, thus, homogenous and sampling calorimeters exist. Due to long and high energetic showers, which demand

lots of absorber material, hadronic calorimeters are mostly sampling calorimeters only. Figure 2.7 shows the two different kind of showers, where difference in shower-length become obvious.

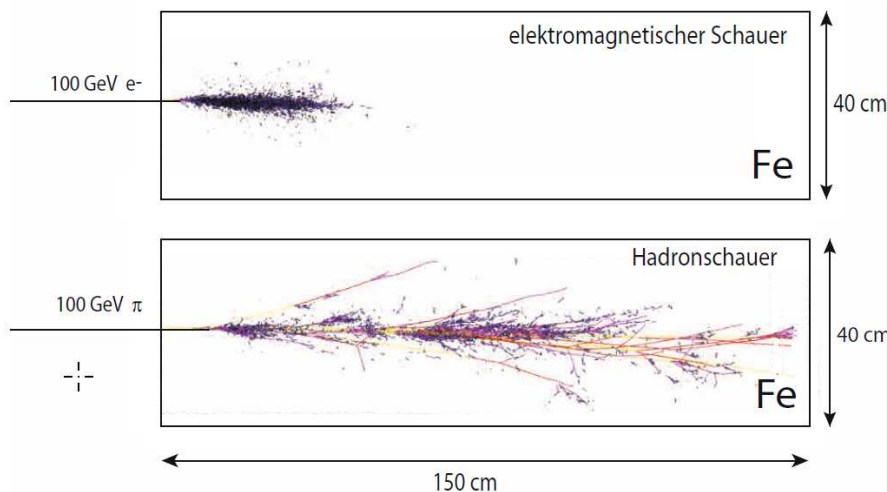Crystals and other scintillators used as homogeneous detectors have another disad-

Figure 2.7.: Different types of showers for incoming particles with same energy. Straight lines correspond to (secondary) hadrons while small dots are electromagnetic particles. Picture taken from [7, p. 593].

vantage: Growing them with a very small diameter is expensive and readout is rather complicated. Thus, lateral resolution of such detectors is usually much worse than those from sampling calorimeters, where different kind of detectors can be used.

2.5.1. Particle Flow

The so-called *particle flow* method was initially introduced in pre-studies for the International Linear Collider (ILC) and is used to achieve better energy resolution by combining data from ECAL and HCAL. Typically 75 % of particles produced at colliders are charged or neutral hadrons, which are measure by ECAL and HCAL according to [12]. The energy resolution of such a shower is than usually driven by the resolution of the HCAL since this sub-detector typically has a worse resolution than the ECAL.

The main idea behind the particle flow technique is to separate all showers from different particles from each other, reconstruct tracks of the particles and combine both information for each secondary particle separately instead of just summing up the measured energy. This requires a high longitudinal and transverse granularity in order to reconstruct tracks directly in the calorimeter. The only parameter that differs significantly for ECAL and HCAL is the b-parameter in formula 2.6. If one assumes a resolution of $\frac{0.15}{\sqrt{E}(\text{GeV})}$ for photons, which are measured in the better performing ECAL and $\frac{0.55}{\sqrt{E}(\text{GeV})}$ for hadrons measured in HCAL, one would theoretical get a resolution in between those two values at around $\frac{0.19}{\sqrt{E}(\text{GeV})}$, taking into account the average production rates of both particle types according to [12]. This calculation assumes that all particles can be fully

distinguished from each other and their energy is measured separately, which is not the case in general. Thus, energy resolution will be a bit worse than this, but still a lot better as if one would use traditional techniques which would result in the energy resolution of the HCAL only.

Particle flow algorithms are recognizing patterns and associate them with reconstructed particles. Those highly complex algorithms demand a lot of studies and differ for each specific detector. The final energy resolution of the detector is a combination of the intrinsic detector-performance and the performance of the particle flow analysis software.

3. Silicon Sensors

The 14th element in the periodic table, silicon, is widely used commercially in computers, telecommunication system and other electronic systems. The commercial availability makes silicon more and more popular for the use in particle physics because its properties are well understood and can be exploited for use in particle detectors. Furthermore, silicon is rather cheap compared to other standard particle detectors like scintillating crystals, which makes it a perfect candidate for large scale detectors.

3.1. Band-Model and Fermi Energy

Silicon is a semiconductor with an indirect band gap of about 1.1 eV which separates the valence band in the conduction band in the so-called band structure model. Due to charge equilibrium, the number of positives holes (p+) in the valence band equals the number of electrons (e-) in the conduction band. Impurities, as well as artificial doping creates additional states in the band gap, allowing to excite more electrons and thus creating a more conductor-like behaviour due to a reduce energy gap. Silicon has four valence electrons and can be either doped with an element that has five valence electrons creating so called *n-type silicon* or with a material containing three valence electrons (*p-type silicon*). An important concept of the band model and the Fermi-Dirac statistics for electrons is the so-called Fermi Energy E_F which represents the highest possible energy of a fermion at T=0 K [6, p. 4]. This equals the energy where $\frac{1}{2}$ of the available energy levels are occupied. Thus, E_F has to be exactly in the middle of the two bands for pure silicon or shifted towards intermediate levels by doping as seen in the upper part of figure 3.1. The most important rule of the Fermi-Dirac mechanism is that E_F is constant for all materials in thermal equilibrium. This is particularly important to understand the following section.

3.2. The pn-Junction

By joining together a n-type and p-type silicon, a so-called pn-junction is created which is the fundamental structure of a silicon sensor. Additional electrons of the n-type will recombine with the additional holes of the p-type silicon close to the interface, creating a so-called space charge region (SCR) where no free charge carriers are available any more since all electron-hole pairs are recombined in this region. A graphical illustration of this process called *depletion* of the sensor is given in figure 3.1. Regarding the band model, electrons of the conduction band of the n-type silicon move to the acceptor levels of the p-type and recombine. Holes move from the valence band of p-type silicon to the donor-level of n-type silicon and recombine as well. These electrons and holes are now missing
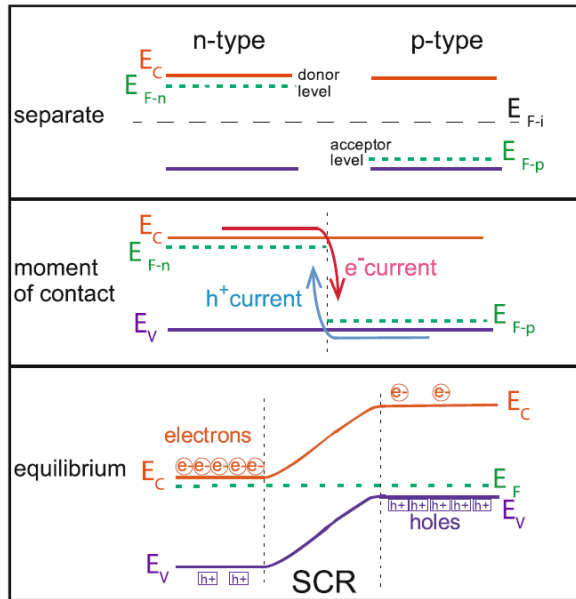
Figure 3.1.: The Fermi Energies of a p-type silicon and a n-type silicon will adjust to each other when bringing them to contact. E_{F-p} and E_{F-n} are the Fermi energies of the separated, doped materials while the dashed E_{F-i} line shows the Fermi level of an un-doped (intrinsic) silicon semiconductor. Both Fermi-levels have to be the same in equilibrium state, which leads to an electric field around the junction. Figure taken from [6, p. 9].

in the silicon layers close to the interface, creating a positively and a negatively charged area and, since electron-hole pairs are electrically neutral, an *electric field* in-between the two silicon types. This electric field in the SCR has opposite direction of the electron diffusion. Equilibrium is reached, when the electron drift from the electric field is high enough to stop additional electrons from recombining.

3.3. Silicon as a Particle Detector

Charged particles traversing a pn-junction create additional electron-hole pairs in the SCR, of the sensor which are separated by the electric field before recombining. This creates a current in the silicon due to the electric field which is pulling them away from each other. This current is collected on electrodes on both sides of the pn-junction and represents the measured signal, as shown in figure 3.2. Charge which is created outside the SCR will not induce a signal, unless it diffuses into the junction, since this charge recombines with the free charge-carries in the material almost immediately. The naturally created SCR just by combining p- and n-type silicon is not enough in order to work as a particle detector: There are still in the order of 10^5 more free charge carries in the non-depleted areas than created by an external particle according to [6, p. 8], which would lead to a recombination of the created electrons and holes before they reach the
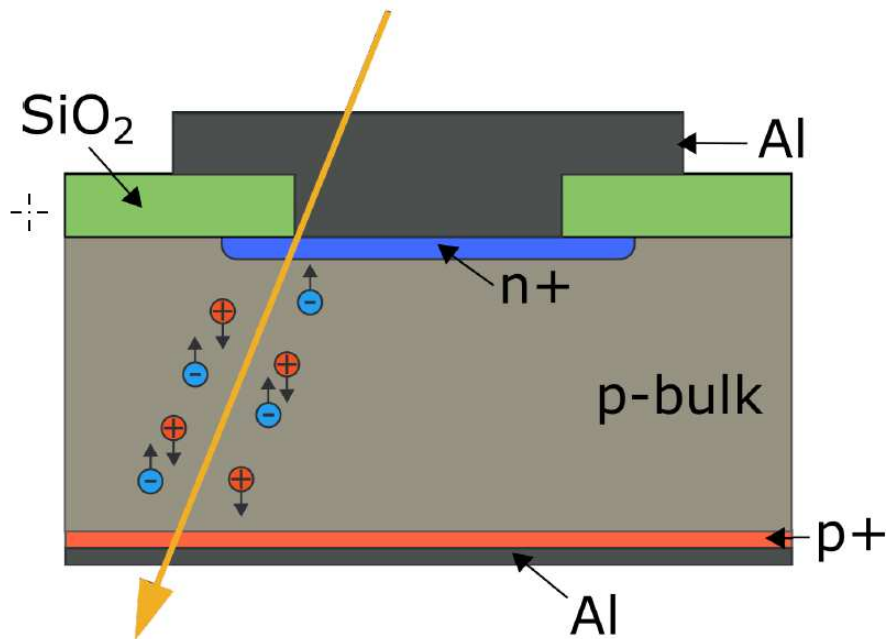
Figure 3.2.: Schematic of a n-on-p silicon sensor. This type of sensor uses p-doped bulk material with an highly doped n implant on top. The backside of the sensor is highly p-doped in order to create an ohmic contact. The n implant and highly doped p-type backside are connected to metal in order to connect wire-bonds to the sensor. Due to oxidation, silicon-oxide is created on non-metal covered pieces, which protects the sensor. The orange arrow shows a traversing particle, creating electron-hole pairs in the SCR. Picture taken from [13, p. 26]

electrodes.

3.3.1. Depletion Voltage

There are two options to reduce the amount of free charge carriers by orders of magnitude which is needed to make a silicon sensor functional as a particle detector.

1. **Cryogenic cooling**
   Cooling to very low temperature decreases the mobility of the charge carriers in the sensor which leads to less recombinations of electrons and holes and therefore a higher signal of the sensor. However, cooling large scale detectors is a big mechanical challenge and therefore not used very often.

2. **Reverse Biasing**
   Connecting the positive side to negative voltage and the n-type side to positive voltage is so-called *reverse biasing*. The voltage source will pull away charge carriers from the silicon, creating an even bigger depletion zone.

In modern particle detectors both methods are used to some extend. However, the second method has a much bigger impact and is thus more exploited for use in detectors. Reverse biasing forces the Fermi-levels of p- and n-type material to move away from each other and thus the final state is not in thermal equilibrium any more (which results in power consumption of the voltage source that is connected to the metallization on the backside and metal implants on the frontside of a sensor as shown in figure 3.2). Voltage applied to the sensor is called depletion voltage. The sensor performance increases for a decreasing amount of free charge carriers in the sensor which equals to an increasing depletion zone. Therefore, silicon sensors are depleted as much as possible in order to achieve the highest possible performance. A fully depleted sensor behaves like a capacitor: It only consists of two electrodes and a dielectric in-between. The full depletion voltage (= minimal voltage that needs to be applied in order to fully deplete the sensor) and the capacity of the sensor at full depletion are two very important characteristics of the sensor.

Due to thermic excitation, some charge carriers are able to dissipate into the SCR, which results in a small current in the sensor even at full depletion voltage. This current is called *leakage current* and is usually determined at a certain reference voltage, which is not necessary the full depletion voltage.

4. HGCal - The CMS Endcap Calorimeter Upgrade

4.1. Current CMS Endcap Calorimeter

4.1.1. Motivation for Endcap Upgrade

Calorimeters of CMS are designed to operate until 500 fb^{-1}, which is clearly below the target for during HL-LHC. Since most of the particles collide at a small angle, most of the energy is deposited in the endcap calorimeters. Thus, barrel calorimeters get much less radiation and do not need to be upgraded. The homogeneous ECAL is made out of scintillating crystals, while the HCAL is a sampling calorimeter consisting of brass absorber layers and plastic scintillators as active detectors.

Light Yield of CMS Crystals

CMS currently uses lead-tungstate crystals in the endcap ECAL as described in section 2.3. The so-called *light-yield* is the ratio of measured (light-)signal over emitted light from crystals and should equal to 1 for an ideal scintillating detector. Unfortunately, this light yield decreases due to radiation damage in the crystal structure when penetrating them with hadrons. Such a study can be seen in figure 4.1 for various luminosities. Considering the fact that HL-LHC will have an integrated luminosity of 3000 fb^{-1} at the end of lifetime, relative light yield will only be a few thousandth for a high η (which equals a small angle between beam and particle). Thus, it is very important to change endcaps completely and use more radiation hard sensors. However, the light yield of barrel detectors is high enough to continue operation even during HL-LHC.

4.2. Phase-2 Upgrade for CMS

Phase-2 upgrade prepares the CMS detector for operation with HL-LHC, while phase-1 upgrade is mainly maintenance and preparatory work for Phase-2. Main goals and challenges for the detector in Phase-2 are described in [14, p. 11] as following:

> The basic goal of the Phase-II upgrade is to maintain the excellent performance of the CMS detector in terms of efficiency, resolution, and background rejection for all the physics objects used in the analysis of the data. The main challenges that must be overcome to achieve this goal are radiation damage to the CMS detector from the high integrated luminosity of the HL-LHC and the very high "pileup" that comes from the high instantaneous luminosity.
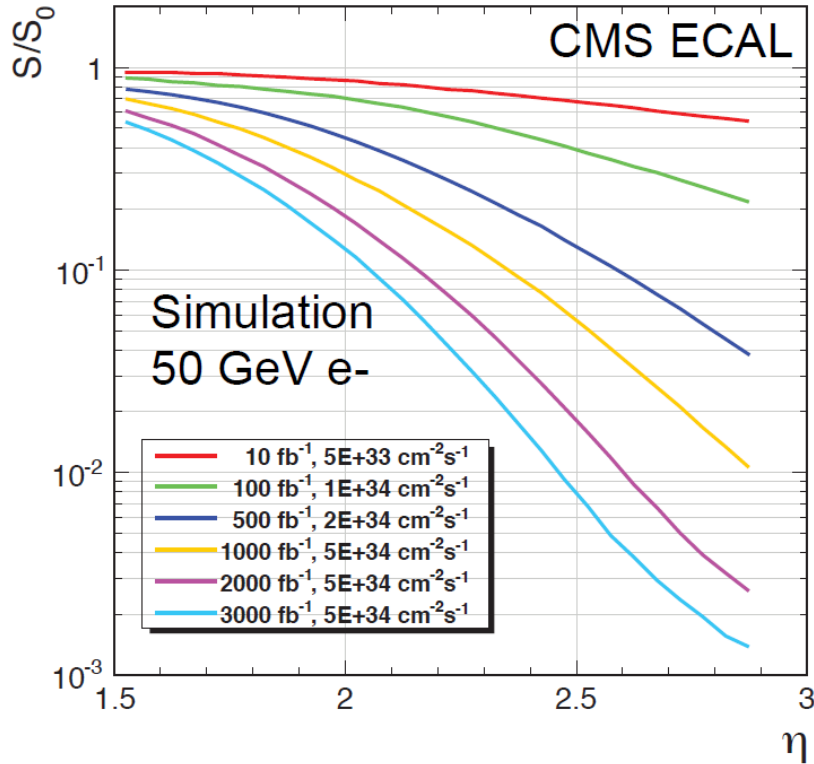
Figure 4.1.: Relative light output S/S_0 for various ageing conditions of CMS ECAL crystals for 50 GeV electrons. Pseudorapidity η is a measure for angles used in high energy physics. A small angle between beam line and particle corresponds to a very high η (up to infinity for parallel case) while an angle of 90 degrees equals 0 η. Picture taken from [14, p. 74].

4.3. Endcap Upgrade

HCAL and ECAL of the CMS endcap calorimeter suffer from decreasing light yield of the crystals and scintillators due to damage in the crystal structure from charged high energetic particles. Moreover, longitudinal and transverse granularity of the current calorimeters is not high enough to deal with the increased pile-up of HL-LHC. A much finer granularity is needed in order to distinguish showers and jets from different particles. Thus, the endcap calorimeters are completely replaced during Phase-2 upgrade by a new detector, the High Granularity Calorimeter (HGCal). HGCal will provide solutions for these problems and can cope with the new requirements of HL-LHC.

4.3.1. Composition of HGCal

HGCal will replace the electromagnetic and hadronic endcap calorimeters on both sides of the detector. A technical drawing of one endcap is shown in figure 4.2. It consists of three sub-detectors using two different techniques for measuring energy. The electromagnetic
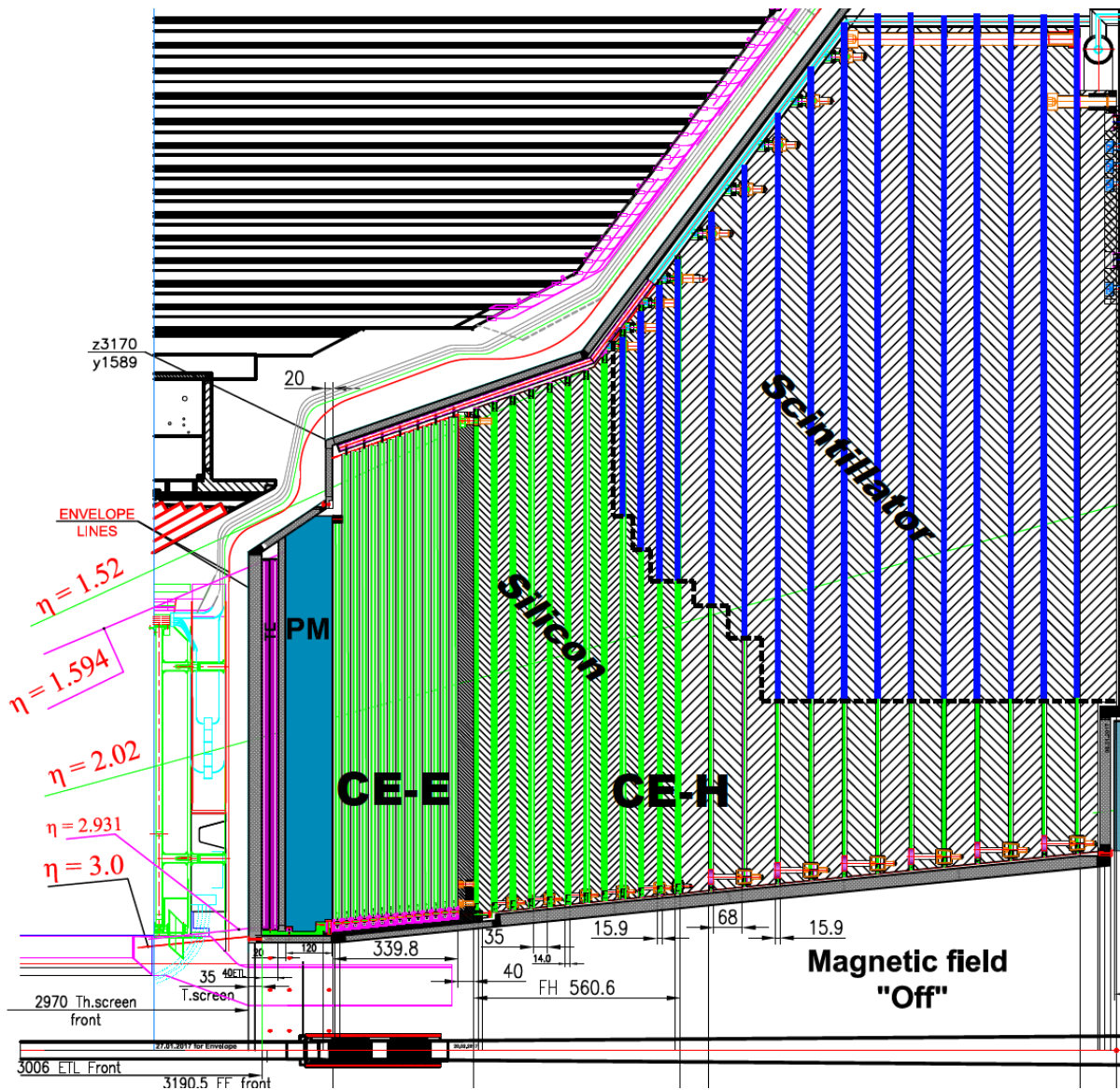
Figure 4.2.: Mechanical structure of HGCal. Due to their better radiation hardness, silicon sensors are used in higher radiated areas (CE-E and CE-H, in green). The backside consists of scintillators (blue). The beam line is shown on the very bottom of the picture. Schematic taken from [4, p. 19].

calorimeter endcap (CE-E) and the hadronic calorimeter endcap (CE-H) are made of metal absorber layers and layers of silicon sensors in between. Absorbers for CE-E are thinner than those for CE-H. Details of this structure can be found in section 6.2. The back part of the detector uses plastic scintillators as active material and silicon photo detectors for readout, which are less radiation-hard compared to silicon detectors. Both materials have been tested for radiation hardness and have proven to resist the expected radiation in their region. The higher granularity compared to the current detectors comes

from the use of silicon pad detectors which have pad size of about 1.1 cm^2 and the use of likewise sampled scintillators. Details are given in section 4.5.

4.4. HGCal as a 5D Calorimeter

The HGCal is a longitudinally sampled calorimeter which consists of an electromagnetic and a hadronic calorimeter. It samples longitudinally in 28 layers with distance of about 2.4 cm between the layers in the electromagnetic part and a varying distance around 3.5 cm in the hadronic part with 22 layers. Transversal sampling is done by the pad structure of silicon sensors. Thus, the sampling area is about 1.1 cm^2 for most of the layers. Due to this longitudinal and transverse sampling, a track of the particle can be reconstructed in all three space dimensions. Furthermore, the HGCal readout chip has a time of arrival measurement which gives additional timing information as well. With the energy being the fifth dimension besides the three spacial dimension and the one time dimension, the HGCal is a so-called 5D-detector. Although its main purpose is the energy measurement, it serves as timing detector and tracker as well. There is no other silicon-based 5D-detector developed so far which makes HGCal a really outstanding detector with a lot of potential for future applications, not only in particle physics.

4.5. Silicon Sensors for HGCal

One slice of silicon sensors consist of many hexagonal sensors that form a big circle-like structure around the beam line. Such a slice is shown in figure 4.3. Thinner sensors are used in the inner part closer to the beam line, which suit better for operation at a high radiation environment.

4.5.1. Layout

Silicon sensors from Hamamatsu Photonics K.K. (HPK) are used. The sensors are so-called silicon pad sensors with 135 cells on a 6-inch wafer. All sensors of the prototype are p-on-n type with a n-doped substrate and a p-doped layer on top. The sensors used in the prototype detector have two different thicknesses. Ninety of the sensors have a depleted thickness of 300 μm and four sensors have a thickness of 200 μm. The sensors themselves as well as the pad cells are hexagonally shaped. The area of one hexagonal cell is around 1.1 cm^2. There are some special, non hexagonally shaped cells per sensor: The so called 'inner calibration cell' with an area of about $1/9^{th}$ of the area of the full hexagonal cell and the surrounding 'outer calibration cell' are located in the middle of the sensor. The former are used for calibration, due to better noise performance compared to bigger cells. This comes from the fact that a smaller area results in a smaller capacitance, which decreases the intrinsic noise of the cell, whilst the MIP signal size stays the same. Half-hexagonal cells and so-called 'mousebite cells' are needed in outer regions of the sensor to fill edges and corners. A picture showing all the different cell types is given in figure 4.4.
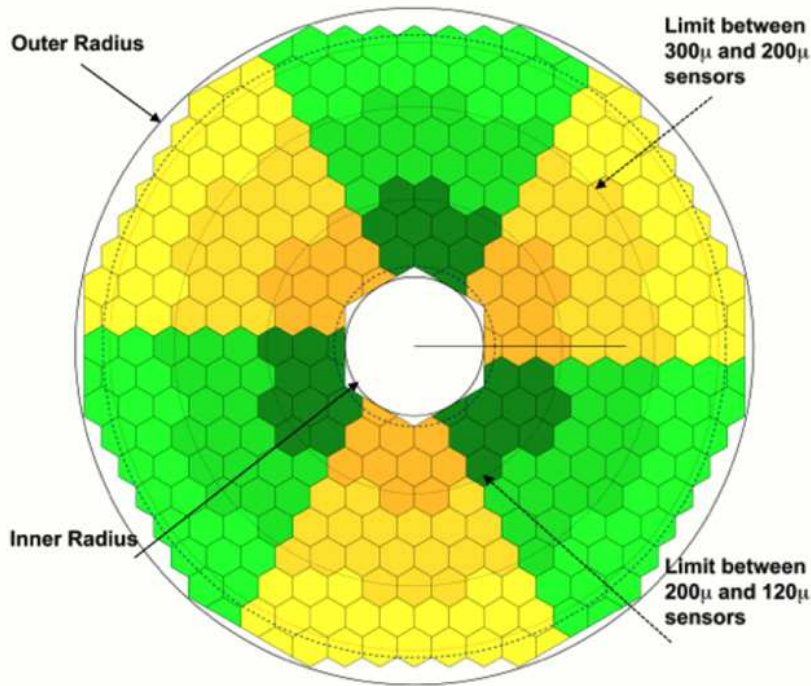
Figure 4.3.: Front view of one slice of the silicon part of the HGCal detector. It corresponds to one green slice in figure 4.2.

Sensors used in HGCal can be represented by a parallel array of capacitors only, thus there is no additional structure for biasing the sensor. This implies that the whole dark current, as described in section 3.3.1 has to flow through the readout electronics and is measured as well. This quite uncommon layout needs special treatment in the analysis software.

4.5.2. Characterization

Sample test of sensors are made before they are mounted onto modules. These tests happen in a cleanroom and include a capacitance measurement up to 1000V and a leakage current measurement using an IV-curve. The latter test is repeated for full modules afterwards and described in section 5.6.3. A two-card measurement system is used for cleanroom measurements which can be found in [15]. An example of the capacitance measurements can be found in Figure 4.6. Clearly visible are four different regions. Those are regions with a different inter-cell distance of 20, 40, 60 and 80 μm. This distance between two cells creates another capacitance, the so-called *inter-cell capacitance*, which contributes to the overall capacitance of the pad. Goal of these different geometries is to measure the noise behaviour and leakage current for different distances. Capacitance and leakage current are very important for the final sensor design, which will have just one uniform distance.
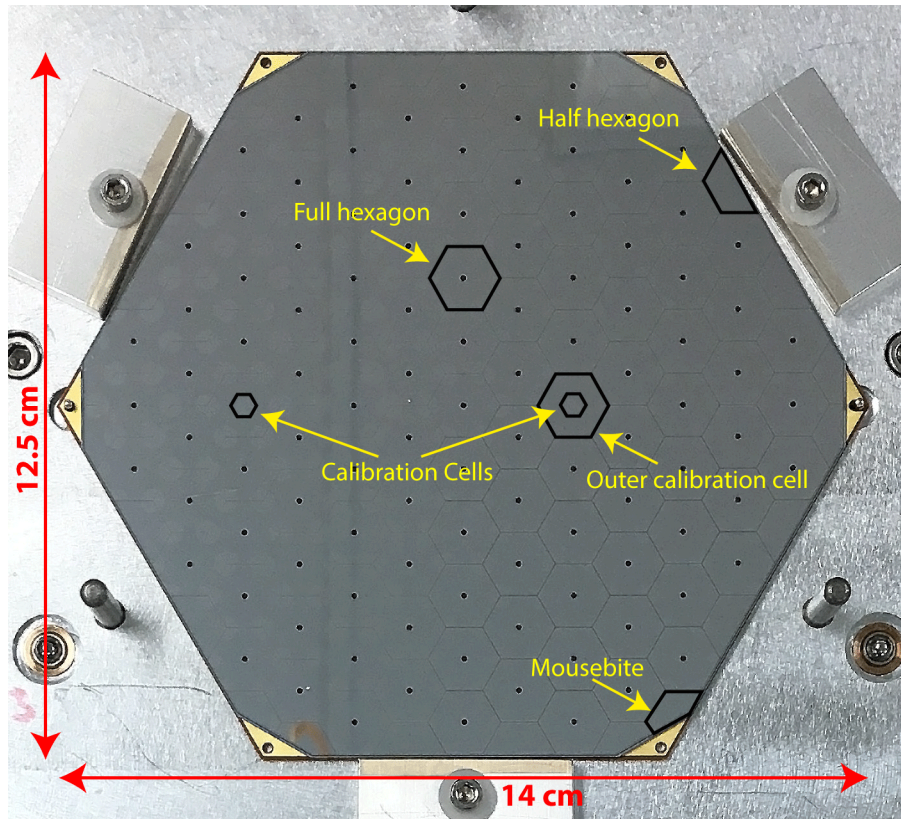
Figure 4.4.: Picture of a 6-inch sensor. The inner and outer calibration cells are visible in the middle of the sensor, whereas the half cells and the mousebite cells are located in the edges and corners.
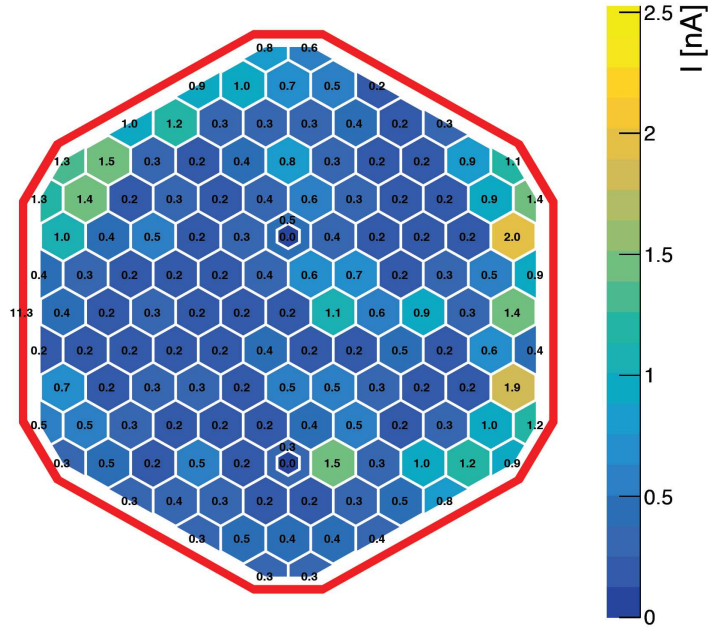
Figure 4.5.: Pad-leakage current per cell at 1000 V for an example 6-inch, 300 μm thick sensor. The red line surrounding the sensor is the so-called *guard-ring*, a special implantation in the silicon used for shielding the electric field.
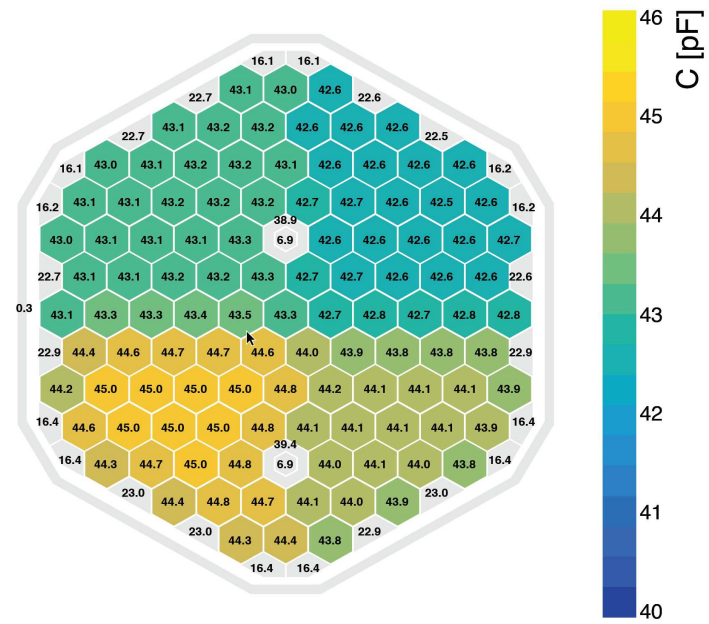
Figure 4.6.: Capacitance above full depletion (400 V) measured with 1 kHz for the same example sensor (6-inch, 300 μm active thickness, 135-cell p-on-n sensor). The four quadrants in the capacitance measurements correspond to four different cell geometries with different inter-cell distance on the sensor.

5. HGCal Modules

5.1. Construction of HGCal Prototype Modules

In order to test the silicon sensors for use in HGCal, prototype modules have been designed. A module is a stack of layers as shown in figure 5.1. A hexagonal PCB, the so-called *hexaboard* consists of all frontend electronics and is described in section 5.2. Every silicon-pad is wire-bonded to the hexaboard through holes in the corner of three cell, which connects a readout channel of the readout chip with a silicon pad.
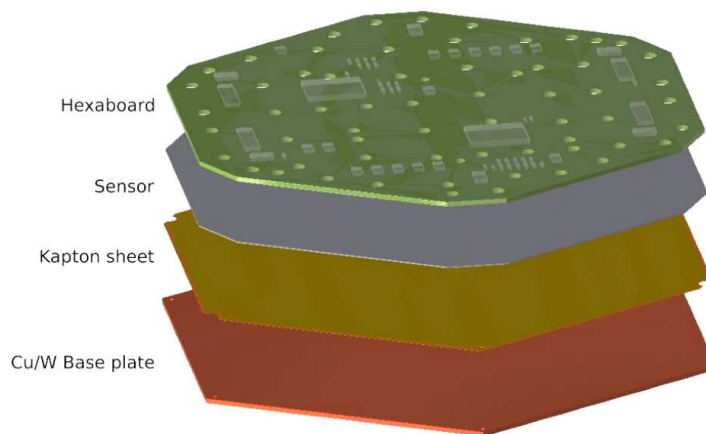

Figure 5.1.: Layers of a prototype 6-inch module. Not shown is a very thin metallic layer between the kapton sheet and the sensor which is used to apply positive high voltage to the backside of the sensor for (reverse) biasing. Figure taken from [4, p. 28].

The backside of the module is the so-called baseplate which is used for cooling, grounding and mechanical assembly in the detector. The baseplate is electrically isolated from the silicon through a kapton layer and also serves as an absorber for the particles. Different baseplates have been tested during a beam test; details can be found in section 6.2.

5.2. Hexaboard

All of the measurements for this project use the (sometimes modified) hexaboard as central readout PCB. Readout-chips, power lines for biasing and electronics, as well as

data-lines are placed on this PCB.
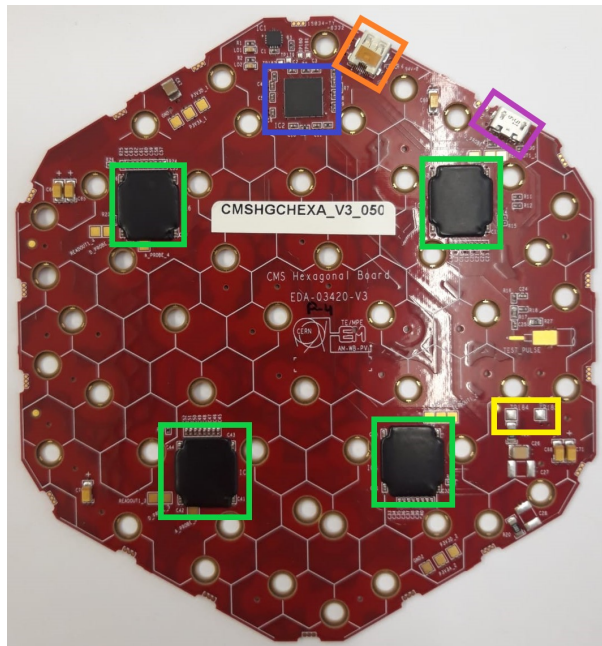
Component	Usage
SKIROC2-CMS	readout chip
micro-HDMI	data transfer, LV power supply
micro-USB	flash FPGA
MAX10-FPGA	send and receive commands and data
HV bonding pads	bias sensor with HV

Figure 5.2.: Picture of a pure hexaboard. The most important electronic parts are given in the table on the right.

Figure 5.2 shows the main components of a hexaboard. Each hexaboard has four readout chips, called SKIROC2-CMS which are protected with glob top, a special non-conductive epoxy resin, to protect the wire bonds. This main frontend readout chip has a lot of electronic circuits which are described in detail in section 5.2.1. These four chips send acquired digital data to an MAX10 Field Programmable Gate Array (FPGA), which is collecting and merging bits together and sends them through an HDMI cable (connected with a micro-HDMI-plug) to another FPGA from the data acquisition system (DAQ). Also the slow control commands which configure the readout chips are sent through this HDMI cable and are distributed by the FPGA. Moreover, also the low voltage power supply that powers all the readout electronics is connected through this cable. The hexaboard does not only consist of electronics for DAQ and slow control commands, it also has bonding pads for the high voltage that is needed to apply a reverse bias voltage to the sensor and another micro-USB connector as part of the Joint Test Action Group (JTAG)-chain, which is needed to flash the FPGA.

5.2.1. SKIROC-CMS

The hexaboard uses the so-called SKIROC2-CMS as the central Application-Specific Integrated Circuit (ASIC) for data acquisition. The chip is developed by OMEGA (Organisation de Micro-Electronique Générale Anancée) as a successor of their SKIROC2-chip.

This ASIC is used for the digital readout in all experimental setups during this project. The four measurement circuits of the SKIROC2-CMS are described in detail in this chapter. A lot of definitions are introduced in this section and will be used further on in the thesis.

Overview of the Functionalities

An overall block diagram is shown in figure A.1 in the appendix. Each channel has its own readout system in the chip, which means all of the described features are duplicated 64 times per chip because each SKIROC2-CMS has 64 channels. However, just half of them (the even channels) are also connected to cells in the silicon in order to reduce power consumption and warm up of the chips. Each channel has two inputs: The regular analogue input in_{PA} which is connected to a silicon pad and a test input, which is connected to the injection circuit of the readout electronics. The analogue part of the chip begins with a pre-amplifier PAC which is common for all four measurement circuits. The signal can be inverted after the pre-amplifier in order to measure positive and negative pulses which is needed for n-type and p-type sensors. Afterwards, the signal goes to the *HighGain (HG)*, *LowGain (LG)*, *Time over Threshold (ToT)* and *Time of Arrival(ToA)* measurement simultaneously. After these four measurements, the still analogue signals are multiplexed into a single output line again and digitized by a twelve bit Analogue to Digital Converter (ADC). The digital part uses a 40 MHz clock which has to be provided externally.

HighGain and LowGain

Two basic measurements which are used to measure energy directly are HighGain and LowGain. The signal is amplified by a factor of ten in the HG and a factor of one in the LG. Afterwards, there is a 13 cell-deep Switch Capacitor Array (SCA) which covers a total time frame of 325 ns, thus the signal is switched to the next capacitor after 25 ns, thus the HG and LG have a sampling rate of 40 MHz. This capacitor array is circular and running continuously. Whenever a *stop-acquisition* signal is arriving, these 13 capacitors stop acquiring data. An additional value, the so-called RollMask (RM) gives the position of the first time-sample (TS).

Time over Threshold

ToT measurement is for very large signals where the HG and LG already saturate. This comparator compares the signal with a given threshold voltage, which is choosable by a 10-bit Digital to Analogue Converter (DAC). When the signal is above threshold, a ramp is started and stops as soon as the signal is below the threshold again. The output is the analogue value of the ramp. A fast and a slow ramp are available for the ToT.

Time of Arrival

ToA measurement is a *timing* measurement which gives additional information about timing of the particle. The signal is shaped in a fast (around 5 ns) shaper and than compared to an analogue threshold which can be again chosen by a 10-bit DAC. When threshold is reached, the ramp is started which stops running at the upper-next rising edge of the overall 40 MHz clock which is a needed additional input. The output is again the analogue signal from the ramp which is proportional to the time. As a second measurement, the same procedure is done just with stopping the ramp after the upper-next falling edge of the 40 MHz clock instead of the rising edge.
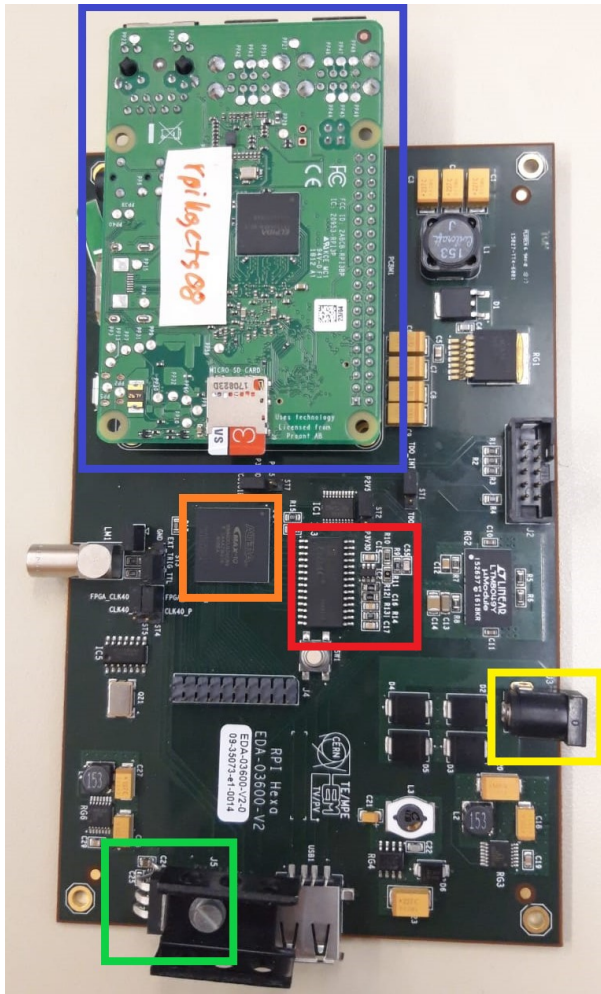
5.3. Teststand

The so-called *teststand* is a PCB that is used for testing a single module in the laboratory. All of the described features in this section are applicable for lab-tests only because the beam test uses a different setup for data acquisition.

The teststand provides different features to test the modules and powers the module. It is connected to the module through an HDMI cable, whose plug (green) is hidden under the heat dissipater in figure 5.3. This HDMI is again connected to another MAX10-FPGA which communicates with the FPGA on the hexaboard and sends slow control commands to the module and receives data from it. The control software for creating commands and storing the data runs on a Raspberry Pi, which is connected to the FPGA through its General Purpose Input Output (GPIO) pins. This Raspberry Pi can be connected to a network and a client via its Ethernet port. The software that runs on the Raspberry Pi is described in the next section. The teststand also has a specific injection circuit where an adjustable pulse can be created and sent to the SKIROC2-CMS (but not to the silicon sensor) in order to test certain channels of the readout chip. This data acquired through charge injection is also crucial for the calibration of the detector. Especially the outermost silicon pads in the beam test are not hit often enough by the beam to have enough events for calibrating. This injection circuit can deliver more data for these channels.

5.4. Readout and Control Software

During readout of the ReadOut Chips (ROCs), information is merged together by the FPGA on the hexaboard and distributed over the GPIO pins of the Raspberry Pi for a faster signal processing. The Raspberry Pi is also the bottleneck in this readout chain since it allows only roughly ten events per second to be readout due to CPU constrains. This readout is controlled by fast-control commands which are distributed from the Raspberry Pi over the FPGAs to the chips. The before mentioned *stop-acquisition* is the main command that stops chips from acquiring data and starts readout. For configuration of the ROCs, slow-control commands are used, which are described in detail in the next

Component	Usage
USB-connector	data transfer between module and teststand, LV power supply for module
MAX10-FPGA	sending and receiving slow control and fast commands
Injection circuit	providing specific pulses to inject charge to sensor
Raspberry Pi	collecting data, sending configuration, connection to remote client
Power plug	Powering hexaboard and teststand

Figure 5.3.: The most important components of teststand are marked in colours. A short description is given in the table on the right

section.

5.4.1. Control-Server on the Raspberry Pi

Slow- and fast-control commands are both based on a GPIO-C-library that is compiled and optimized for a certain kernel version of the Raspberry Pi in order to have the fastest possible readout. However, the control software itself is written in Python.

Configuration

The python code reads configuration parameters from a dictionary (written in YAML-language) and merges it together into a 48-bit long bitstream for each SKIROC2-CMS which is then handed over to the C-library that pushes it via the I^{2}C-protocol to the chips. Table

5.1 describes the choosable parameters.

Parameter	Unit	Description	Usage
nEvent	-	number of events to acquire	configuration
externalCharge-Injection	-	turn on/off external charge injection	configuration
acquisitionType	-	selects trigger mode	configuration
channelIdsToMask	-	list of channels which are disconnected	configuration
headerSize	bits	size of the bitstream (one per chip or one for all)	data analysis
injectionDAC	DAC-counts	amount of charge to inject	configuration
pulseDelay	a.u.	pre-amplifier delay for shifting the pulse to peak in a certain SCA	configuration
totDACThreshold	DAC-counts	threshold for time over threshold measurement	configuration
toaDACThreshold	DAC-counts	threshold for time of arrival measurement	configuration
shapingTime	ns	shaping time of the preamplifier	configuration
moduleNumber	-	number of the module under test	storage
outputRawDataPath	-	path where binary data is stored	storage
outputYamlPath	-	path where configuration is stored	storage
storeYamlFile	-	turn on/off storage of configuration	storage

Table 5.1.: Most important configuration parameters.

Readout

For the readout, the Raspberry Pi receives a certain bitstream in a predefined format from the ROCs. This bitstream includes information from all four measurement circuits, plus some additional information and headers which are needed for the transport protocol. The description of these bits can be found in the appendix. This bitstream is saved bitwise in a binary file. This binary file is also the breakpoint between data-acquisition and data-analysis. The channel mapping and actual analysis are not done on the Raspberry Pi any more due to performance issues with the rather slow CPU of the Raspberry Pi. However, there is a plug-in, the so-called *unpacker* available, which puts the data into a readable format that can be printed in the terminal for debugging and to get a first impression of the data quality. The following steps are needed for this procedure:

1. cut off headers

2. map each bunch of bits per event with a certain chip, channel and SCA/ToT/ToA

3. read the roll mask in order to find out the first SCA-value in time

4. decode the Gray-encoded numbers to regular binary numbers

5. convert the numbers to decimal

6. print roll mask, channel and chip numbers and the respective SCA/ToT/ToA values

In order to map bits from the bitstream with physical silicon cells, the connections between cells and channels of the readout chip have to be defined. Figure 5.4 shows the electronic circuit diagram which gives exactly this information.
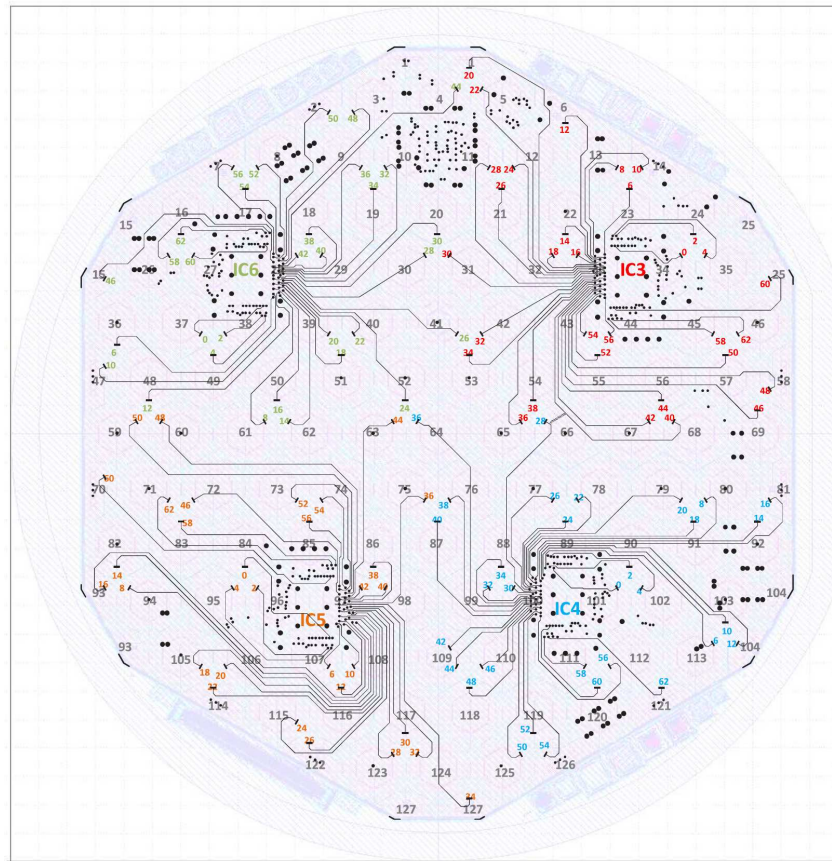

Figure 5.4.: Mapping between silicon cells and readout channels of the four SKIROC2-CMS (IC3-6) on a version 3 hexaboard. Grey numbers refer to the silicon pad numbers (1-127; printed on the silicon) while coloured numbers refer to readout channels of the readout chips (four times 0-63).

Pulse-shape

The RM is used in the unpacker to time-reorder SCA values. Those time-ordered values are now called time-samples (TS) in order to distinguish them from non-ordered SCA values. An example plot of these time-samples is shown in figure 5.5 and visualizes the pulse-shape of our signal. All of the channels are biased with a few volts in order to see negative pulses and undershoots as well. This bias-offset is called *pedestal value*.

The pulse in figure 5.5 shows a clear undershoot after the actual signal starting in time-sample 5. The lowest possible value is 4 ADC counts which is the default output of the SKIROC2-CMS if no signal is arriving.
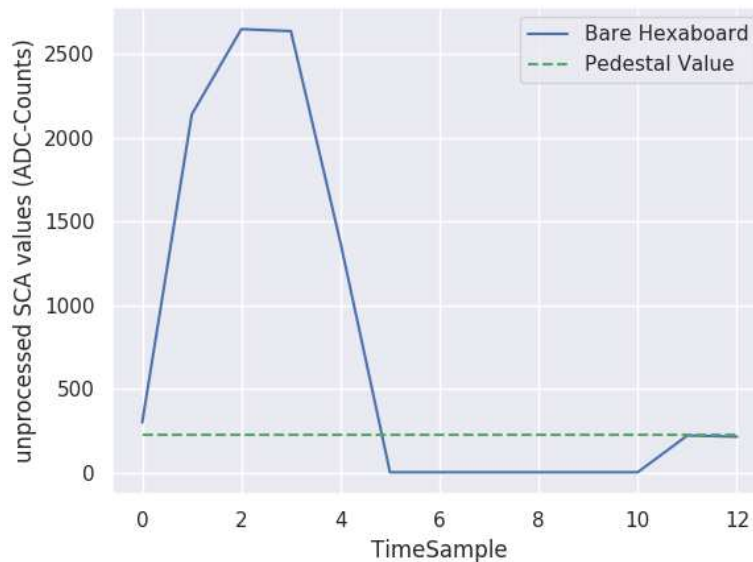

Figure 5.5.: Graphical representation of time samples. The dashed line represents the average offset which equals the pedestal value of channels. The flat shape of the undershoot after the pulse is due to a saturation of the ADC.

5.4.2. Control-Client

The readout system on the Raspberry Pi is not very fast and does not have a lot of functionalities. In order to improve handling and make more features available, a new client-server system has been developed. Therefore, the central update is the setup of a ZMQ-communication which is sending strings as commands to the Raspberry Pi via TCP protocol and also receives output from the chips over the network via TCP. This brings up a lot of new opportunities because the network gives a lot more possibilities of communication (ssh-access, storing data in network filesystems, ...) and the client PC can be used to implement a lot more features since it is more powerful than a Raspberry Pi. The following changes have been implemented:

- upgrading the system from Python 2 to Python 3

- a storage system on a CERN fileserver

- remote ssh access for quick debugging and launching the server on the Pi

- a plug-in for quick data tests which is needed for online data monitoring

- a configuration write-and-read loop in order to quickly repeat a measurement

- a draft GUI to have another input option besides command line arguments and the configuration file. Since it was not used at all, it was not further developed.

- a GPIB control system which can be used completely independently for an IV-curve and to change the bias-voltage of the sensor during data-taking in order to improve the automatization of the system

An example output of the plug-in for quick data tests is shown in figure 5.6. There are currently three tests implemented. Apart from the shown standard output, there is an option to print all values of channels, where at least one test failed or to print simply all channels. An example of this is given in figure 5.7.

```
                                                                Receive event  9
                        Receive event  9                        ******* RollMask-TEST
                        ******* RollMask-TEST *******   *********
                        Event = 9 Chip = 0 RollMask =                   Event = 9 Chip = 0 RollMask =
0xc00                                                    0xc
                        Event = 9 Chip = 1 RollMask =                   Event = 9 Chip = 1 RollMask =
0xc00                                                    0xc
                        Event = 9 Chip = 2 RollMask =                   Event = 9 Chip = 2 RollMask =
0xc00                                                    0xc
                        Event = 9 Chip = 3 RollMask =                   Event = 9 Chip = 3 RollMask =
0xc00                                                    0xc
                        ********* SCA-TEST *********                     ********* SCA-TEST ***********
                        Event = 9 Chip = 0 RollMask =                   Event = 9 Chip = 0 RollMask =
0xc00                                                    0xc
                        broken channels:[]                              broken channels:[]
                        noisy channels:[]                               noisy channels:[10, 10]
                        Event = 9 Chip = 1 RollMask =                   Event = 9 Chip = 1 RollMask =
0xc00                                                    0xc
                        broken channels:[]                              broken channels:[]
                        noisy channels:[]                               noisy channels:[10, 10]
                        Event = 9 Chip = 2 RollMask =                   Event = 9 Chip = 2 RollMask =
0xc00                                                    0xc
                        broken channels:[]                              broken channels:[]
                        noisy channels:[]                               noisy channels:[10, 10]
                        Event = 9 Chip = 3 RollMask =                   Event = 9 Chip = 3 RollMask =
0xc00                                                    0xc
                        broken channels:[]                              broken channels:[]
                        noisy channels:[]                               noisy channels:[10, 10]
                        ******* ToA/ToT-TEST *********                  ******* ToA/ToT-TEST *********
                        Event = 9 Chip = 0 RollMask =                   Event = 9 Chip = 0 RollMask =
0xc00                                                    0xc
                        Event = 9 Chip = 1 RollMask =                   Event = 9 Chip = 1 RollMask =
0xc00                                                    0xc
                        Event = 9 Chip = 2 RollMask =                   Event = 9 Chip = 2 RollMask =
0xc00                                                    0xc
                        Event = 9 Chip = 3 RollMask =                   Event = 9 Chip = 3 RollMask =
0xc00                                                    0xc
                        channels with ToA or ToT not                    channels with ToA or ToT not
4:                                                      4:
                        [[], [], [], []]                                [[10, 10], [10, 10], [10, 10],
                                                          [10, 10]]
```

Figure 5.6.: Two example outputs of the quick data tests using the client. A bare hex-aboard, without any sensor connected has been read out. The left side shows an output for a pedestal run, while the right side shows a run where charge was injected in channel 10 in all chips. This channels appears twice, once for HG and once for LG.

RollMask-Test

The RM can have 13 different values, representing 13 possible SCA- positions of the first value in time. This test checks if the RM has one of these 13 allowed values. The data is invalid, if the RM has any other value.

```
channelID = 12      214 219 219 218 216 216 220 216 222 221 219 228 227 4 4
channelID = 11      206 212 213 212 216 213 209 217 209 217 213 225 228 4 4
channelID = 10      228 693 1093 144 4 4 4 120 306 4 4 243 243 2376 2595
channelID = 9       230 236 229 222 237 225 229 230 235 228 233 243 235 4 4
channelID = 8       214 216 215 224 216 216 222 214 221 221 218 231 230 4 4
```

Figure 5.7.: Part of the optional output of the client that shows all values of channels. Charge has been injected in channel 10. This channel is also shown in figure 5.5

SCA-Test

Two different functionalities are implemented in the SCA-test. Firstly, it checks if the measured ADC counts are within a choosable range and defines a channel as noisy, if a certain number of SCA values is outside this range. Range and number of allowed values outside this range can be configured. This can be used to quickly find channels that have signal since those channels have higher ADC values than the normal signal from noise. Secondly, it checks if one of the SCA values is 0 which cannot be the case for a proper working channel because of the before mentioned electronic feature that allows only 4 as lowest value. If there is a 0, the channel is treated as broken. This tests only affects the first 13 values which come from the SCA, however, it does not consider the values of the last two SCAs because they are showing a systematic higher noise. This values are also not considered in the data analysis framework.

ToT and ToA-Test

The last two values of each channel are ToT and ToA. Also here, the minimal possible value is 4. Therefore, those two values should always be 4 if the threshold for ToT and ToA measurement is not reached. This test is simply looking for values that are not 4, in order to quickly detect channels with a signal. In figure 5.5 there is one channel detected with has both values above four. It is exactly the channel where charge was injected and thus ToT and ToA are firing. This can be used to exclude random events which have signal from some external source that is not wanted in pedestal runs.

More output from these tests as well as IV-curves taken with this system can be found in section 5.6.

5.5. HEXA8

HEXA8 is the working title for 8-inch prototype of the hexaboard which is a scaled version of 6-inch prototype, again using the SKIROC2-CMS and MAX10 FPGA communication. Pure hexaboards without any sensor attached are tested right after the assembly of components at Hybrid SA, the assembly company. Functionality of all readout chips, FPGA and other components are tested. The so-called data integrity, which represents quality and reliability of digital data, is measured by reading out pedestal values from the hexaboard. In order to assure reliability, long-term runs over a couple of hours are taken. For data quality assurance, this data is analysed with the above described quick data

checks. An example outcome of a fully working hexaboard is given below. All available tests are performed and no channel shows unwanted behaviour.

```
*********** RollMask-TEST *************
Event = 9          Chip = 0          RollMask = 0x600
Event = 9          Chip = 1          RollMask = 0x600
Event = 9          Chip = 2          RollMask = 0x600
Event = 9          Chip = 3          RollMask = 0x600
*********** SCA-TEST *************
Event = 9          Chip = 0          RollMask = 0x600
broken channels:[]
noisy channels:[]
Event = 9          Chip = 1          RollMask = 0x600
broken channels:[]
noisy channels:[]
Event = 9          Chip = 2          RollMask = 0x600
broken channels:[]
noisy channels:[]
Event = 9          Chip = 3          RollMask = 0x600
broken channels:[]
noisy channels:[]
*********** ToA/ToT-TEST *************
Event = 9          Chip = 0          RollMask = 0x600
Event = 9          Chip = 1          RollMask = 0x600
Event = 9          Chip = 2          RollMask = 0x600
Event = 9          Chip = 3          RollMask = 0x600
channels with ToA or ToT not 4: [[], [], [], []]
```

For three out of twelve tested hexaboards one or more readout chips are not working. As an example, the output of one event from a long term run for such a not working chip is given below.

```
*********** RollMask-TEST *************
Event = 9995       Chip = 0          RollMask = 0xc00
Event = 9995       Chip = 1          RollMask = 0xc00
Event = 9995       Chip = 2          RollMask = 0x8000
Rollmask Issue : impossible value (not 10..01, not 0..11..0, not 110..0, not 0..011)
Event = 9995       Chip = 3          RollMask = 0xc00
*********** SCA-TEST *************
Event = 9995       Chip = 0          RollMask = 0xc00
broken channels:[]
noisy channels:[]
Event = 9995       Chip = 1          RollMask = 0xc00
broken channels:[]
noisy channels:[]
Event = 9995       Chip = 2          RollMask = 0x8000
broken channels:[]
noisy channels:[63, 62, 61, 60, 59, 58, 57, 56, 55, 54, 53, 52, 51, 50, 49, 48, 47, 46, 45, 44, 43,
42, 41, 40, 39, 38, 37, 36, 35, 34, 33, 32, 31, 30, 29, 28, 27, 26, 25, 24, 23, 22, 21, 20, 19, 18,
17, 16, 15, 14, 13, 12, 11, 10, 9, 8, 7, 6, 5, 4, 3, 2, 1, 0, 63, 62, 61, 60, 59, 58, 57, 56, 55,
54, 53, 52, 51, 50, 49, 48, 47, 46, 45, 44, 43, 42, 41, 40, 39, 38, 37, 36, 35, 34, 33, 32, 31, 30,
29, 28, 27, 26, 25, 24, 23, 22, 21, 20, 19, 18, 17, 16, 15, 14, 13, 12, 11, 10, 9, 8, 7, 6, 5, 4, 3,
2, 1, 0]
Event = 9995       Chip = 3          RollMask = 0xc00
broken channels:[]
noisy channels:[]
*********** ToA/ToT-TEST *************
Event = 9995       Chip = 0          RollMask = 0xc00
Event = 9995       Chip = 1          RollMask = 0xc00
Event = 9995       Chip = 2          RollMask = 0x8000
Event = 9995       Chip = 3          RollMask = 0xc00
channels with ToA or ToT not 4: [[], [], [63, 62, 61, 60, 59, 58, 57, 56, 55, 54, 53, 52, 51, 50,
49, 48, 47, 46, 45, 44, 43, 42, 41, 40, 39, 38, 37, 36, 35, 34, 33, 32, 31, 30, 29, 28, 27, 26, 25,
24, 23, 22, 21, 20, 19, 18, 17, 16, 15, 14, 13, 12, 11, 10, 9, 8, 7, 6, 5, 4, 3, 2, 1, 0, 63, 62,
61, 60, 59, 58, 57, 56, 55, 54, 53, 52, 51, 50, 49, 48, 47, 46, 45, 44, 43, 42, 41, 40, 39, 38, 37,
36, 35, 34, 33, 32, 31, 30, 29, 28, 27, 26, 25, 24, 23, 22, 21, 20, 19, 18, 17, 16, 15, 14, 13, 12,
11, 10, 9, 8, 7, 6, 5, 4, 3, 2, 1, 0], []]
```

The fact that all tests fail for all channels in chip 2 leads to the conclusion that the whole chip must be broken. It cannot be a malfunction of the FPGA because other chips do deliver proper data. The impossible value for the roll-mask, which has to consist of twelve bits while just two after each other are ones and all the others are zero, cannot come from a wrong configuration either, thus further investigation is needed. Because of limited availability of measurement equipment at the assembly company, it was only figured out that one of the three not working chips was misplaced on the PCB and thus wire-bonds were connecting to wrong pins. This chip was replaced as well as the other
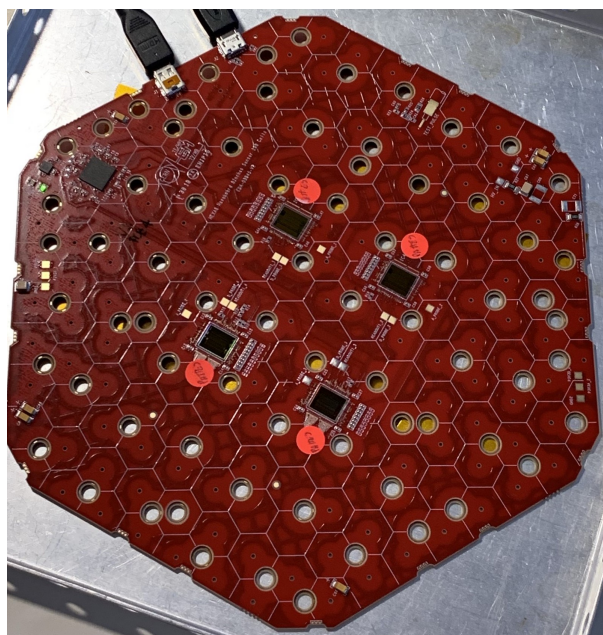
two not working chips.

Figure 5.8.: 8-inch prototype version of the hexaboard equipped with 4 SKIROC2-CMS. The cell size of full hexagons is identical with the 6-inch version. Additional cells are connected to odd input pins of the SKIROC2-CMS, which are not used in the 6-inch version.

5.6. Reception-tests

Roughly 70 modules have been shipped from USA to CERN during September 2018 which need to be tested before mounting them into the detector. This is important in order to assure that transport didn't harm the modules and to gain valuable information about their basic performance which is needed to safely run the prototype-detector. A structured approach for this measurements has been developed and is described in this section.

5.6.1. Visual Inspection and Hardware Setup

Before attaching a module to the test system, a visual inspection takes place as first step after opening the transport box. The majority of modules don't show any abnormalities, however, three modules with missing or dislocated electronic parts (such as a capacitor) are found. Those minor mistakes could be solved by re-soldering these parts manually. This very quick check is needed to quickly find potential problems and save time for other, longer measurements which would be useless if some electrical components are dislocated or missing. Afterwards, modules are connected to the teststand for detailed electrical tests.
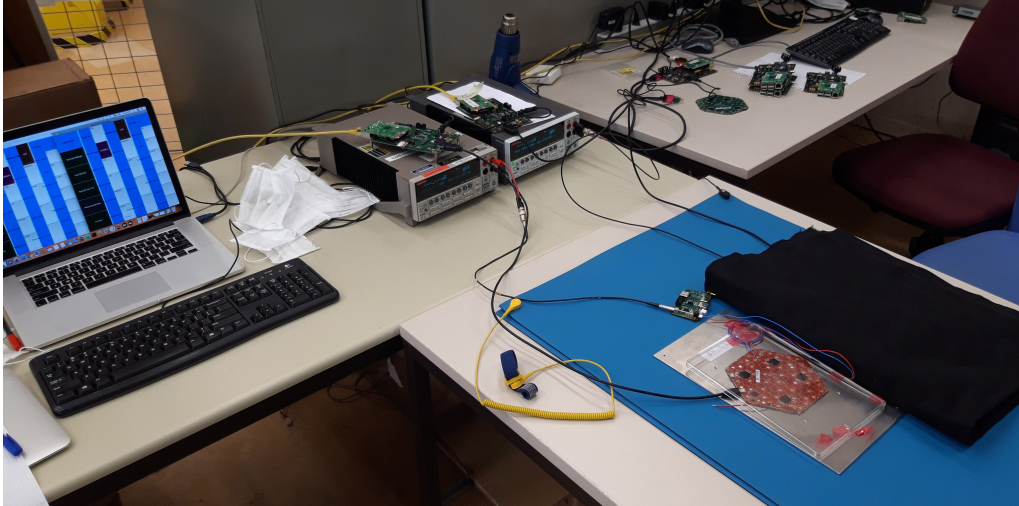
Figure 5.9.: The setup allows testing two modules at the same time. During operation, both modules are covered under black cloth in order to avoid light contamination. In this picture, just one of the modules is covered to demonstrate the full setup.

Modules are connected to teststands and operated as described in section 5.4. Two modules can be tested simultaneously. Two teststands are placed on top of two Keithley2410 Source Measurement Units (SMU) which are used to bias modules and for the IV-curve as seen in figure 5.9. The light protection is crucial for proper tests since silicon is sensitive to light which would create an unwanted, additional noise-signal. A Laptop is used as a client to control two SMUs and teststands simultaneously with the upgraded version of the software.

Interposer

A small PCB is used to connect teststand and module in figure 5.9. It has two different functionalities. On the one hand, it has two low-pass filters in order to keep the high voltage stable because the noise filter of the power supply is not sufficient for the tests. This has been seen during a previous beam test. Only the high voltage part of the interposer is connected for reception tests. On the other hand, it has voltage regulators which regulate voltage from 5 V down to 3.3 V which is the needed voltage for powering the electronic parts of the hexaboard. This is not needed for reception tests since the teststand can deliver the desired 3.3 V directly. However, during test beam, voltage loss due to longer cables would lead to a significant voltage drop, therefore the power supply delivers 5 V which are regulated down to 3.3 V by this interposers, that are located very close to the modules.

5.6.2. Data-Integrity and Noise

The next step is to test data integrity and noise performance. Therefore, so-called pedestal runs are taken, where the detector is just read out, without any external signal

induced in the silicon. 1000 events are acquired and tested online with the fast data-checks described in the previous section. Channel 22 in chip 3 is detected as noisy in all tests and has therefore been masked from readout. Masking a channel means that the pre-amplifier is disconnected and channels basically behaves like an unconnected channel. This issue has been known before and can be explained by noise coming from the HDMI-connector that is placed on top of this cell. Apart from this cell, most modules do not show any noisy or broken cells. One example of the very few bad modules is module 137, which is shown here:

```
Event = 21          Chip = 0          RollMask = 0x1800
channelID = 22      35 155 257 298 330 563 226 7 32 155 241 95 102 2514 4 (noisy)
channelID = 28      201 227 253 258 254 316 256 193 186 4 4 204 216 4 4 (noisy)
channelID = 22      4 4 4 514 802 2378 1113 4 4 4 4 125 122 1853 4 (noisy)

Event = 21          Chip = 1          RollMask = 0x1800

Event = 21          Chip = 2          RollMask = 0x1800

Event = 21          Chip = 3          RollMask = 0x1800
channelID = 44      99 165 227 255 267 421 266 98 93 131 230 146 145 4 4 (noisy)
```

This long version of output from the data tests shows three noisy channels. For these tests, a SCA values between 100 and 400 is considered as normal noise around the offset which is around 250 ADC counts. The first line shows that four values (35, 563, 7 and 32) out of the first eleven time samples are outside this range. Since a quite big range was chosen, a channel is considered as noisy if one or more values are out of this range. This criteria is met for all of the detected channels. Channel 22 in chip 1 appears twice because it is noisy in high gain and in low gain. The noise in this channel is also high enough to trigger the ToA measurement (which is the 14th number). As seen in the short summary that is printed in the terminal, this is detected as well, however, since this comes from noise, it is not explicitly mentioned in the output of the algorithm.

Some noisy channels in a module are expected and there is no reason to not include them in the detector. This applies also for full chips that are not working or delivering wrong data, which are detected by the same algorithms as well. Such failures are considered as a bad data integrity and important to know for reconstruction of data after beam test. According to these results, modules with a lot of bad channels have been put in the outer-most parts of the detector during beam test because these regions are not hit very often by particles and thus less data is lost due to noisy channels.

5.6.3. IV-Curve and Leakage-current

The last step of characterization of modules during the reception test is to take an IV-curve. The two most important outcomes from these IV-curves are leakage current at operation voltage and breakdown voltage of cells. Operation voltage during beam test is 250 V. This value is chosen to be inline with previous beam tests in order to make results comparable. Moreover this voltage should be above full depletion voltage. According to measurements during sensor testing, depletion voltage is around 200 V. It is also important to not chose the bias voltage too high. Some not working cells are expected. Those cells have a very high leakage current which is increasing with bias voltage and thus have to be treated separately.
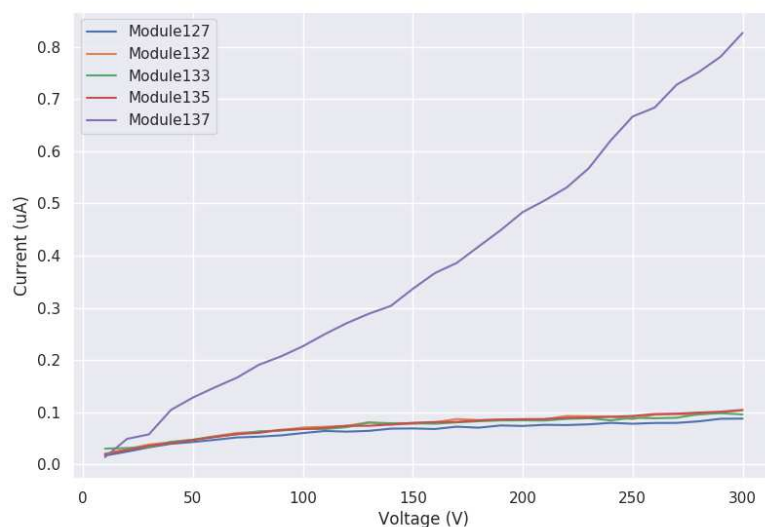
Figure 5.10.: IV-curves for a sample of five modules. Leakage current stays below 100 nA for most of the tested modules during the relevant range for the beam test (up to 250 V).

Figure 5.10 shows IV-curves of five modules taken during reception tests. Module 137 clearly shows a different behaviour than all other modules, therefore further investigation is needed. Linear increasing leakage current is a hint for a not proper working cell that is breaking through a very low voltage. The breakdown voltage of all silicon cells should be above 800 V, thus the module is biased with a higher voltage to find the breakdown point. Although this point is at 450V, which would be high enough for a stable operation during beam test, it was decided to treat this module as breaking through. Modules with a high leakage current are heating up the detector on the one hand which leads to a unstable temperature which effects the performance of the detector. On the other hand, the power supplies can only deliver a certain amount of current, therefore the modules with a high leakage current get a dedicated channel of the power supply during beam test in order to assure enough current and to monitor current during operation, while normal working modules are grouped together to one channel of the power supply.

5.6.4. Final Result

The outcome of the above mentioned tests is a big spreadsheet containing all important information in a compact and easy-to-use way. With this information, layout of the detector is decided even before the actual detector is built. Modules with a high leakage current get a separate power line and modules with a lot of noisy cells will be put in outer regions of the detector where less particles are detected and thus the loss of data is decreased. It is important to decide the layout of the detector based on this tests before building it because it is not easy to re-arrange modules or connections during operation.
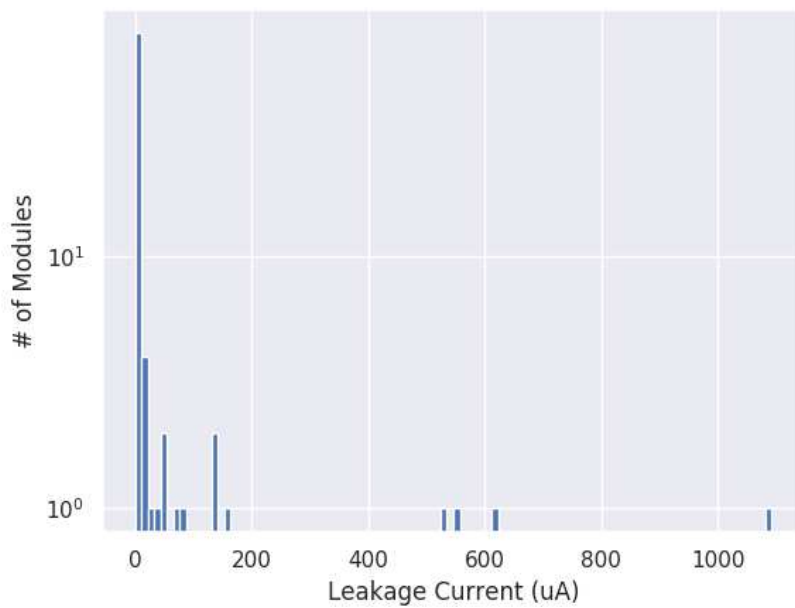
Figure 5.11.: Summary of the leakage current for all of the measured modules during reception test. 250 V bias voltage are chosen as reference point for this measurement. The cut between 'good' and 'bad' modules is chosen at 300 μA. Modules above this threshold are treated separately to assure safe and stable operation during beam test.

6. HGCal Test Beam

6.1. Aim of Test Beam

The aim of the test beam can be summarized to two main points. Firstly, proof of concept and system validation, showing that a full on-to-off-detector using a stack-up of silicon modules can be built. Secondly, gaining experience on hardware, data acquisition and data analysis is not less important in order to operate the final detector.

6.1.1. Specific goals for the October 2018 Test Beam

This section very briefly explains conceptual goals of this specific test beam. Previously, test beams at CERN north area and DESY in Hamburg were focussing on external noise suppression and position resolution, thus those topics got less priority during this test beam.

Scalability is the first factor that needs to be tested during this test beam. So far, there have been maximum 20 modules used at the same time. Upscaling to the order of 100 modules demands scaling of DAQ hardware and software as well in order to handle the higher number of modules. Renewal of the DAQ-system goes hand in hand with higher power consumption and bigger secondary infrastructure. Moreover, a new Detector Control System (DCS) for monitoring currents and temperature throughout the detector as well as a Data Quality Monitoring (DQM) system for a online control of the data quality were needed to assure safe and reliable behaviour of the detector during beam test operation.

With the high number of modules, it was possible for the first time to build and run the hadronic subsystem simultaneously with the electromagnetic sub-detector and a prototype of a scintillator based detector. Thus, electromagnetic and hadronic performance of the detector are studied in detail in the test beam analysis. The calculation of X_0 and λ_I for different sub-detector are crucial for calculating energy. So are reconstruction of shower shapes, particle tracks and jets as seen in section 2.2.

Noise behaviour for different cell types, silicon-sensor thicknesses according to section 4.5 and different baseplates are studied during this test beam. Most of the baseplates are made of copper, but some modules have copper-tungsten baseplates where others use a double layer of kapton or PCB material as baseplate.

Results from the beam test are compared to results from sensor tests whenever possible.

6.2. Building the HGCal prototype detector

The whole detector is first build and operated in the laboratory in order to test the full chain including DAQ before the actual beam test. Therefore, the detector is setup as it will be in the beam area and pedestal runs are taken to check power and data connections to assure data integrity. The three main components of the system are the electromagnetic and hadronic sub-detector as well as the DAQ-system

6.2.1. Mini-Cassettes for the Electromagnetic Calorimeter

The electromagnetic section is built already quite similar to the final detector. So-called mini-cassettes have been built and tested during a previous test beam already. A picture of a cassette is shown in figure 6.1. The electromagnetic section basically consists of a
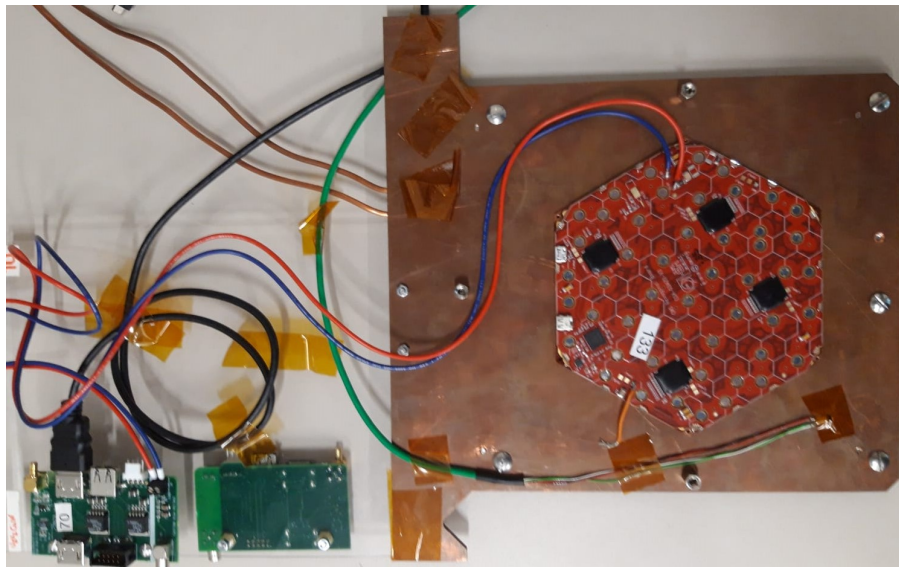
Figure 6.1.: One side of a mini-cassette showing the module, a temperature sensor and the interposer. On the left side, the backside of a second interposer is visible, which is connected to the module on the backside of the copperplate.

copperplate used for cooling and a mechanical support plate which has a module mounted on both sides as the active part and copper-tungsten absorber plates in between those, serving as absorber. Details of this design can be found in [4, pp. 58, 59].

6.2.2. 'Flowers' for the Hadronic Calorimeter

Layout of the hadronic part of the detector is completely renewed for this test beam. The final result is called 'flower' and can be seen in figure 6.2. Many mechanical details have to be considered during construction of such a flower. A lot of tests and considerations from mechanical and electronic perspectives were needed and the final results are presented here. Firstly, the module in middle has to be lifted a few millimetres because the
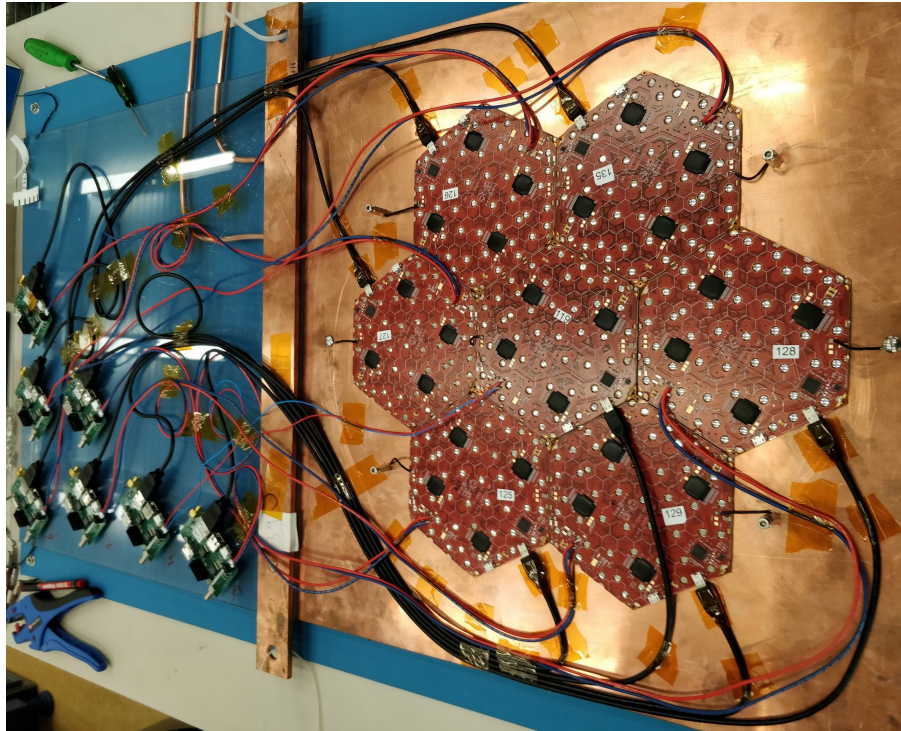
Figure 6.2.: Picture of one layer of the hadronic part of HGCal. Due to it's shape, these plates are called 'flower'. One flower consists of seven modules and interposers which are all on one side of the copperplate.

rather flat micro-HDMI connector is directly on top of the PCB and the plug wouldn't fit in any more. Secondly, modules in the middle are rotated according to their position such that the connector is always on the outside of a module. The right side is connected on the top, for a shorter distance to the interposer. As seen in figure 6.2, the left side is connected from the bottom side to avoid bending the HDMI cable. It is crucial for the trigger that all cables have the same length. Thus, the way from each interposer to a module has to be the same and within the flexibility of cables. Lastly, interposers are placed in different distances to the modules in order to cope with the above mentioned issues and keep the cable length the same for every module. Interposers are mounted with a 45° angle to be able to reach them when plates are stacked next to each other, which can be seen in figure 6.2

It has to be mentioned, that this design differs from the shown design in figure **??** where another PCB and copperplate are shown. The second PCB (the motherboard) and its support copper plate are missing in our prototype-detector because design is not yet finalized and modules are read out by a special DAQ constructed just for this beam test.

6.2.3. DAQ-system

The DAQ-crate was designed for this test beam and is based on the teststand-system used for reception tests. Details are given in [16]. The system, as shown in figure 6.3, consists of readout boards which can read out eight modules simultaneously (instead of one compared to the teststand) an one synchronization board which acts as a master synchronizing the data taking from the readout boards. Coincidence of two scintillators triggers readout, however certain sub-detectors can send a veto signal in case they are not ready for readout.

Each module is connected by two cables, one for the high voltage supply and one for
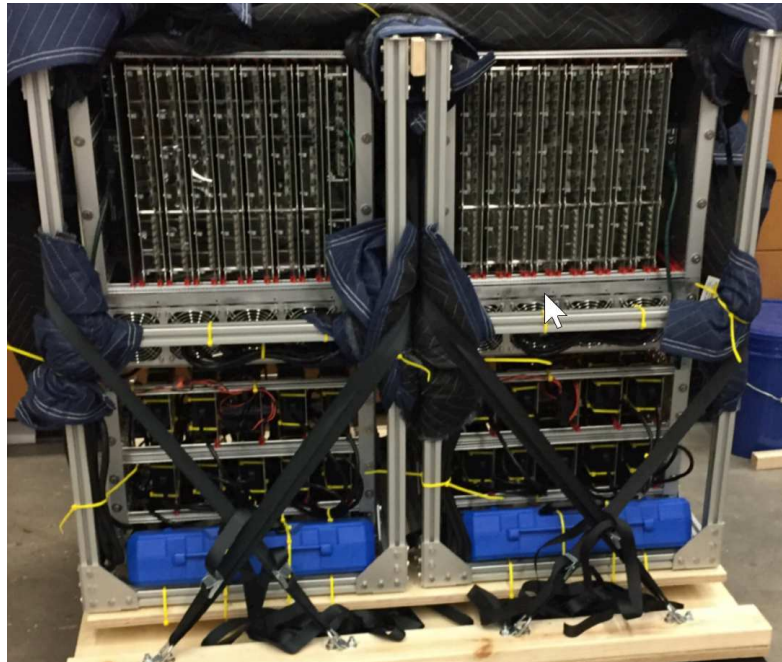
Figure 6.3.: Front-view of the DAQ system, showing 15 readout boards and one synchronization board on the top and power supplies on the bottom. One can power and read out up to 120 modules with this DAQ crate.

low voltage supply, control commands and data lines. Together with 16 Ethernet cables that are used to transfer data from readout boards to the synchronization board and storage disks, there are roughly 200 cables used which have to be all correctly in place. Structured cabling is a big challenge and a single dislocated cable would mix up signal reconstruction in the software. DAQ-software provides a way to check online if all cables are connected correctly, however, a dry-run in order to practise cabling before beam test is needed to speed up construction at beam area.

6.3. Setup and Beam Test at CERN H2 North Area

The beam test took place at the H2 beam line at CERN north area in the Prevessin site in October 2018. Over 50 people from institutes all over the world took part in the beam

test.

6.3.1. HGCal and AHCAL

The main device under test (DUT) is, of course, the HGCal prototype detector. A picture of the setup of the silicon part of HGCal is shown in figure 6.4. Behind (meaning downstream in the beam line), which is the right side in figure 6.4, there is the AHCAL detector from the CALICE collaboration, which is based on scintillators. The hadronic part of HGCal will have a scintillating part after the silicon part as well, thus the AHCAL detector was used in this beam test to show the possibility of a common, synchronized trigger and readout system between the silicon part of HGCal and a scintillating detector.
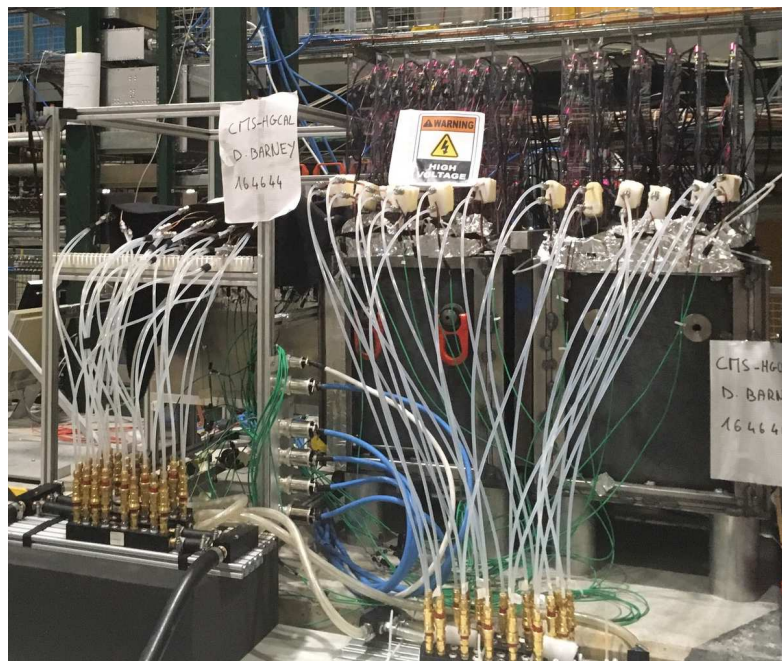
Figure 6.4.: Side view of the HGCal detector. Every layer is connected to the cooling system with white pipes. Beam direction is from left to right. AHCAL is completely covered in black cloth and thus not in this picture.

The beam hits the electromagnetic part first, this part consists of mini-cassettes as described in section 6.2.1. Between cassettes there are 4 mm copper tungsten layers which serve as absorber for the ECAL prototype. The radiation length X_0 of all absorbers summed up is around $25\,X_0$. Cooling pipes are integrated in the copper plates that hold the modules.

The hadronic part of the detector uses 4 cm of stainless steel as absorber material in between flowers and is located after ECAL prototype. The summed up interaction length equals roughly $4\,\lambda_\mathrm{I}$. Unlike ECAL prototype, cooling pipes are connected on the backside of the copper plates. The different baseplates mentioned in section 6.1.1 have been put in the HCAL prototype mostly.

Event-Displays of the HGCal prototype

Every particle needs to be stopped completely in the detector in order to record its full energy. Hadronic showers are usually much bigger than electromagnetic showers, thus the hadronic part needs more absorber material to stop particles and a bigger circumference due to higher Molière-radius of hadrons. The first issue is addressed by taking 4 cm of steel instead of 4 mm copper tungsten as absorber. The second issue is addressed by the flower structure, which covers an lateral area that is seven times bigger than the electromagnetic part.

It is important to plot event displays to see where energy is deposited. The ideal case is that no energy is deposited in outermost regions of layers and no energy deposit in the last layer. The latter criteria is not quite the case as seen in the event display for a 300 GeV pion in figure 6.6. Thus, the AHCAL detector afterwards catches and records the residual energy of such 300 GeV pions.
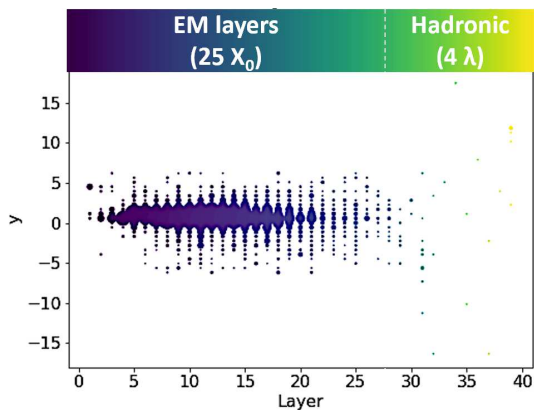
Figure 6.5.: The event display of a 200 GeV electron shows that electrons are mainly interacting with the electromagnetic part.
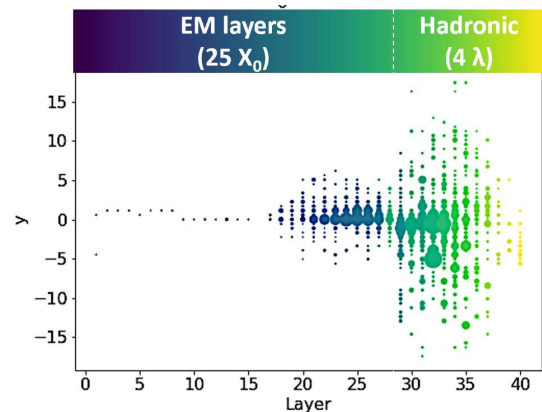
Figure 6.6.: The event display of a 300 GeV pion shows that hadrons are mainly interacting with the hadronic part of the detector.

Figures 6.5 and 6.6 show shower shapes for different particles at similar energies. As seen in the plots, almost no energy is lost in the outer regions. Electron showers are quite narrow and only present in the ECAL prototype. The HCAL prototype unfortunately can not completely catch the full pion showers since 4 λ_I is not enough to stop the particle completely. Taken AHCAL into consideration, this situation improves because AHCAL has a tail catcher dedicated for this. Thus, a joint readout of the silicon and scintillating part is very important in order catch the full energy of hadrons.

6.3.2. Other Detectors

HGCal and AHCAL are not the only detectors in the beam line. Beam monitoring detectors as well as reference signals from other, calibrated detectors are needed in order to validate measurements with HGCal. The other instruments in the beam line are also readout synchronously and consist of:

- Cerenkov-Detectors for particle identification (ID)

- Multiwire Proportional Chambers (MWPC) for the beam position measurements

- Multi Channel Plates (MCP) as a timing reference measurement

- Scintillators for triggering

6.3.3. Secondary Infrastructure

In order to safely operate several detectors simultaneously, more infrastructure is needed. The aim of this secondary components is to keep the detector in stable environmental conditions and to monitor the state of the detector. Figure 6.7 gives an overview of the most important secondary components and explains why they are needed.

6.3.4. Data Taking and Shifts

This section is meant to be a bit more informal in order to describe how the HGCal detector is operated, how to assure good data quality and guarantee a safe environment. Preparation, including training for all users during test beam is fundamental in order to have a successful beam test. Some considerations and instructions for preparation of people and running the detector safely are given here.

Training and Operation of the detector

The test beam took part in October 2018 for 14 days non-stop. Over 50 people are involved in preparation and operation of the HGCal prototype detector. Operation of the detector was divided in three eight hour shifts for each day (and night) non-stop over the whole period, except one day when the beam line was shut down due to a technical stop. At least three people have to be in the control room at any time, consisting of two people from HGCal, who are responsible for the overall running of the detector, steering beam and safety, and one person from AHCAL who is responsible for running the AHCAL detector. In addition, experts and responsible people for the subsystems have to be available on call 24/7.

The main work during a shift is taking data and monitoring data quality. Beam line experts prepare so-called beam-files which consist of ready-made parameters for magnets and targets in the beam line to produce a beam with a certain type of particle, energy and profile. The primary beam from the accelerator, the Super Proton Synchrotron (SPS),
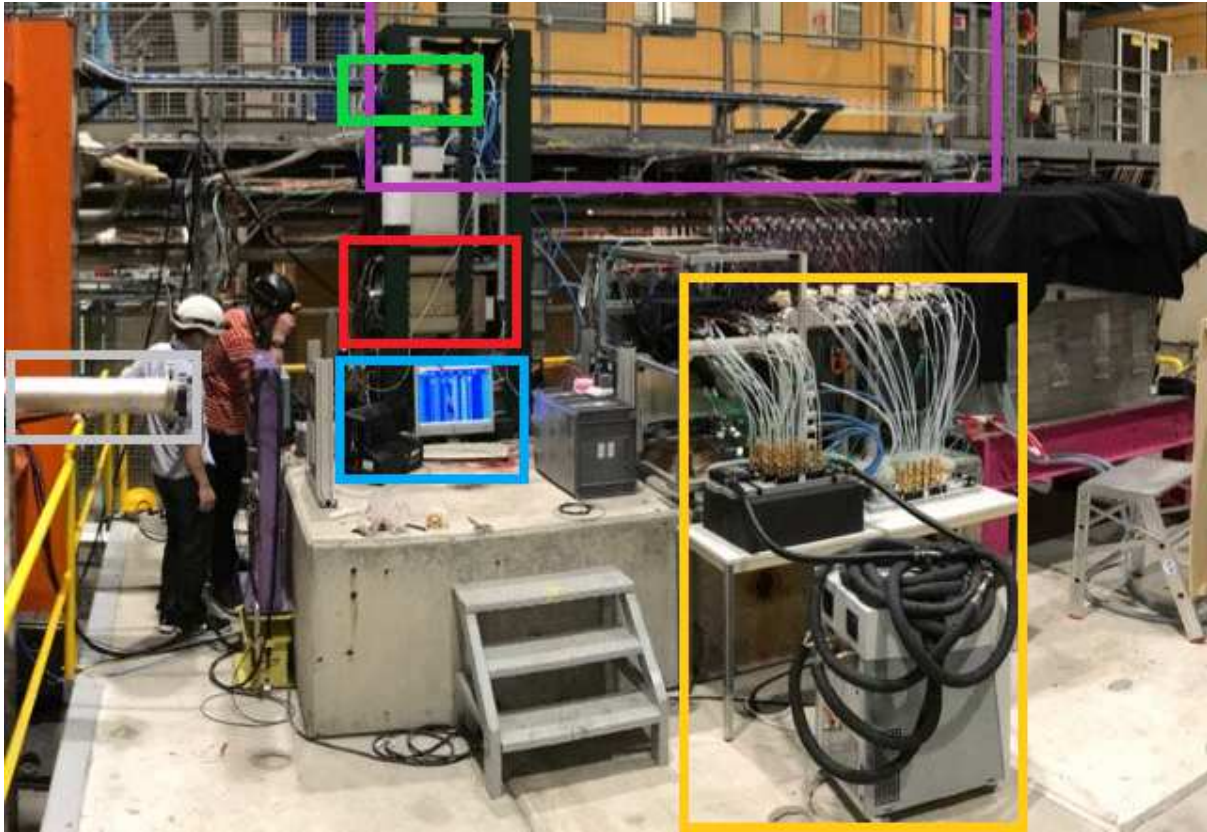
Component	Usage
beam pipe	beam injection
temperature control unit	keeping temperature stable
trigger logic	triggering the readout
DCS system, LV and HV supply	monitor temperature and currents, power supply for detector
connector of temperature and humidity sensors	part of DCS system
control room	accommodate shift screw
dry air supply (not shown)	keeping humidity stable
DAQ-crate (behind HGCal)	data acquisition

Figure 6.7.: Full setup at the H2 beam line in the CERN north area, including secondary infrastructure of the HGCal prototype.

consists of protons which are converted into pions or electrons (secondary beam) by hitting a target. The energy range for this beam test was 20 GeV to +300 GeV (positive and negative) for pions and electrons (respectively positrons for the positive energy). Particle type and energy are chosen beforehand and the shift crew has to load the corresponding beam file in order to setup all magnets to produce the desired secondary beam. Beam monitors are available to observe beam profile. The beam comes in packets of protons, so-called bunches, and an acoustic signal indicates when there are bunches arriving in

the beam line. This has to trigger readout of our detector. The DAQ system has implemented software that shows if a beam is present, which has to match with the signal from incoming bunches. The EUDAQ-framework [17] was used in order to acquire this huge amount of data. This differs from laboratory tests where teststand and Python framework are used. EUDAQ requires a certain data format, thus data has to be converted back into the 'SKIROC2-CMS '-format B in order retrieve channel numbers and other information from it which is needed in the analysis framework. Moreover, EUDAQ comes with a so-called run control, which is a graphical interface to configure readout chips, start a run, save and monitor data. All abnormalities need to be reported. Thus, a log-file has to be written by the shift crew containing all unusual behaviour of beam monitors and run control. In addition, a run-list is written where run parameters (run number, number of events taken per run, particle type, energy and changes in settings) are recorded.

Safety is always the highest priority, thus currents from power supplies as well as environmental data (temperature and relative humidity) are recorded independently by the detector control system (DCS). This data is also important input for studies on temperature dependence. However, especially the current of power supplies is important to monitor with respect to safety, thus an extra list needed to be filled regularly by hand by the shift crew in order to have a second independent source of this data.

Another task of the shift crew is general operation of the control room. This includes:

- Regular control of the beam area to assure that nobody is in the area and check if there are any visual signs of damage.

- Handling request and demand actions from the accelerator control room if needed.

- Open beam area and guarantee safe working in it on request of the beam test responsible for minor, unavoidable work directly at the detector (changing configuration) and fixing problems.

- Taking care of any other test beam related issue that occurs during the shift.

Overview of Data Output

Configuration of the detector changed twice during test beam because there are not enough modules available to fill the full detector. A configuration with a fully filled electromagnetic part, a fully filled hadronic part and a mixture of both are realized during test beam. A visualization and further details can be found in Appendix C.

Over *six million events* have been recorded during test beam. Figure 6.8 shows the number of events per particle type. As mentioned in section 6.3.2, there have been more detectors in the beam line than just HGCal. It was not possible to operate all of them from the beginning onwards, thus they have been assembled later during the beam test as shown in figure 6.9.

Overall performance and amount of data recorded during test beam was extraordinary high and which is why the beam test is considered as a huge success, delivering a high
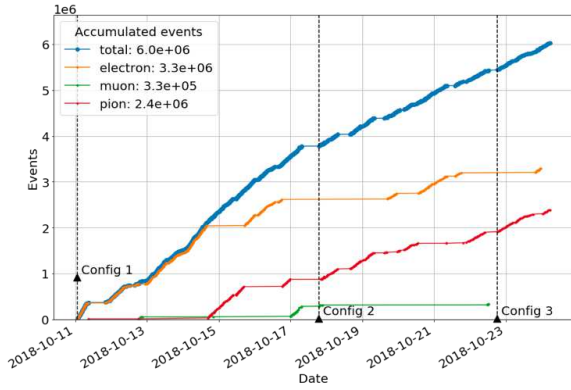
Figure 6.8.: Number of events per particle type. The vertical lines indicate the change of configuration. Moreover, the horizontal lines in the blue curve show the downtime of the detector, mostly due to the non-availability of beam. Plot taken from [18]
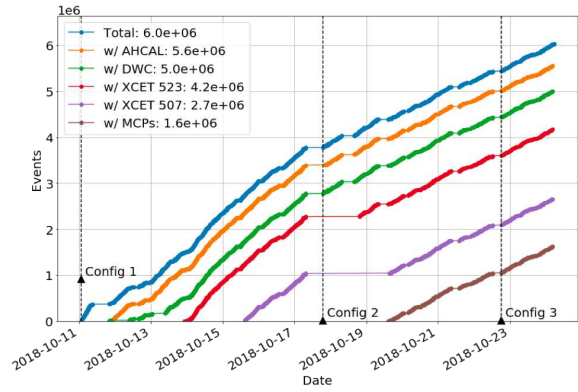
Figure 6.9.: Number of events taken per sub-detector. The total number corresponds to events of the HGCal detector. The starting points of the curves indicate at which day the detector was operational. Plot taken from [18]

amount of data (compared to previous test beams). In fact, most of the downtime was due to beam line issues and not due to the HGCal prototype. Cooperation between different groups of CERN and students from universities all over the world during beam test worked very well and it was a nice and comfortable environment to work with.

56

7. Analysis of Test Beam Data

7.1. The Analysis Framework

Input for the data analysis framework is the bit-file which is created by the SKIROC2-CMS and readout software. Data structure and channel mapping are described in section 5.2.1. The analysis framework is written in ROOT, containing a fast, complied C++ part for actual calculations and a python-script for input and output handling. It is part of the CMS-software (CMSSW) package.

7.1.1. Data Flow and Overview

Each chip sends 1924*16 bits per event. The bitstream of four chips is gathered by the FPGA on the hexaboard which sends it to a readout board. Each readout board receives data from up to eight modules. This data is than wrapped into a certain format that is needed form the DAQ software EUDAQ. This data is finally readout by an EUDAQ producer and un-wrapped into one bitstream for each module again in order to reproduce the SKIROC2-CMS memory map and stored in a root TFile. This TFile serves as input for the actual physics analysis in ROOT. The following steps describe shortly what is done during this analysis.

Step 0: Converting data from raw ROOT-files into a so-called CMSSW-collection which is needed in order to run analysis with the CMSSW framework.

Step 1: Compute pedestal and noise values.

Step 2: Subtracting pedestal value and re-order SCA values in time to get the time samples. Data after this step is stored in the so-called 'RawHit'-collection.

Step 3: Calculating and subtracting the common - mode noise (details in the next section)

Step 4: Fitting a pulse shape through the time samples for energy calibration. The amplitude is proportional to deposited energy.

Step 5: Calibrating and selecting the different gains. Each energy interval uses only linear parts of each gain (high gain, low gain and ToT). Data after this step is stored in the so-called 'RecHit'-collection (Reconstructed Hit). This is the final step before physics analysis.

7.1.2. Main Analysis Goals

Data analysis from test beam data is divided into two big parts. On the one hand, there are studies on reconstruction and calibration which focus on stability and improvement of the methods to produce a RecHit as described above. It is important to understand as much details as possible here because these are fundamental values on which the whole analysis is based on. It influences the detector performance and accuracy. One the other hand, studies on physics performance of the detector are given. These studies rather focus on energy resolution and performance for different particles than on specific detector-dependent phenomena. A brief overview of studied topic is given here, however the rest of this chapter focusses on pedestal calculation and noise behaviour which was chosen as main study for this thesis.

Reconstruction and Calibration

Different methods on how to estimate common mode noise, which is intrinsic noise of silicon sensors that affects the whole sensor at the same time, and how to quote the residual noise are part of the *noise and pedestal* study. This also includes pedestal calculation which is a constant offset for each channel that is applied to the ADC in order to record undershoots as well. Dependency of noise behaviour on environmental aspects and geometric position is studied as well.

The *calibration* of HG, LG, ToT and ToA is an important part of reconstruction in order to get conversion factors between measured ADC-values and energy (in terms of MIPs). Conversion is done relatively with respect to the other gains as a first step, which means ToT is converted to LG and LG is converted to HG by scanning through the full range of gains. HG is than calibrated with MIP signals coming from muons. These are rather constant over the full range of energy as described in section 2.1.1. Different methods using data from test beam and injection test as well as stability of the conversion are studied as well.

The last part of this study are *electronic effects*. A so-called baseline-shift occurs when a very high energy deposit in one chip draws a lot of current and the power supply is not able to keep voltage stable for other chips. This behaviour is not fully understood yet and studied here, apart from the so-called crosstalk effect. Crosstalk effects occur when independent silicon channels are electronically coupled which might affect performance because channels, that are actually not hit show a signal in this case. Channels are AC-coupled by design of the silicon pads: The inter pad distance (together with the connection to ground or high voltage over intrinsic resistance of silicon) behaves like an AC-coupling. There might be similar couplings in electronic parts of the readout chip which are also part of this study.

Physics Performance

Simulation is used in order to simulate our detector and beam to verify data we get from the experiment.

Main focus on physics performance is measuring different aspects of electron and hadron showers. Shower shape, Molière radius, energy resolution and efficiency studies are done for both particles. Moreover distinguishing between an electronic or hadronic shower and a jet is part of the *pion and electron studies*. The impact of different techniques used for reconstruction and calibration as well as more advanced studies such as energy linearity and clustering are done as well for both particle types.

The last part are timing studies which focus on timing performance of the detector using ToA measurements. Comparison with MCP-data and simulation are crucial for this study. Timing is one of the big innovations of the HGCal detector, thus there are hardly any other similar setups where results could be compared to. Additional, independent detectors and simulations are thus the only reliable references.

7.1.3. Energy Resolution of the HGCal Prototype Detector

As mentioned in section 2.4, energy resolution is the driving parameter while operating a calorimeter. After calibrating data, fitting the pulse shape and reconstructing energy deposit for each cell, one can plot the energy resolution of the detector. An example output for electrons as incoming particles with a range from 20 to 300 GeV is shown in figure 7.1.

By fitting the curve in figure 7.1 to the general equation for energy resolution 2.6, one can
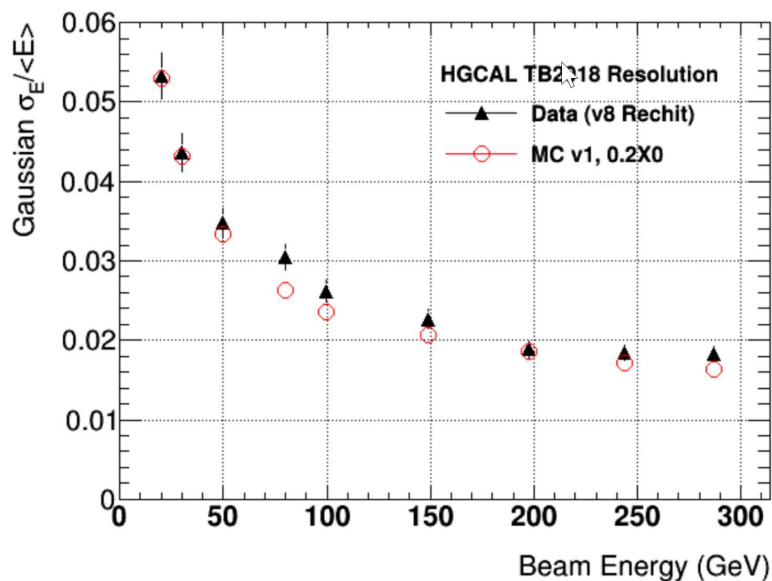
Figure 7.1.: Energy resolution for electrons during test beam and Monte-Carlo (MC) simulation. The two curves agree with each other quite well, which proofs that reconstruction and calibration work accurate.

retrieve the parameters a,b and c. This has not been done yet because the disagreement of data and simulation around the 100 GeV region is not fully understood yet. However,

such values have been calculated with simulation data for a final design already, which are given in equation 7.1 for a 100 GeV electron, according to [4, p. 73]. The b-parameter is not shown, since it mainly depends on the readout electronics.

$$\frac{a}{\sqrt{E}} = 2.4\%$$
$$c = 0.5\% \tag{7.1}$$

Comparing values from the electromagnetic part of HGCal (equation 7.1) to the current CMS ECAL (equation 2.7), the resolution will be worse. However, energy resolution is still good enough to reach the desired performance for the electromagnetic part. The increase in granularity decreases energy resolution, but also enables particle flow analysis, which is desired for HGCal.

7.2. Common Mode Noise for non-standard Cells

This project is focussing on noise studies which connect the readout system of the test beam with measurements for sensors in the cleanroom. This setup is described in section 8.1.1, followed by the measurements. In this chapter, studies on noise for modules are done, which can be considered as a requirement for studying sensors, however, they still deliver valuable analysis output on their own as well. An introduction to statistical methods and effects is given using the calculation of pedestal values as example. However, the same principles apply to noise calculation as well. The last part focusses on the noise for non-standard cells which have not been studied in detail during previous test beams.

7.2.1. Robust Statistics and Pedestal Calculation

Pedestal values, or, in short, 'pedestals', of our detector are offset values of every readout channel that occur due to a small offset, which is applied to the ADC in order to see undershoots and negative pulse shapes. This offset voltage is treated as independent from time and is calculated for every readout channel separate since it depends on the chip, via length and smaller effects like electronic crosstalk. The pedestal value is calculated by reading out in the order of 1000 events during a pedestal run (without signal) and computing a average of this distribution for each SCA. A good pedestal run needs coverage to protect it from light and stable environmental conditions. This is not possible during test beam due to changing humidity and temperature which cannot be avoided over a long time. Thus, the 25 ns time bins for readout are chosen such that the first bin records data before signal arrives and only this time sample is considered for calculating a pedestal value. This includes a big loss of statistics because the first time sample is stored in random a SCA from 13 circular arranged SCAs. Thus, one gets roughly one value every 13 events for the pedestal distribution of a readout channel. This differs from real pedestal runs in the lab, where no signal contamination can be guaranteed and the first seven time samples are used.

Using different averages and their effect on the pedestal distribution was studied in detail

during this thesis. There are two possible options to calculate an average of a distribution which are the *mean* and the *median*. The distribution of residual SCA values after subtracting pedestals using mean and median is shown in figure 7.2. SCA values are given in ADC counts, thus those are integers and the binning is chosen with bin edges at integer values. This explains the slight shift to the right when using median: Values exactly between two integers are likely to occur and are always counted to the right bin while the value is hardly never exactly half of an integer when using mean which makes the distribution more centred around 0.

For well behaving data, which doesn't have signal contamination or other irregularities,
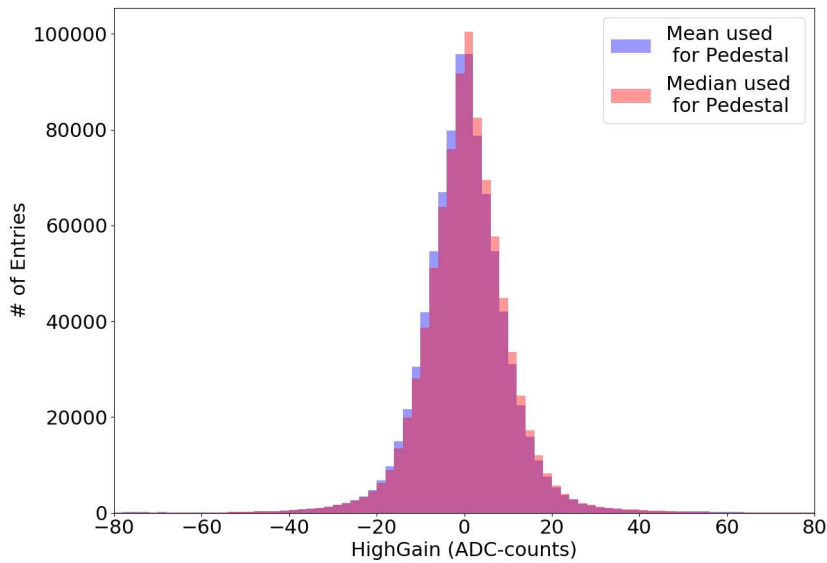
Figure 7.2.: Distribution of calculated SCA values after subtraction of pedestal values using two different averages for Module127. The number of entries in the whole histogram summed up is 1.664.000 which equals 128 channels times 13 SCAs times 1000 events.

there is no reason to not used the mean for pedestal calculation. However, disturbances due to noise or unwanted signal occur during test beam. Thus, the median is used because it is less sensitive to outliers (The outliers do not affect the value of the median). Due to their *robustness to outliers*, median and inter quartile range are robust measures for the centre of a distribution while mean and standard deviation are not.

The following points sum up calculation of pedestal values:

- The pedestal value equals the average over many events without signal

- Pedestals are computed for every SCA separately

- Time sample 0-7 are used in lab tests, only time sample 0 is used in test beam

- Mean is used for average in lab tests, median is used for test beam

7.2.2. Common Mode Noise for standard cells

Common mode noise (CMN) is noise that is *common* to all cells of a chip or the full sensor. It can be caused by a slight change in the power supply, for instance. It is not part of the signal actually coming from a particle, thus, CMN needs to be calculated and subtracted before data is used for analysis and performance studies. A new plug-in for the CMSSW framework used for analysis of data has been written during this project. It provides a lot of options and calculation methods which are used and described in this section. It can handle lab data as well as test beam data.

Common Mode Calculation

Common mode is time dependent and thus calculated per time sample. It catches eventual changes in bias voltage for every time bin, thus it is calculated and subtracted 13 times for every event, once for every time sample. Only full cells are considered for this calculation, thus there are only roughly 100 values available to calculate common mode. Common mode is defined as average over the distribution of pedestal-subtracted SCA values of full cells per time sample. As for pedestal calculation, mean and median can be used with the same consequences. This implies looping over events twice. Pedestals have to be calculated first, which needs input from all events, while common mode needs to be subtracted afterwards for each event, which requires another loop over events. This uses quite a lot of CPU power, thus this step is an optional plug-in dedicated for noise studies and not used per default in data reconstruction.
The effect of pedestal and common mode subtraction can be seen in figure 7.3, which shows the distribution of pedestals before and after every step.

Statistical Considerations

An ideal pedestal run should give a pure Gaussian distribution centred around zero. Thus, the peak-width in figure 7.3 can be considered as noise of the sensor. However, this measure would sum up all cells which is not wanted. Thus, noise is defined as width of the SCA distribution after pedestal and common mode subtraction *for each SCA*. Width of the distribution can be defined by inter quantile range (IQR), which is a robust measure or by root mean square (RMS) which is not robust. RMS equals the σ-value for a Gaussian distribution which gives the inner roughly 68% of a distribution which equals edges at 15.8% and 84.2%. In order to make values of RMS and IQR comparable and to stick to the sigma notation (the distribution is Gaussian in the ideal case), edges of the IQR are also chosen to be at the same percentage, although usual values for IQR are 25% and 75%. Two example distributions with a pure pedestal run with and without disturbances can be seen in figure 7.4 and 7.5, which the different behaviour of IQR and RMS. This distribution should have 1664 entries which equals 13 SCAs times 128 channels.
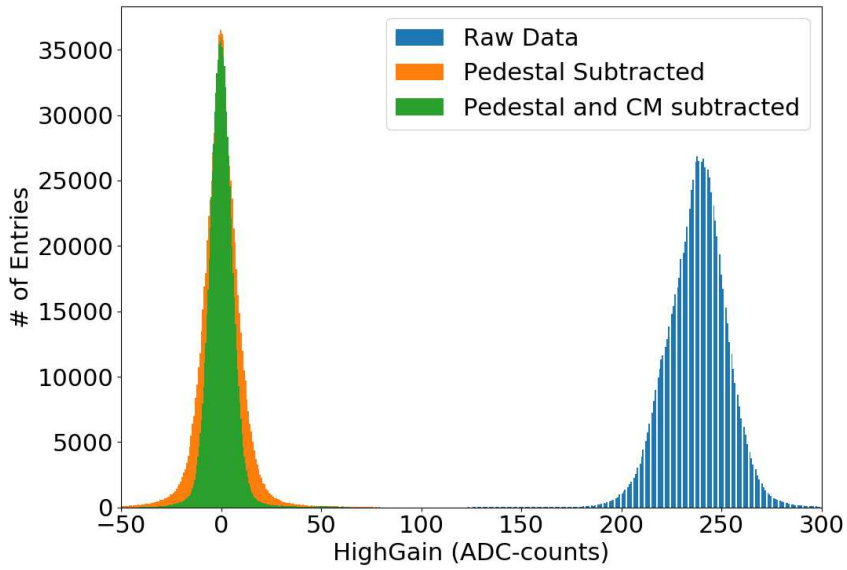
Figure 7.3.: Raw, pedestal subtracted and common mode subtracted SCA distributions for Module127. The discrete distribution for raw data comes from the integer output of the ADC, while other distributions are continues due to using mean for computing pedestals and common mode.
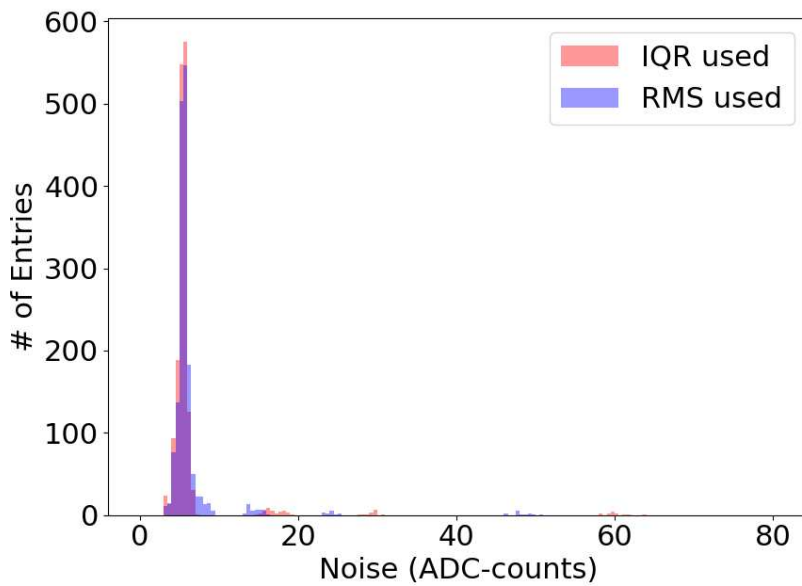
Figure 7.4.: Noise distribution for a pure pedestal run. Outliers occur in groups of 13 and belong to a noisy cell each. The very high noise cell at 60 ADC counts for the IQR measure is channel 22 in chip 3 which is below the HDMI connector.
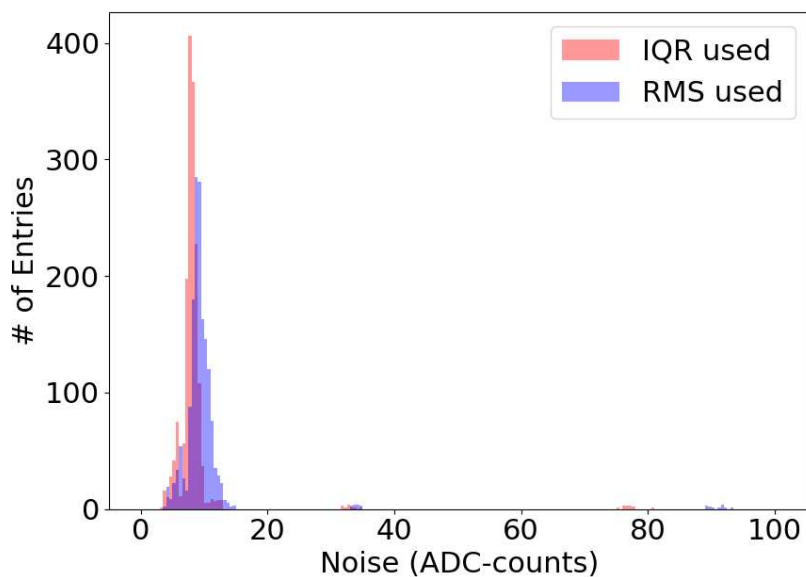
Figure 7.5.: Noise distribution for run with a lot of noisy events. The robust IQR gives more accurate results here because it is not biased by high noise events. It is important to quote noise with IQR measure here because these high noise events occur randomly and are not intrinsic to SCAs, thus they should not be considered.

Noisy cells are masked for test beam analysis and not used. Thus, also plots in chapter 8 exclude these cells. The distribution peaks at roughly $6\,ADC-counts$ (for the high gain), which gives a signal to noise ratio (SNR) of around 6, considering that a MIP signal equals roughly $35\,ADC-counts$, as known from calibration studies.

As addressed in the beginning of this section, Common Mode Noise can come from HV bias voltage which affects the whole sensor or from the LV supply for ROCs which affects only cells connected to one readout chip. For the latter case, common mode should be calculate per chip and not per hexaboard. A new plug-in is written to study this case which was needed to be completely rewritten, due to significant changes in the code. As seen in the example result in figure 7.6, this does not effect noise values significantly, thus the standard method using common mode calculation per hexaboard is used because it averages over roughly 100 cells and thus has a better statistical behaviour than calculation per hexaboard, which averages over roughly 25 cells only.

7.2.3. Studies on Non-Full Cells

Non-full cells, meaning half cells, mousebite cells, calibration pad and outer calibration ring, as described in section 4.5, are not considered so far in this chapter. It is expected that common mode noise is area dependent, thus it is not possible to use the same value
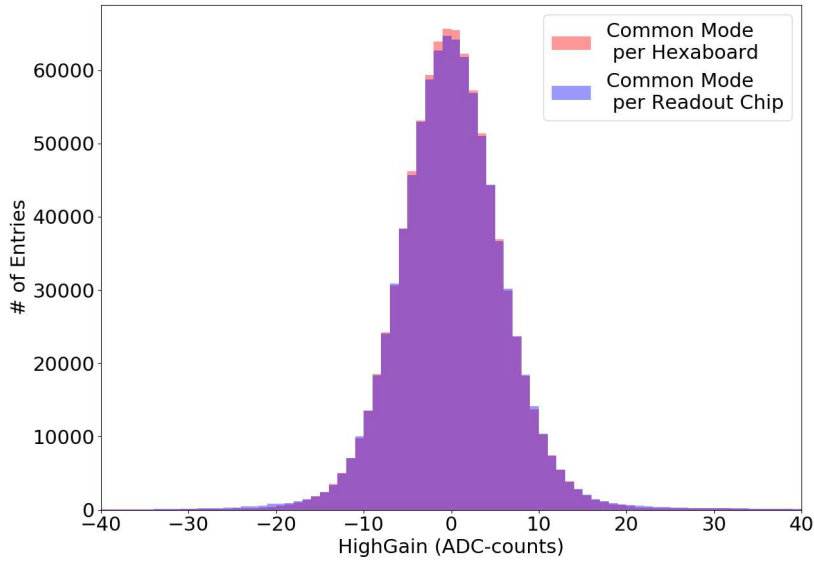
Figure 7.6.: SCA-values after pedestal and common mode subtraction for different types of calculating common mode. No significant difference is visible, thus common mode is chosen to be calculated per hexaboard due to higher statistics.

for common mode as for full cells. Moreover, computing common mode noise is not possible for most of them since there are only very few cells of the same type and an average would not make sense.

The following plots use a good pedestal run of Module127, thus common mode and pedestal value are calculated with mean method (using 1000 events) and noise is quoted as RMS of the residual distribution per SCA after subtracting pedestals and common mode.

Area Factor

As mentioned above, a big part of common mode comes from the HV supply of sensors, which effects all cells equally. A silicon pad sensor can be considered as one capacitor per cell, connected in parallel. A change in bias voltage $\frac{dU}{dt}$ leads to a current in such a capacitor according to equation 7.2. Capacitance in equation 7.2 is linear dependent on the area of a cell, according to equation 7.3 where the area is the only factor that changes for different cell types.

$$I = C\frac{dU}{dt} \tag{7.2}$$

$$C = \epsilon\frac{A}{d} \tag{7.3}$$

The used variables in equations 7.2 and 7.3 are:

$$I = \text{Cell current}$$
$$C = \text{Capactinace per cell}$$
$$\frac{\mathrm{d}U}{\mathrm{d}t} = \text{Change in voltage}$$
$$\epsilon = \text{Permittivity}$$
$$A = \text{Cell area}$$
$$d = \text{Height of the cell}$$

Noise of Non-Full Cells

The linear dependence of a current change from cell area)and thus also in common mode noise) can be accounted for by applying an area factor to the CMN of full cells. Thus, common mode of full cells is multiplied by the area of the non-full cell divided by the area of a full cell before subtracting common mode from non-full cells. Different behaviour of noise after common mode subtraction with and without an area can be seen in figure 7.7 and 7.8. The box plots use standard definition for IQR and define outliers of the distribution as all values outside 1.5 times IQR. This definition of outliers is taken from [19, p. 62]. Each SCA is treated separately in the plots.

The common mode for smaller cells without an area factor is over-correcting noise and subtracting too much which leads to a wider distribution and even higher noise than for full cells, in case calculated ADC values are below 0. To study this method, half cells are used. There are twelve half cells connected and an average over these cells is considered as the real value for common mode noise of half cells in plot 7.9.

Although the real value for noise is still lower than the noise value with area-corrected common mode noise, an improvement is clearly visible. There are other geometrical factors that might influence noise as well, such as edges and corners of cells. However, since the result in figures 7.8 and 7.9 show that using simple area factors leads already to a huge improvement af calculating noise for non-standard cells (considering the error bars), further and more complicated studies are not needed.

7.2.4. Conclusion and Final Noise Value

All these studies on noise of modules lead to the following conclusion for calculating noise in laboratory tests or cleanroom:

- Mean is used for calculating pedestals. The first seven time samples are used.

- Mean is used for common mode. Common mode is calculated per hexaboard.

- Noise is quoted as RMS of the residual distribution after pedestal and common mode subtraction per SCA.

66
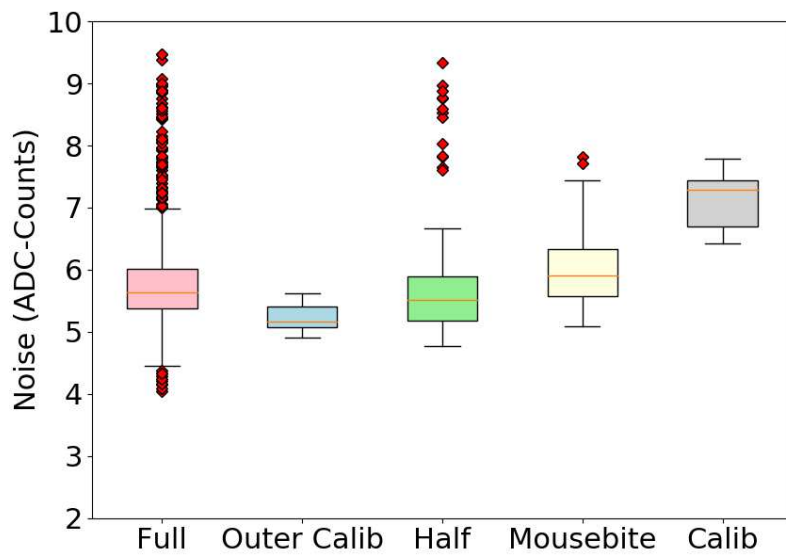
Figure 7.7.: Noise of different cell types with common mode calculated using full cells for all cell types. Cell types are sorted by their area. This estimation is overestimating noise for cells with a smaller area.
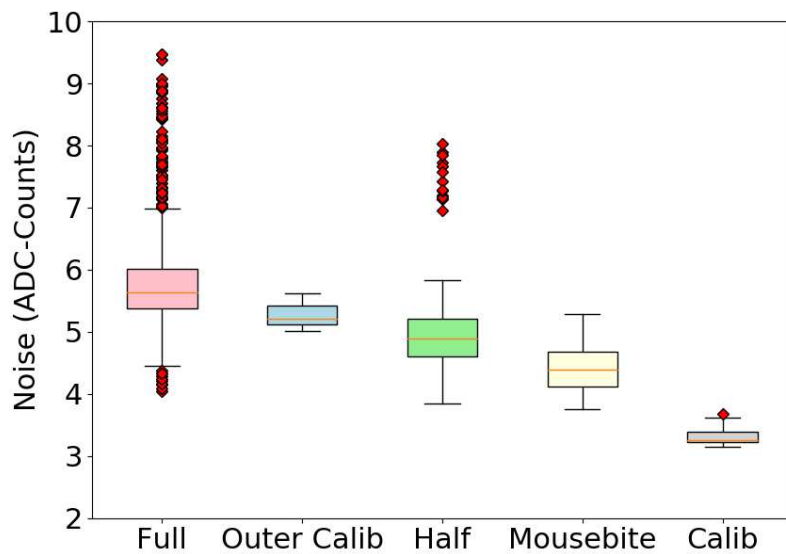
Figure 7.8.: Noise for different cell types using an area factor for non-full cells. Noise behaves as expected and decreases with decreasing cell area.

- 1000 events are used for each measurement.

These methods have proven to give the same results as the robust median and IQR and
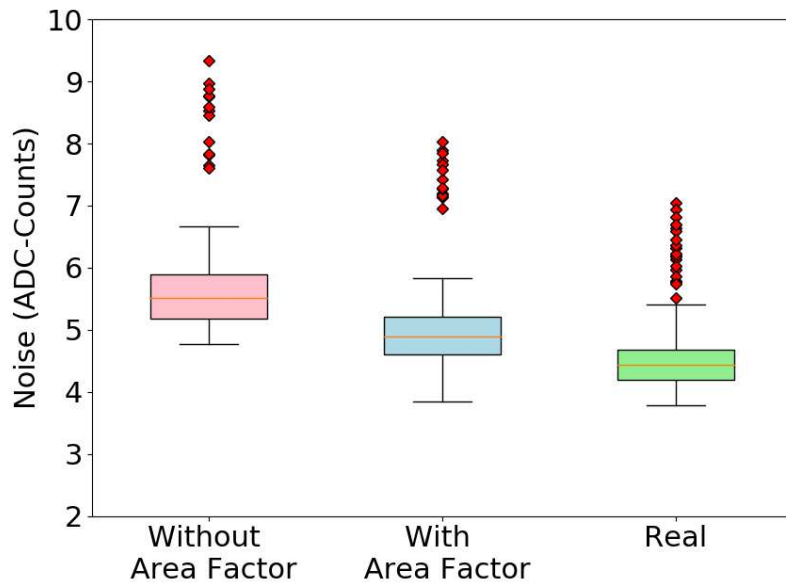
Figure 7.9.: Comparison of different techniques to calculate the common mode noise for non-standard cells. The area factor is a good improvement in the calculation which is already close to real noise.

are sensitive to outliers which is exceptionally needed for measurements in the clean-room because occasional irregularities give important information about performance of sensors.

8. Cleanroom Measurements for Noise Performance

A whole new experiment was set up in a cleanroom at CERN to measure sensors instead of full modules with the same readout system as used for testing modules. This challenging task combines sensor-related measurements, such as depletion voltage and capacitance with module-related noise performance measurements.

8.1. Commissioning of the Cleanroom-Setup

A new experimental setup needs proper commissioning in order to assure stable results. Thus, an intensive study on voltage stability and noise disturbance from the setup has been carried out before studies on actual noise behaviour of sensors took place.

8.1.1. Setup

Main idea behind the so-called *pogo pin setup* in the cleanroom is to use pogo pins on the backside of the hexaboard to contact sensor pads instead of wire bonds through holes in the PCB. Such a hexaboard can be seen in figure 8.1. This pogo pin card is placed on top of a sensor, which requires precise alignment of the sensor since pogo pins can only contact sensors at bonding pads. The sensor itself is put on a chuck which applies HV from the backside. A schematic of the whole setup can be seen in figure 8.2. Apart from the pogo pin card, the setup is quite similar as for lab tests, which is described in 5.6. The teststand with a Raspberry Pi is used for readout and connected to a PC in the cleanroom. This PC also controls HV power supply, which enables the option to change voltage automatically during tests. Chuck, sensor and teststand are put in a dark box which has common instruments of typical silicon probe stations mounted. Cameras of the probe station are crucial for aligning the sensor. Use of a probe station with a dark box requires some mechanical preparation such as a feedthrough and special cables to connect the power supply and PC. Big advantage is the stable environment in the cleanroom due to a humidity and temperature control unit in the room as well as nearly perfect light protection due to the dark box.

8.1.2. Commissioning

An intensive study of noise performance is carried out in order to investigate if pogo pins introduce additional noise compared to wire bonds. As a first step, noise of the pure pogo
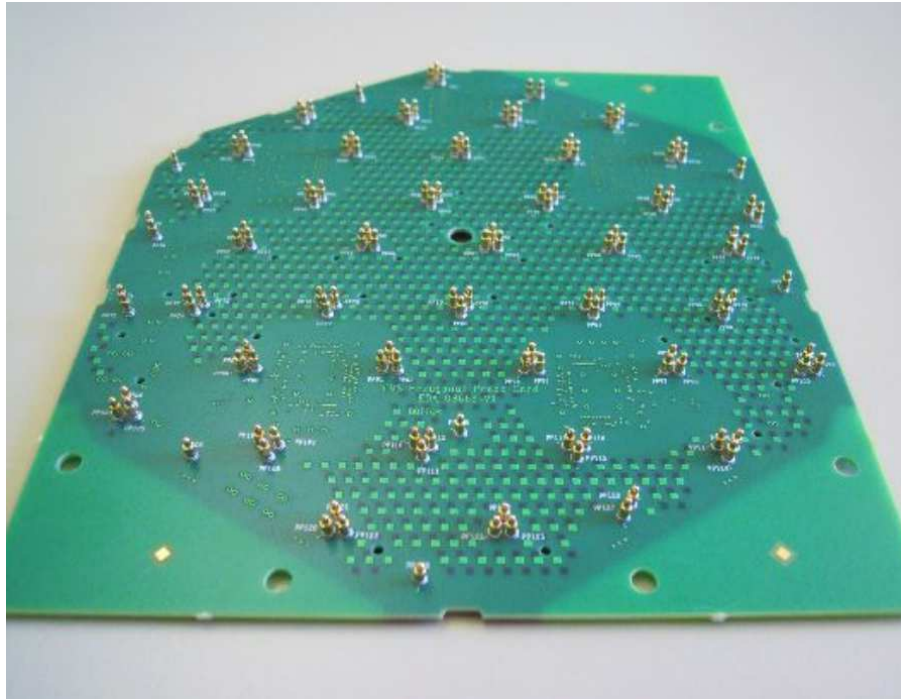
Figure 8.1.: Backside of hexaboard probe card with pogo pins. The additional PCB surrounding the hexagon is needed in order to mount the probe card in the dark box.
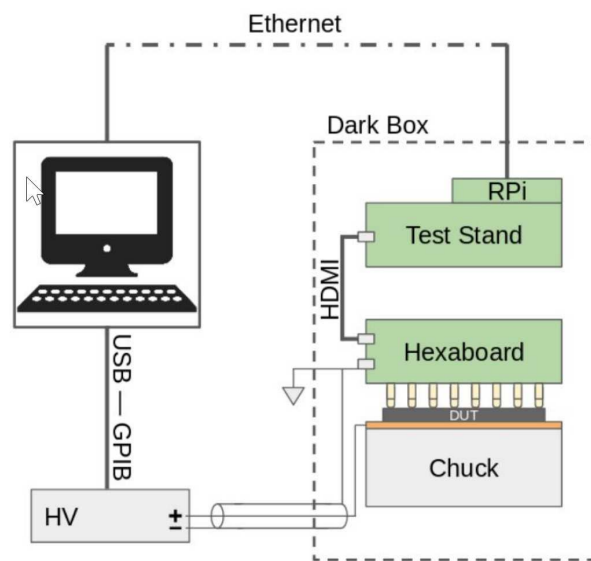
Figure 8.2.: Schematic of the pogo pin setup in the cleanroom. Apart from using the pogo pin card instead of a wire bonded hexaboard, the setup equals the laboratory setup during reception tests. Sensors are labelled as device under test (DUT). Not shown in this schematic is the interposer, which is crucial for a good noise performance.

pin card is measured and different ways of grounding are investigated. For these measurements, pogo pins are lifted from the sensor, thus no sensor, chuck and high voltage supply is actually needed. This is called the *floating pogo pin* setup. The pogo pin cards are rather precious since there are only two cards available, thus they should be handled carefully with the least mechanical stress from soldering or similar modifications possible. This is quite a challenge for grounding the card. The first idea is to use a special plug, which consists of the shielding connection from a micro-USB cable (but no wires inside) and plug it into the unused micro-USB plug of the hexaboard pogo pin card. Pedestal runs have been taken with same settings as for reception tests and the output is plotted in figure 8.3. Unfortunately, the noise peak with the special shielding-only plug is not
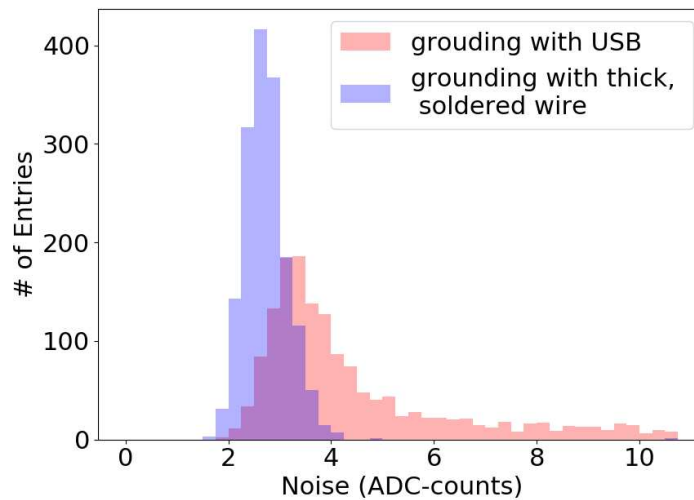
Figure 8.3.: Noise for different concepts of grounding. Pure intrinsic, electronic noise should have a Gaussian curve, which is not to case for USB grounding.

very sharp and also not Gaussian, which should be the case for pure electronic noise. Thus, a second attempt is taken and a thick wire is soldered to a soldering pad for the ground layer of the hexaboard pogo pin card. The result is given in figure 8.3 as well. The noise peak with this ground connection is clearly sharper and more Gaussian, which is the reason for continuing measurements with this setup.

Four sensors are tested in order to study noise performance of the whole setup. All of them are 300 µm thick, where three of them are p-type and one of them is n-type in order to compare it to an n-type module. Same pedestal runs as for the floating pogo pin setup are taken, but this time pogo pins are touching the sensors and high voltage is applied. The result for a bias voltage of 250 V can be seen in figure 8.4. This figure also includes a plot from Module76, where data is taken with same settings, in order to use it as a reference for comparison.

Two important results from figure 8.4 are stable noise distributions given by sharp, Gaussian-like peaks, as well as the fact that the noise-peak of the module is in the middle
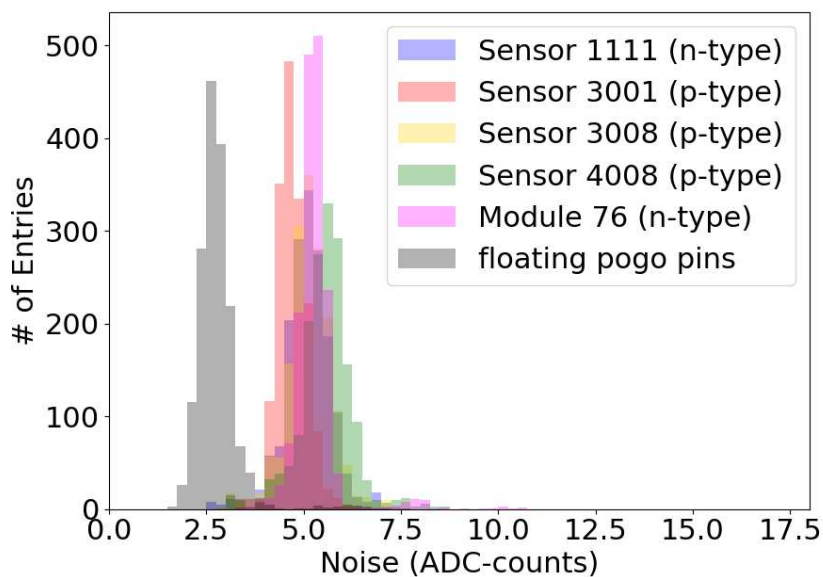
Figure 8.4.: Noise performance for different sensors at 250 V. The noise peak of floating pogo pins acts as lower limit for noise from sensors.

of the sensor-peaks. As a conclusion, pogo pins do *not* introduce more noise than wire bonds from modules. Noise of floating pogo pins should be much lower than noise coming from the pogo pin card with a connected sensor because there are less capacitances from sensors in the circuit. This is the case as seen in figure 8.4.

8.2. Noise Performance at Different Bias Voltages

A voltage scan for noise-values is another option (apart from CV and IV curves) to measure full depletion voltage. For keeping the result comparable and not considering edge and corner effects, only full cells have been used for this measurement. A voltage scan for the same sensors as used for commissioning can be seen in figure 8.5. For this kind of measurement, a noise-value for full sensors has to be defined. This value is chosen to be the mean of all noise values from SCAs connected to full cells and the error in figure 8.5 is given by the RMS of this noise distribution.
 Decreasing noise for higher voltages is expected because depletion-depth increases with higher voltages which leads to in increasing distance between capacitor plates in equation 7.3. Smaller capacitance leads to smaller noise, which explains the behaviour of the curves in figure 8.5. This also explains why noise does not get better after a certain voltage step (which is around 200 V for these sensors). This voltage equals the full depletion voltage, where depletion depth cannot grow any more, thus, noise becomes constant.
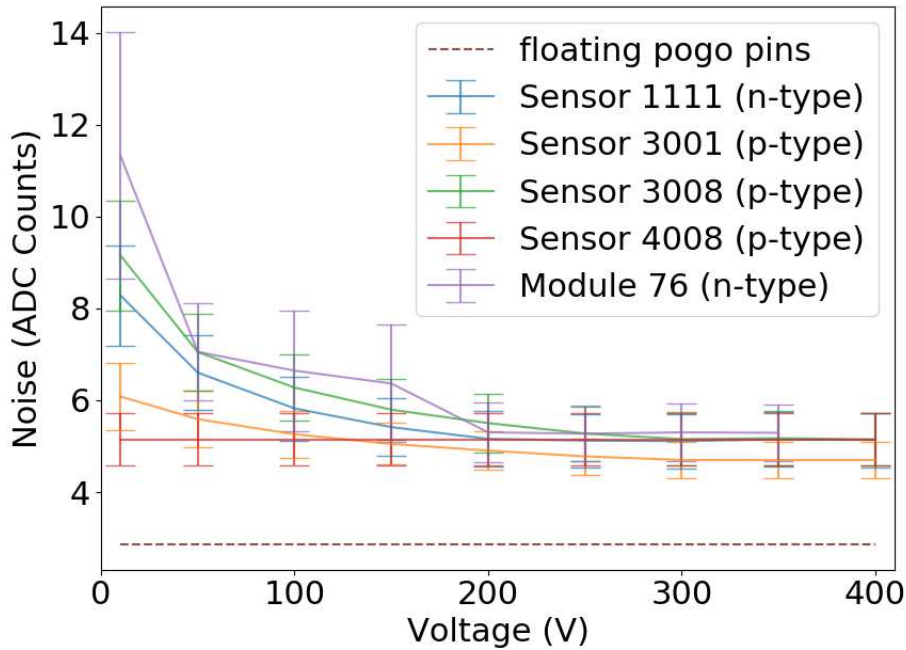
Figure 8.5.: Voltage scan in steps of 50 V for the same sensors as in figure 8.3. It is not possible to apply high voltage to floating pogo pins, thus a single measurement without biasing the floating pins is plotted as a dashed line.

8.3. Noise in Different Geometry Regions

Each sensor has four different regions with a different distance separating cells. This distance is called *inter-pad distance* and can be either 20 μm, 40 μm, 60 μm or 80 μm as mentioned in section 4.5. It influences the size of a pad resulting in a different pad area and, according to equation 7.3, different capacitance. The noise behaviour for these different geometries is studied here.

A previously taken pedestal run from Sensor1111 at 250 V bias voltage is chosen for this analysis. All SCAs belonging to full cells, which are not at the border of the sensor or to another inter pad distance region, are analysed for noise and the result is put into four different box plots representing the four regions. This box plots can be seen in figure 8.6. The settings for plotting are the same as described in section 7.2.3.

The decrease of noise with higher inter pad distance comes from the decrease in pad area for higher inter-pad distances. Although plot 8.6 shows this seems to be true for the 20 μm, 40 μm and 60 μm regions, noise from the 80 μm region is higher than the others, which is unexpected. Thus, further analysis is needed.

As a next step, the same analysis has been done for data from two modules taken during the reception tests. Unfortunately, the four inter pad regions overlap exactly with the four readout chips, thus there is no way to see if the result is really due to different
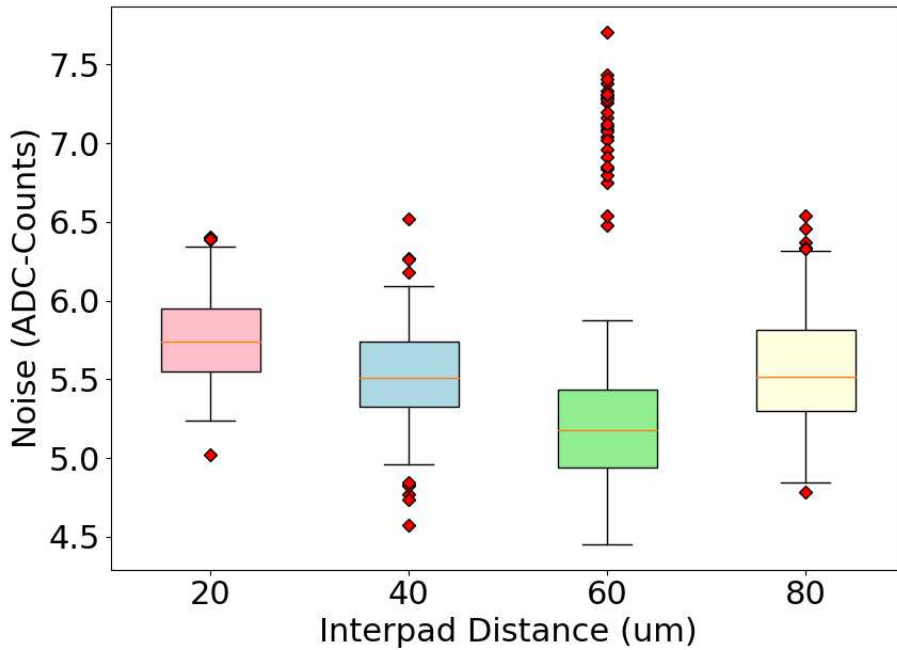
Figure 8.6.: SCA-noise separated for the four different inter pad distances. An overall decrease of the noise with increasing distance is expected, which is the case for the first three distances.

inter pad regions or due to slightly different behaviour of each readout chip. Since there is only one pogo pin card used for measurements, which has only four SKIROC2-CMS on it, modules with different chips are studied to investigate in this problem. The result plots can be seen in figures 8.7 and 8.8.

Unfortunately, the trends for noise of two example modules differ quite a lot from the sensor measurements, which leads to the conclusion that this effect comes most likely from readout chips than from sensor geometries.

This studies have shown that the noise difference between different inter pad distances is negligible. The final sensor design will have just one inter pad distance of 50 μm instead of four different geometric regions.

8.4. Noise Dependence from Capacitance

With the information from the two previous studies, it is possible to combine both results into one output two finally get a direct information of noise dependence on capacitance.
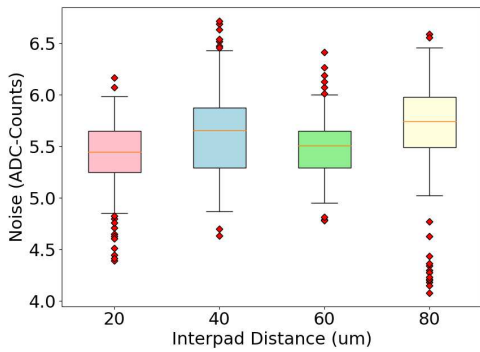
Figure 8.7.: Noise for different inter pad regions in Module127. The trend differs from figure 8.6 and figure 8.8.
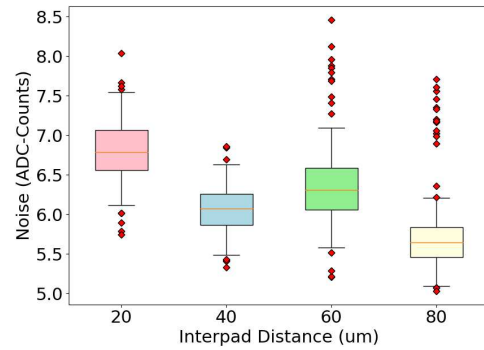
Figure 8.8.: Noise for different inter pad regions in Module133. The trend differs from figure 8.6 and figure 8.7. This is a hint that the noise trend comes mainly from different read-out chips.

8.4.1. CV-Measurement

The Capacitance-Voltage (CV) curve is needed in order to convert a bias voltage of a pad to its capacitance. This measurement is described in section 4.5.2, where a full output for a certain voltage step can be seen. Intensive studies have been done for CV measurements as well beforehand and for this analysis, the result from the latest CV measurement are needed as input. As a reference, figure 8.9 shows a typical CV curve for a single cell. As mentioned before, decreasing capacitance for increasing voltage due to bigger depth of the depletion zone can be seen. Capacitance has its minimum at full depletion voltage and stays constant afterwards.

8.4.2. Noise at Different Capacitances

Analysis of noise for different capacitances is similar to the comparison of noise for different voltages described in section 8.2. However, this time voltage is converted to a capacitance using CV-curves. Moreover, noise is not summed up over the sensor any more and the curve for each cell is printed separately. In order to keep it comparable, again just full cells which are not on the border of the sensor or to a different inter pad region are plotted. Figure 8.10 shows the result. It might not look very tricky to do this analysis, however, this plot needs input from four different sources, three measurements and two different setups, thus it is quite complicated to match information from different inputs since they do not use the same mapping and output style.

The results from figure 8.10 and figure 8.6 confirm each other with respect to decreasing noise for increasing inter pad distance with the exception of the 80 μm region. Also, according to figure 8.5 (low voltage equals higher noise) and the CV curve (low voltage
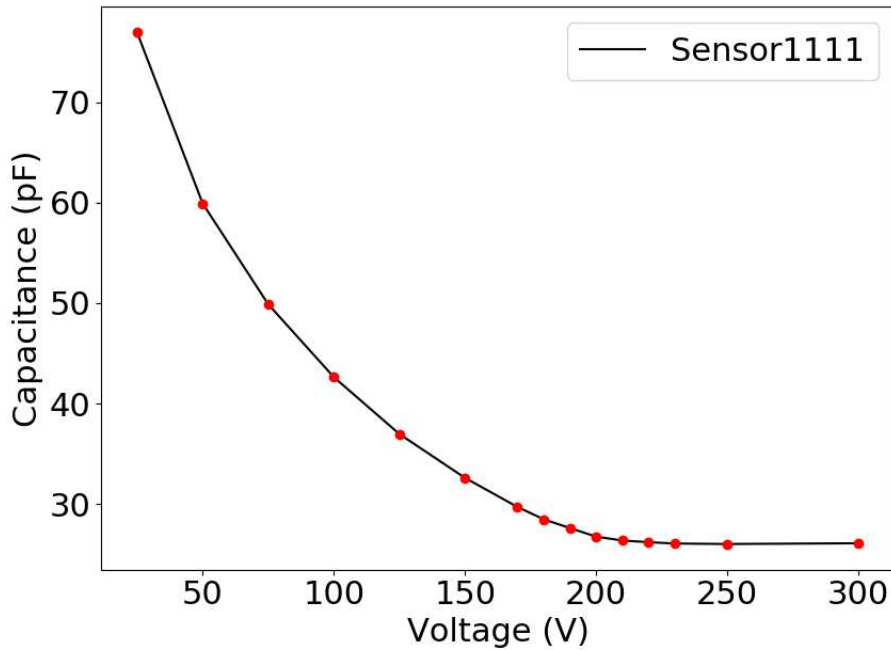
Figure 8.9.: CV-measurement for pad 19 on Sensor1111. Depletion voltage is reached around 200 V.

equals high capacitance), the behaviour of increasing noise with increasing capacitance is explained. Noise does not change for voltages over full depletion voltage. In order to see this behaviour as well, voltage was ramped up to 300 V, which gives, with a step size of 50 V, three measurement points at or over full depletion voltage (200 V). These points are the small kinks in figure 8.10 for low capacitances.

However, there is another important output from this analysis. For noise coming from silicon sensors, a linear increase with capacitance is expected, according to [20, p. 123]. The single cell curves in figure 8.10 show a very linear form which leads to the conclusion that measured noise is really coming directly from the sensor and not from readout electronics or other sources.
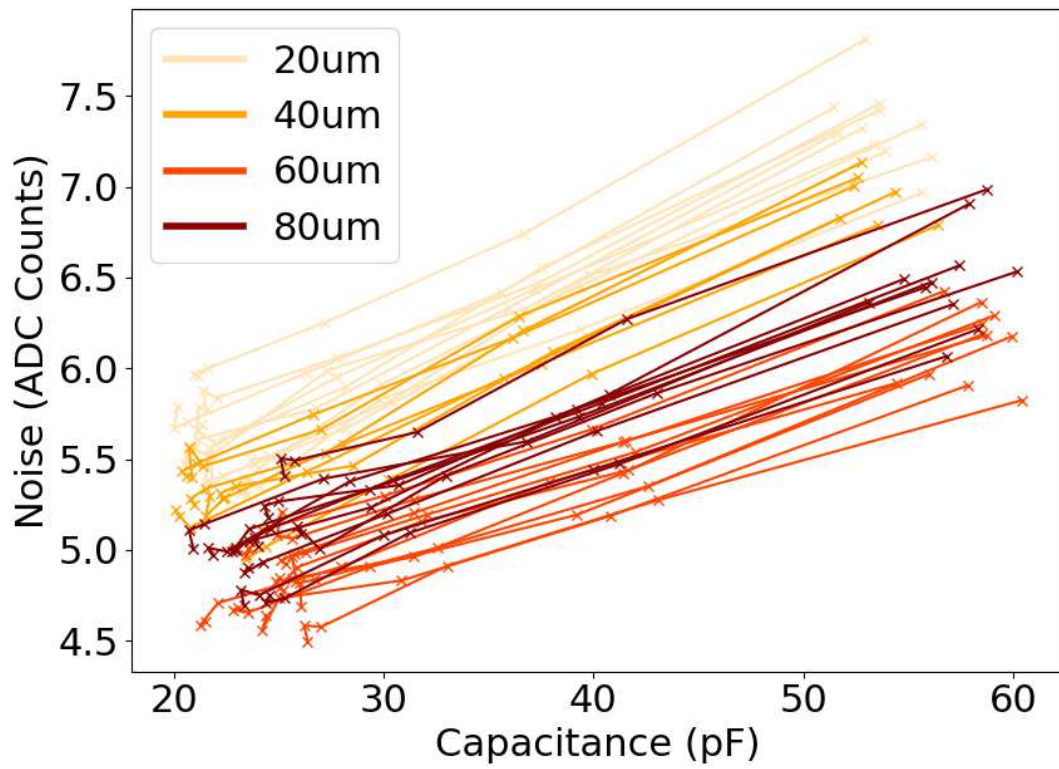
Figure 8.10.: SCA noise for cells at different capacitances in Sensor1111. The four different colours belong to the four different inter pad regions. The same cells as in plot 8.6 are used for comparison

9. Conclusion

The scope of this diploma thesis was quite wide spread and divided into two main parts which seemed to be quite independent from each other at first, but have shown a lot of similarities in analysis and setup afterwards. A detailed understanding of the analysis procedure for test beam combined with detailed knowledge of silicon sensors is needed in order to retrieve relevant information for noise out of sensor measurements.

The SKIROC2-CMS has proven to be a perfect choice for prototype modules of the HGCal detector showing promising results with respect to SNR, which has been studied during this project. The use of three different gains for different signal sizes is working perfectly and analysis gives stable results for all three regions. Furthermore, timing performance due to a ToA measurement implemented in the SKIROC2-CMS shows a behaviour which reaches requirements, as shown in preliminary results from other analysis groups.

For all these results and further studies on resolution and performance, the test beam delivered indispensable data for analysis. The test beam carried out during this thesis was challenging due to a high amount of modules which have never been studied altogether at once before. In fact, it was even tricky to fit the whole detector into the beam line because the HGCal prototype uses a lot of space. With construction, commissioning and operation of a prototype at this size, a lot of knowledge was gained, which gives a good basis for further test beams and final operation as part of CMS. Not to mention the fact that this test beam was a very good training for people to get familiar with operation of the detector itself and also on how to carry out needed shifts during test beams.

The most challenging part in this thesis was the analysis framework of test beam data. It uses highly advanced CMSSW software already at this prototype stage, which will be needed during operation at CMS. Understanding basic principles from this framework was crucial in order to perform noise studies, where one has to dig really deep into the framework. The developed plug-in for dedicated noise studies was needed not only to study non-full cells; it is also a baseline for noise studies on sensors. This study delivered valuable information on how to deal with non-full cells, which need special treatment due to a lack of statistics. Over 50 people still take part in analysis of test beam data carried out already in October 2018 to understand as much details as possible from this prototype. This shows once again the importance of this test beam.

Testing pure silicon sensor faces oneself with completely new challenges. Some training with the cleanroom setup was needed in order to carry out CV measurements which are another input needed for the desired studies on noise performance in the end. Setting up a whole new measurement in the cleanroom was a bigger challenge than expected. The setup is very similar to reception tests, however, commissioning of this setup in the

cleanroom was not as easy as expected. Acquiring data for sensor testing comes with additional requirements for the DAQ system as well since different voltage steps, which are changing during data acquisition, are needed. Thus, also the teststand framework needed some refurbishment to operate in the cleanroom. Another challenge here was the not aligned numbering of pads an readout channels and different output formats of the two systems, which were difficult to combine. Nevertheless, we managed to deal with this challenges and got very nice results on noise performance of sensors in the end. Especially the results on noise for different geometrical regions and linearity of noise with respect to capacitance are two really promising outputs that have never been measured before this project.

This setup for noise measurements acts as a baseline to carry out more advanced studies on charge collection measurements with light injection and a laser. Additional components for these measurements are being commissioned at the moment and this project provides a lot of knowledge on hardware, DAQ firmware and analysis software needed.

Acknowledgements

Bibliography

[1] HiLumi - CERN, ed. *The HL-LHC project*. May 2018. URL: `http://hilumilhc.web.cern.ch/about/hl-lhc-project` (visited on 07/07/2019).

[2] CMS Collaboration, ed. *How CMS Works*. 2019. URL: `http://cms.cern/detector` (visited on 08/07/2019).

[3] FLUKA Team 2000–2019, ed. *FLUKA*. May 21, 2010. URL: `http://www.fluka.org/fluka.php` (visited on 08/07/2019).

[4] CMS Collaboration. *The Phase-2 Upgrade of the CMS Endcap Calorimeter*. Tech. rep. CERN-LHCC-2017-023. CMS-TDR-019. Technical Design Report of the endcap calorimeter for the Phase-2 upgrade of the CMS experiment, in view of the HL-LHC run. Geneva: CERN, Nov. 2017. URL: `https://cds.cern.ch/record/2293646`.

[5] CMS Collection, ed. *Collision events recorded by CMS in 2016*. Jan. 10, 2017. URL: `https://cds.cern.ch/record/2241144` (visited on 08/07/2019).

[6] Frank Hartmann. *Evolution of Silicon Sensor Technology in Particle Physics*. 2017. ISBN: 978-3-319-64434-9.

[7] Hermann Kolanoski and Norbert Wermes. *Teilchendetektoren*. Springer, 2016. ISBN: 9783662453490, 9783662453506. DOI: `10.1007/978-3-662-45350-6`.

[8] Grupen Claus and Boris Shwartz. *Particle Detectors*. 2008. ISBN: 978-0-511-38866-8.

[9] Daniel Pitzl. *Detectors for Particle Physics. Lecture 2: Showers and calorimeters Particle flow*. DESY. 2011. URL: `http://www.desy.de/f/students/lectures2011/lec3.pdf` (visited on 06/10/2019).

[10] *Detectors for Particle Physics. Calorimeters*. presentation. May 23, 2019.

[11] STFC. *CMS ECAL Endcaps photographs*. CERN. 2008. URL: `https://hepwww.pp.rl.ac.uk/groups/CMSvpt/bestphotos/Crystal%20Palace/slides/F2_026_23.htm` (visited on 08/26/2019).

[12] M.A. Thomson. 'Particle flow calorimetry and the PandoraPFA algorithm'. In: *Nuclear Instruments and Methods in Physics Research Section A: Accelerators, Spectrometers, Detectors and Associated Equipment* 611.1 (2009), pp. 25–40. ISSN: 0168-9002. DOI: `https://doi.org/10.1016/j.nima.2009.09.009`. URL: `http://www.sciencedirect.com/science/article/pii/S0168900209017264`.

[13] Elias Pree. 'Development of Large Area Silicon Sensors for the High Granularity Calorimeter at CMS'. dissertation. Institut für Hochenergiephysik, Sept. 9, 2018.

[14] D Contardo et al. *Technical Proposal for the Phase-II Upgrade of the CMS Detector*. Tech. rep. CERN-LHCC-2015-010. LHCC-P-008. CMS-TDR-15-02. Upgrade Project Leader Deputies: Lucia Silvestris (INFN-Bari), Jeremy Mans (University of Minnesota) Additional contacts: Lucia.Silvestris@cern.ch, Jeremy.Mans@cern.ch. Geneva, June 2015. URL: https://cds.cern.ch/record/2020886.

[15] Florian Pitters et al. 'ARRAY: An Open Source, Modular and Probe-Card based System with Integrated Switching Matrix for Characterisation of Large Area Silicon Pad Sensors'. In: *arXiv:1903.10262 [physics.ins-det]* (May 25, 2019).

[16] Arnaud Steen and Bora Akgun. 'DAQ System for the HGCAL Beam Tests (to be submitted to JINST)'. Aug. 2019.

[17] DESY. *EUDAQ*. 2011. URL: https://github.com/eudaq (visited on 07/04/2019).

[18] Artur Lobanov. *OCTOBER TEST BEAM: SUMMARY*. Oct. 24, 2018. URL: https://indico.cern.ch/event/767686/contributions/3188736/attachments/1740542/2816371/HGC_TBOct2018_Summary.pdf.

[19] A. Unwin, M. Theus, and H. Hofmann. *Graphics of Large Datasets: Visualizing a Million*. Statistics and Computing. Springer New York, 2007. ISBN: 9780387379777. URL: https://books.google.at/books?id=VY8BGEcpwdYC.

[20] Helmut Spieler. *Semiconductor Detector Systems*. 2005. ISBN: 0–19–852784–5.

Glossary

AC Alternating Current.

ADC Analogue to Digital Converter.

AHCAL Analogue HCAL.

ALICE A Large Ion Collider Experiment.

ASIC Application Specific Integrated Circuit.

ATLAS A Toroidal LHC ApparatuS.

CE-**E** Calorimeter Endcap - Electromagnetic.

CE-**H** Calorimeter Endcap - Hadronic.

CERN Organisation européenne pour la recherche nucléaire.

CMN Common Mode Noise.

CMS Compact Muon Solenoid.

CMSSW CMS-SoftWare.

CV Capacitance-Voltage.

DAC Digital to Analogue Converter.

DAQ Data AcQuisition.

DCS Detector Control System.

DESY Deutsches Elektronen Synchotron.

DQM Data Quality Monitor.

DUT Device Under Test.

ECAL Electromagnetic Calorimeter.

EYETS Extended YETS.

FPGA Field Programmable Gate Array.

GPIO General Purpose Input Output.

HCAL Hadronic Calorimeter.

HG High Gain.

HGCal High Granularity CALorimeter.

HL-LHC High Luminosity LHC.

HLT High Levlel Trigger.

HPK Hamamatsu Photonics.

ID Identification.

IQR Inter Quantile Range.

JTAG Joint Test Action Group.

LG Low Gain.

LHC Large Hadron Collider.

LHCb LHC-beauty.

LS Long Shutdown.

MC Monte Carlo.

MCP Multi Channel Plate.

MWPC Multi Wire Proportional Chamber.

PCB Printed Circuit Board.

RM Roll Mask.

RMS Root Mean Square.

ROC ReadOut Chip.

SCA Switch Capacitor Array.

SCR Space Charge Region.

SMU Source Measurement Unit.

SPS Super Proton Synchrotron.

TAC Time to Analogue Converter.

ToA Time of Arrival.

ToT Time over Threshold.

TS Time Sample.

WIMP Weakly Interacting Massive Particle.

YAML Yet Another Markup Language.

YETS Year End Technical Stop.

Appendices
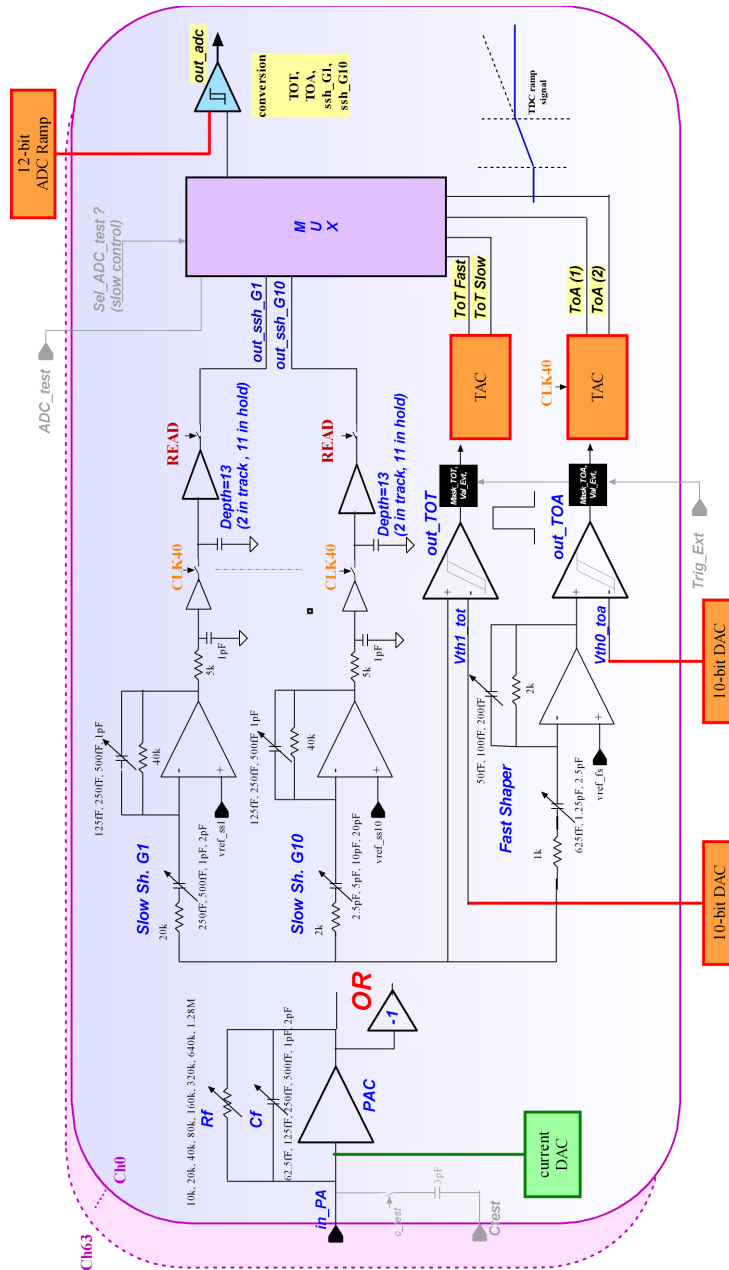
A. SKIROC2-CMS Schematics

Figure A.1.: Schematic of the SKIROC2-CMS . The four measurements circuits from top to bottom consists of the LG, HG, ToT (all three are used for energy measurement) and ToA (used for timing).

B. SKIROC2-CMS Memory Mapping

- Readout is MSB first and high address first
- Global TS is gray encoded
- Extra bit is LSB counter on falling edge (binary decoded)

- ADC data are 12 bits gray
- Conv order : TOT / TOA / Q
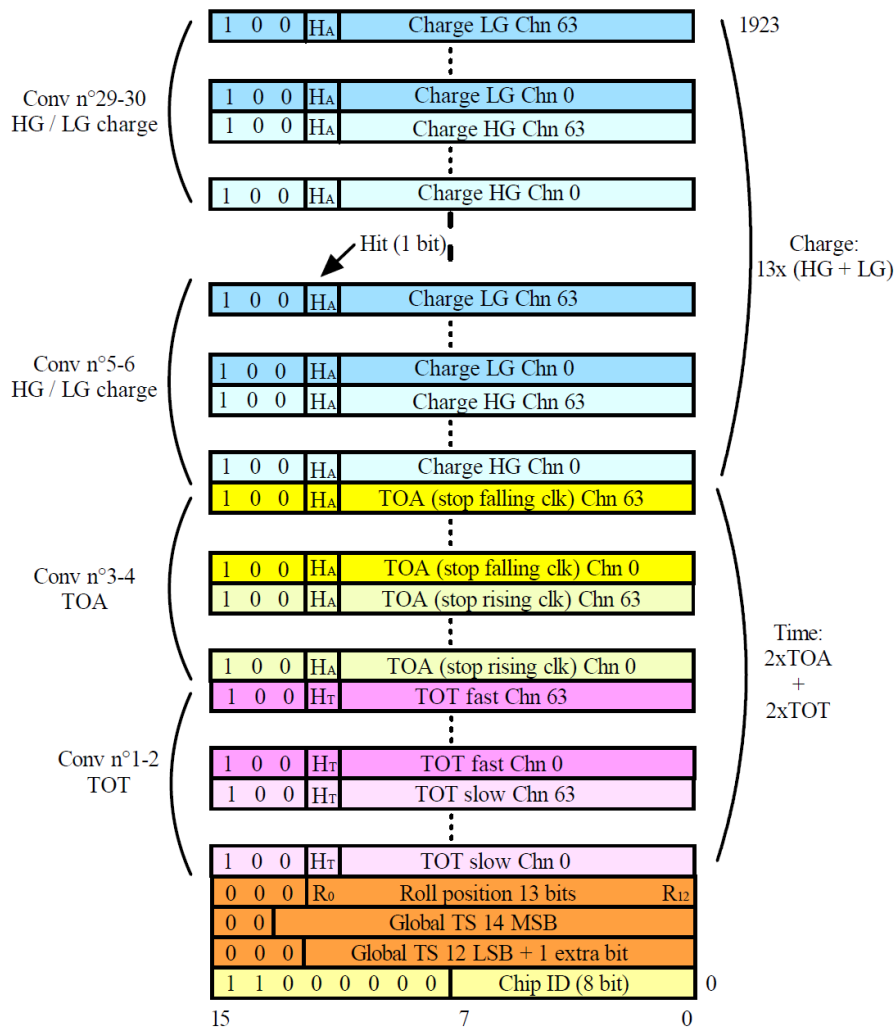- First conv is "TOT fast" with FlagTdc @ '1'

Figure B.1.: Memory Map of the SKIROC2-CMS .

C. Configurations during Test Beam

Configuration 1:

- ◉ EE: 28 layers x 1 module
- ◉ FH: 9 x 7 + 3 x 1
- ▲ FH absorbers between all layers

Configuration 2:

- ◉ EE: 28 layers x 1 module
- ◉ FH: 2 x 1 + 9 x 7
- ▲ No FH absorbers between 2 x 1 layers

Configuration 3:

- ◉ EE: 8 layers x 1 module
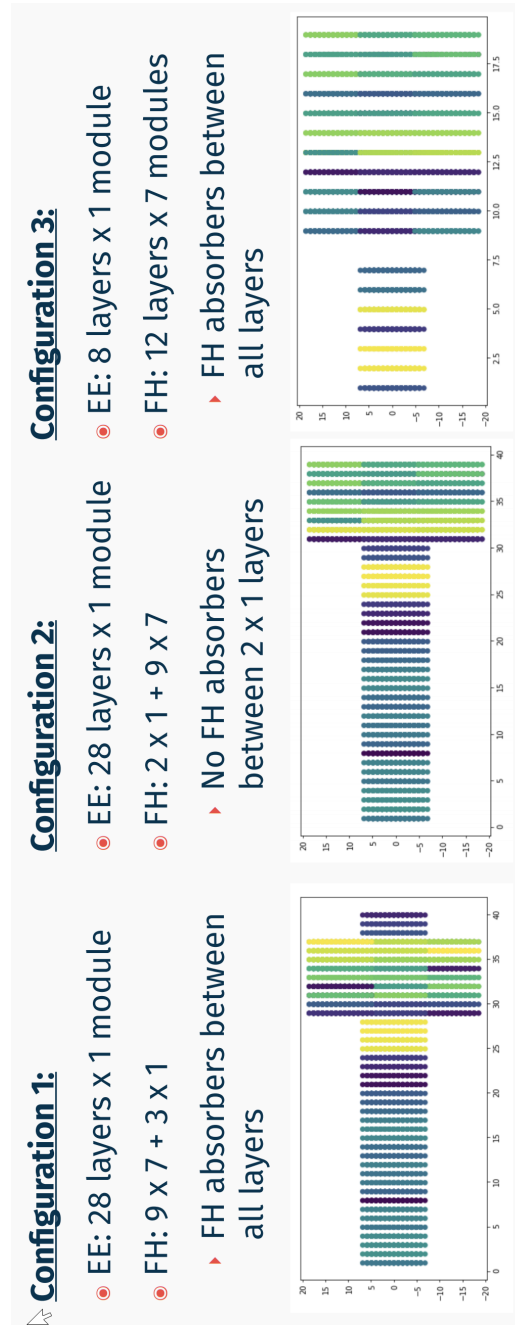- ◉ FH: 12 layers x 7 modules
- ▲ FH absorbers between all layers

Figure C.1.: Different Configuration during the test beam.

95